Hues of Habitability: Characterizing Pale Blue Dots Around Other Stars

Citation

Rugheimer, Sarah M. 2015. Hues of Habitability: Characterizing Pale Blue Dots Around Other Stars. Doctoral dissertation, Harvard University, Graduate School of Arts & Sciences.

Hues of Habitability: Characterizing Pale Blue Dots Around Other Stars

A dissertation presented

by

Sarah MacGregor Rugheimer

to

The Department of Astronomy

in partial fulfillment of the requirements

for the degree of

Doctor of Philosophy

in the subject of

Astronomy & Astrophysics

Harvard University

Cambridge, Massachusetts

January 2015

Dissertation Advisor: L. Kaltenegger and D. Sasselov Sarah MacGregor Rugheimer

Hues of Habitability: Characterizing Pale Blue Dots Around Other Stars

Abstract

A wide range of potentially rocky transiting planets in the habitable zone (HZ) have been detected by Kepler as well as ground-based searches. The spectral type of the host star will influence our ability to detect atmospheric features with future space and ground based missions like JWST, GMT and E-ELT. For my thesis, I present a complete suit of stellar models with a stellar effective temperature ranging from $T_{\text{eff}} = 2300$K to $T_{\text{eff}} = 7000$K, sampling the entire FGKM stellar type range, for modeling extrasolar planets. I also have a grid of model atmospheres for an Earth-analogue planet orbiting stars and derive remotely detectable spectral atmospheric features.

The UV emission from a planet's host star dominates the photochemistry and thus the resultant observable spectral features. Using the latest UV spectra obtained by Hubble as well as IUE, I model Earth-like planets for a wide range of host stars. I detail the results of activity on the primary detectable atmospheric features that indicate habitability on Earth, namely: H_2O, O_3, CH_4, N_2O and CH_3Cl. I model the emergent spectra of Earth-analogue planets orbiting our grid of FGKM stars in the VIS/NIR (0.4 μm - 4 μm) and the IR (5 μm - 20 μm) range in accordance with future mission design concepts like JWST and direct detection missions like HDST/LUVOIR in the more distant horizon. We also model the amount of UV flux reaching the surface of Earth-like planets at various geological epochs ranging from a pre-biotic world through the rise of oxygen and for Earth-like planets orbiting FGKM stars at equivalent stages of evolution.

Contents

Acknowledgments

I would like to thank my advisors, Lisa Kaltenegger and Dimitar Sasselov, for sharing their passion of astronomy and astrobiology and for guiding and encouraging me through the process of becoming a scientist. It is hard to imagine two more enthusiastic advisors. I particularly thank Lisa for her assurances that I am not an "impostor" and Dimitar for his encouragement of work-life balance. I would like to thank my thesis committee: Dave Charbonneau, Rosanne Di Stefano, Mercedes López-Morales, and Jeff Linsky. In particular, I would like to thank Dave Charbonneau for his excellent career guidance and for his comment "there are no geniuses."

To the many graduate students who have been supportive and encouraging on this path: Sarah Ballard, Zach Berta-Thompson, Nick Stone, Wen-Fai Fong, Maggie McLean a.k.a. Sr. Hope, Chris Faesi, Bob Penna, Paul Torrey, Greg Snyder, Laura Blecha, Gurtina Besla, Elisabeth Newton, Josh Suresh, Robert Harris, Diego Munoz, Lauranne Lanz, Sukrit Ranjan, Tanmoy Laskar, Katherine Rosenfeld, Ragnhild Lunnan, Eliza Kempton, Jason Dittmann, John Lewis, Maria Drout, Ryan O'Leary, Jack Steiner, Dylan Nelson, Maxwell Moe, Nathan Sanders, Blake Cullen, Joey Munoz, Meredith Hughes, Stephanie Bush, Robert Marcus, Chris Hayward, Andy Friedman, Ben Maruca, Bekki Dawson, Laura Schaefer, Courtney Dressing, and Li Zeng.

To my many friends, who have been supportive in the best and worst of times: Sarah Douglas, David Roberson, Ty Robinson, Joel and Brianna Quick, Andy Cohn, Deb Kaplan, Deb Wegener, Cassie Freyschlag-Siler, Shawn Domagal-Goldman, Tom Norman, Liz Brown, Himmi Kariyawasam, Brittany Schmidt, Caitlin Casey, Andras Zsom, Vlada Stamenkovic, Sean Corcoran, Dan Therrien, Corby Harwood, Jessie Berta-Thompson, Ethan Butler, Kaye Wierzbicki, Sid Hegde, Yami Miguel, Annie Mejia, Alicia Breakey, Cliff Johnson, Ceclia and Ben Ehrenfield, Daniel Green, Lori Schneider, Clarissa Scholes, Julie LeDoux, Ben Mohlie, Amanda Nguyen, Phil Ashby, Easwar Magasan, Simon Poole, Fern Marusiak, Krystal Brown, Nick Allen, Nichelle Tirtzah Lewis, Colleen Hayes, Andrew Jurdan, Mikhail Kats, Mike Einziger, and Jeffrey Lim.

My Fellow Harvard Horizons Cohort: David Roberson, Tom Norman, A.J. Kumar, Adam Anderson, Heather Olins, Danny Orbach, and Whitney Henry.

To the wonderful administrators who make everything happen: Peg Herlihy, Robb Scholten, Amanda Preston, Jamie Villanueva, Sara Yorke, Brenda Atchison, Kelly Moreno, and Jean Collins.

To Dr. Rue Wilson, for guiding me in stress management and self-discovery.

To influential teachers: Prof. Richard Schaus, Prof. Rachid Ouyed, Prof. Ramesh Narayan, Prof. Newton Kupelian a.k.a. "Dr. Kupes," Mrs. Sue Brown, and Ms. 'Asta Bowen.

I would never be here today without the guidance of influential life mentors. Sally Conrad (ever so slightly off-center and mildly irreverent), I thank you for showing me how to live a full and good life. Debbie Burke, I thank you for guiding me in my growth as a writer and being ever non-offendable.

I thank my family, brothers and sisters for being shining examples of excellence before me. In particular, my brother Dr. Paul Rugheimer, who gave me my first fantasy novel and for his love of physics thought experiments.

I thank my wonderful spouse, Christian Schmid MacGregor, for your love and

support, for allowing me to stay up late finishing work, and for encouraging me at every turn. For taking care of my father in dementia, though you never knew him before. For leaving your friends, family, and job to join me in Cambridge. For truly being with me in sickness and in health, in good times and bad times, in joy as well as sorrow.

Most of all I would like to thank my father, Norman “Mac” Rugheimer, for being the best father I could imagine. For supporting me in any passion I pursued. For driving me 5.5 hours each way to Irish dance lessons for 8 years. For looking over my first year physics homework. For telling me I have to major in what I want to major in, not what he would want me to major in. For always supporting every decision, even if he disagreed, to the best of his ability. For showing me a passion for teaching. For making such a positive impact in every life you touched that people still glow when talking about your influence decades later. For facing the end with absolutely no fear. For fully embodying the quote: “You only live once, but if you do it right, once is enough.” It was an honor and a pleasure being your daughter. You will forever be in my heart and I dedicate this thesis to your memory.

In loving memory of my father, for sharing the beauty of the Universe with me.

Dr. Norman "Mac" Rugheimer

Physics Professor MSU

February 10th, 1930 - February 4th, 2010

Chapter 1

Introduction

1.1 Finding Earth 2.0

This planet we call home is teeming with life from the very depths of the ocean where no light penetrates, to small brine layers between ice crystals and near boiling iridescent waters of Yellowstone. As we discover the vast diversity of extremophile life on Earth, our minds can only begin to imagine the possibilities for life to exist on other planets in the Universe. Yet, despite the vast array of planets in our solar system, we only have one example of an inhabited planet so far: *Earth*.

One of the first steps toward answering the big question, "Are we alone in the Universe?" is to first find suitable environments for life to thrive outside of Earth. Indeed, while Mars and several icy moons in our Solar System may be able to host life now or in the past, Earth has been particularly successful at providing environments allowing life to flourish. Though we only have a sample size of one, this singular example drives the search for another habitable planet.

We have made great strides toward detecting habitable, rocky worlds. When I started graduate school, no sub-neptune sized planets were known. Yet now we know of dozens of rocky exoplanets candidates in the habitable zone (HZ). Occurrence rates suggest that we will find a habitable transiting planet within 20 pc of Earth (Dressing & Charbonneau 2015). In the next few decades, we hope to observe atmospheric features of small, Earth-like planets. The technological challenges are huge. All information of these new worlds in the foreseeable future, whether blended together with starlight or resolved separately from the host star, will lie within a single pixel. In 1990, Voyager I turned back toward Earth to take a picture from six billion kilometers away, the farthest human technology had been from our planet. All of Earth is captured in that one pale blue dot (see Fig. 1.1, right).

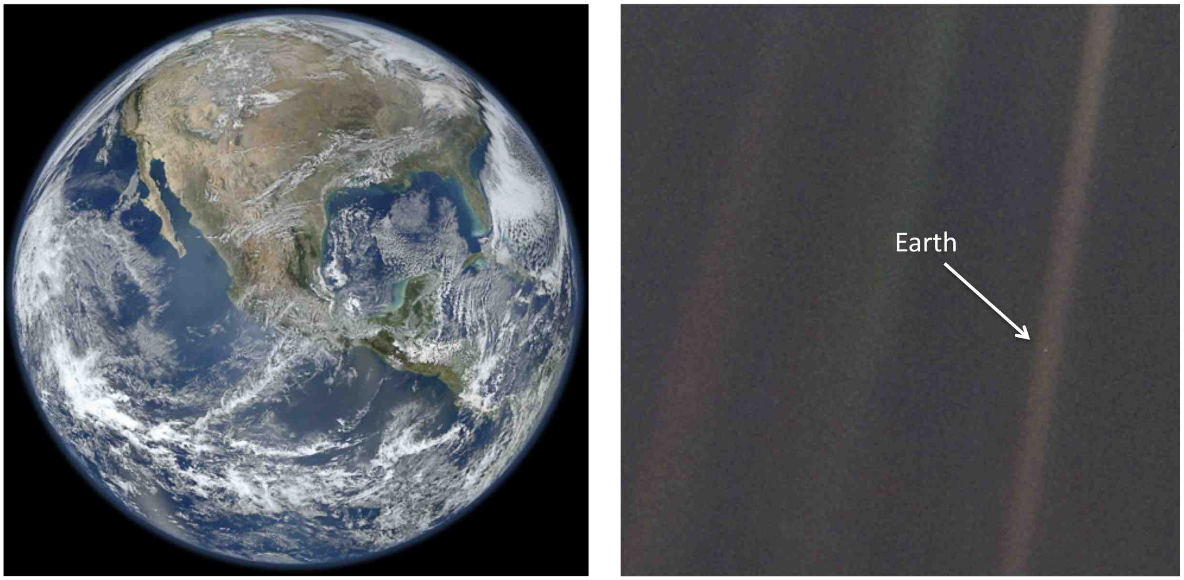

Figure 1.1: NASA photograph of Earth taken Jan 2012 (left) and of Earth taken by Voyager I taken 6 billion km away (right). Image Credits NASA.

The history of exoplanet detections started back when I was in grade school, without a thought in my mind of some day being an exoplanetary astronomer. The first extrasolar planet around a Sun-like star was found in 1995 (Mayor & Queloz 1995). But even without direct evidence, extrasolar planets have been thought to exist for millennia. As early as fourth century BCE, Democritus postulated the existence of not only other planets, but of life like our own existing on them:

> There are innumerable worlds of different sizes. In some there is neither sun nor moon, in others they are larger than in ours and others have more than one. These worlds are at irregular distances, more in one direction and less in another, and some are flourishing, others declining. Here they come into being, there they die, and they are destroyed by collision with one another. Some of the worlds have no animal or vegetable life nor any water. (trans Guthrie, 1965)

This description, despite being over 2,400 years old, is remarkably accurate and insightful. Since 1995, we have confirmed thousands of extrasolar planets, many within the past few years, spanning a remarkable range of sizes, compositions, and distances to their host star. Indeed we expect some to have life and others to remain lifeless. We even expect some to be destroyed by collisions, as Democritus intimated, or gobbled up by their host star as the planet migrates inward.

In our discovery of extrasolar planets, the one predictable fact is that the Universe is full of surprises. Every type of planet we can imagine and also the ones we can't imagine, exist. Last year a planet which contradicts theoretical predictions was found, Kepler-10c (Dumusque et al. 2014). Weighing in at 17 $M_\oplus$, Kepler-10c is too massive to be rocky by formation models, yet the density is clearly rocky at 7.1 ± 1.0 g cm^{-3} (Earth's density is 5.5 g cm^{-3} for comparison).

In 1995, the first extrasolar planet around a Sun-like star was so alien, so unexpected, that my advisor Dimitar Sasselov at first couldn't process the orbital parameters he saw on the poster and heard from Michel Mayor. Conventional wisdom held that Jupiter-sized planets would reside in far-out orbits from the star, based on our understanding of their formation. Jupiter-sized planets need the larger "feeding-ground" found farther from a star where ices and solids in the primordial disk allow Jupiters to accumulate enough mass to retain their large gaseous envelopes. This Jupiter-mass companion, as Mayor reported to the rapt audience, had a period of only four days (Mayor & Queloz 1995). Mercury, the planet closest to our Sun, orbits every 88 days, and is a baked, dead surface, and Jupiter, the first gas giant in our system orbits every 12 years. A planet so close it orbits every few days and as large as Jupiter had never even been dreamed of as a physical possibility.

The day before the talk, Dimitar walked up to Michel's poster, curious to learn more, but also skeptical. He listened to Mayor's explanation of the data, but was stumped by the non-intuitiveness of it. Despite the clearly labeled axes on the graph and the verbal explanation from Mayor, my advisor still misheard the orbital period of the planet to be 400 days, unable to comprehend 4 days. Even at 400 days he thought there is no way this is a true discovery of a Jovian planet. Imagine his surprise when the next day at the talk Mayor emphasized the period was a mere 4 days, not the 400 days my advisor had already thought implausible. Yet the discovery was robust and since then many more such hot Jupiters have been found. Due to the detection bias of the radial velocity technique, it is little wonder the first decade of planet hunting was filled with these enigmatic, hot, massive planets. Today we know there is roughly one hot Jupiter around every hundred sun-like stars (Howard et al. 2012).

Another such paradigm shift leapt forward exoplanet research in 1998, when then Harvard graduate student, Dave Charbonneau (and now my thesis chair), did a back-of-the-envelope calculation causing him to hypothesize that planets, orbiting with just the right orientation, could be detected by the slight dimming of star light when the planet crossed in front. These transits would offer another key piece of the puzzle, the size of the planet, which combined with the radial velocity (RV) mass yields a density and a constraint on the composition (see Fig. 2). Charbonneau calculated that a hot Jupiter exoplanet would be detectable in 1 out of every 10 planet-hosting stars using the STARE telescope Project Schmidt camera located in Boulder, Colorado. Driving across the country, Charbonneau set up the camera in an empty parking lot and observed ten stars before finding a transit signal. Harvard professor Ramesh Narayan remembers being particularly concerned, chuckling, “I thought we had lost him and he would never graduate.” Thus the first transiting planet, HD 209458b, was discovered (Charbonneau et al., 2000).

In the vast array of possible planets, one particular type captures the rapt attention of layman and astronomer alike – habitable planets. Habitable is, in the absence of any other example of life, taken to mean habitable for Earth life, all of which requires liquid water. Thus, for a planet to be habitable, we require that the planet has a definable surface, i.e. is rocky or terrestrial rather than gaseous, and that water could be stable on the surface.

Two detection methods in particular have been the most fruitful: the radial velocity method and the transit method. For both of these techniques, larger, closer-in planets are easier to detect and so the history of exoplanets has comprised a journey from large planets to small, and from boiling hot planets to cool. This path culminates in a final goal: finding and characterizing an Earth-like planet in the Habitable Zone (HZ) around an FGKM star.

1.2 Characterizing the Atmospheres of Exoplanets

NASA's *Kepler* satellite has advanced the field of exoplanet science immeasurably. We now know, statistically speaking, that nearly every star in the galaxy hosts at least one exoplanet (Fressin et al. 2013; Dressing & Charbonneau 2013; Swift et al. 2013) and that small planets are much more common than large gas giants, at least at small periods (Howard et al. 2012). One of *Kepler's* science goals was to determine, $\eta_\oplus$, the frequency of Earth-sized planets in the Habitable Zones of Sun-like (FGK) stars. Unfortunately, *Kepler's* 2nd reaction wheel failed before a robust value for $\eta_\oplus$ was determined. For M stars, the sample is more complete due to their close in HZs. Using Q1-Q17[1] *Kepler* data sets, estimates of $\eta_\oplus$ for M dwarfs range from 0.172 to 0.454 for planets with radii from 0.8 to 2.0 $R_\oplus$depending on the definition of "habitable" (see next section and Dressing & Charbonneau 2015). For FGK stars, the *Kepler* data sets need to be extrapolated to reach longer periods. Determining a false positive rate of 12.3% in the Kepler light curves, Fressin et al. (2013) calculates 14.9 ± 2.4% of FGK stars host Earth-sized planets (0.8 - 1.25 $R_\oplus$) with periods ranging from 0.8 to 50 days. The occurrence rate for habitable planets around GK stars is estimated to be around 22% Petigura et al. (2013)

---

[1] the first four years of observations

or 6% Foreman-Mackey et al. (2014) depending on the assumptions used, but in both cases adopting a very generous HZ of 1/4 to 4 times Earth insolation (0.5 to 2 AU).

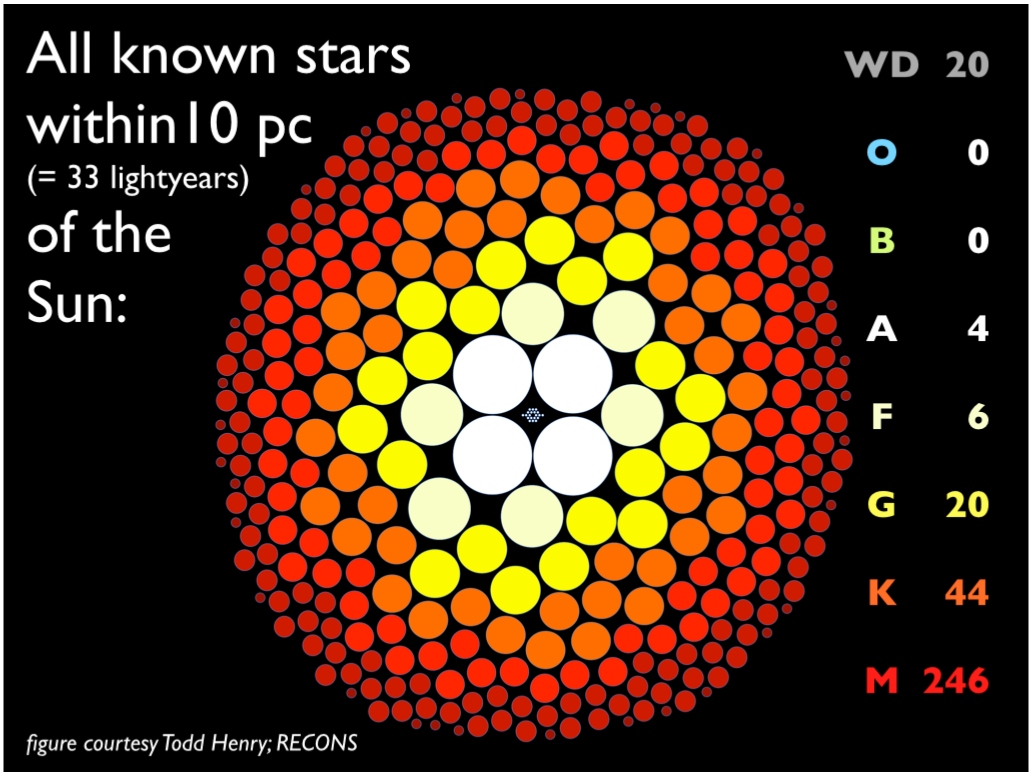

Figure 1.2: Graphical representation of all stars within 10pc. Figure credit: RECONS.

Knowing the value for $\eta_\oplus$ is vital when planning future direct detection or transiting planet missions to characterize atmospheres of terrestrial exoplanets. The transit probability for an Earth-like planet in the habitable zone orbiting an M dwarf is around 1/50 while it is 1/200 for a Solar analogue. Given the higher transit probability and that 75% of our solar neighborhood stars are M dwarfs, the first habitable planet to be characterized will likely be transiting a nearby M dwarf (see Fig. 1.2 for a graphical representation of all stars within 10 pc). M dwarf planets are prime targets for transiting missions but are not easily accessible to future direct detection missions due to their close in habitable zones. F & G stars, with their low transit probabilities but further out HZs will be ideal targets for future direct detection missions. K stars sit nicely between the two extremes and should be accessible to both direct detection and transiting planet missions. In addition, K dwarfs are better RV targets than M dwarfs due to higher intrinsic luminosity at bluer wavelengths where most spectrographs are optimized. However, occurrence rates for planets orbiting K dwarfs have been historically less pursued and may be confounded by errors in their stellar parameters.

A few current assumptions need to be improved in order to get a robust value for $\eta_{\oplus}$ for FGK stars. Petigura et al. (2013) and Foreman-Mackey et al. (2014) did not account for multiple planets per star and considered only the most easily detectable planet in a system. Habitable planets, however, are often at longer periods and lower masses than other planets in a multi-planet system and are therefore more difficult to detect. Accounting for multiple planet systems will increase the estimated occurrence rate. It is important to also consider biases in the sample. *Kepler* stars are on average slightly older and more metal poor than stars in our solar neighborhood. Thus the occurrence rates could vary slightly with metalicity and age since there is a correlation with metallicity for the occurrence of giant planets as well as for smaller planets[2] (Wang & Fischer 2015).

Given the current estimates for occurrence rates from *Kepler* for habitable planets, there should be a transiting habitable planet orbiting an M dwarf within 10.6pc and a non-transiting habitable planet within 2.6pc for an M dwarf or within 10pc for an F or G

---

[2] The correlation is weaker with metallicity for smaller planets but still significant. Wang & Fischer (2015) find a 9.3x and 1.72 increase for gas giants and terrestrial planets, respectively

star (Dressing & Charbonneau 2015; Foreman-Mackey et al. 2014; Petigura et al. 2013).

1.2.1 What is Habitable?

All of the above estimates for $\eta_{\oplus}$ depend on how one chooses to define the Habitable Zone. It's important to note that when talking about the HZ, we focus on the remotely detectable HZ. In our own solar system, there are many environments habitable for Earth-like life such as in the subsurface ocean of Europa or subsurface Mars. However these environments, given our inability to remotely detect any signs of life from subsurface environments on Mars or Europa whilst next door from Earth, would be completely inaccessible on extrasolar planets at interstellar distances. Thus, while many orbital distances are expected to be suitable for life in niche environments on a rocky planet, the HZ concept relies on a global biosphere interacting with the atmosphere. Because all life on Earth uses water as a solvent, the first HZ environments we are searching for require liquid water on the surface of a rocky planet.

It is possible that alien life exists in Titan-like environments with a hydrocarbon solvent, but until more research is done in synthetic biology, we would not be able to recognize those biosignatures. Probes to Titan will be pivotal in understanding possible alternative biochemistries. However, since water and carbon are both abundant in the Universe, our first steps to finding alien life around another star will be probing a parameter space that we know can yield biology.

Research groups take different approaches when defining the habitable zone. The classic circumstellar HZ for FGKM stars based on liquid surface water was first defined in Kasting et al. (1993) and estimated to be 0.95[3] - 1.67 AU.[4] Kasting used a 1D climate code with the inner edge assumed to be when either the planet absorbs more energy than it can emit or water increasingly is lofted to the stratosphere and photolyzed leading to an irreversible loss of H to space (i.e. a runaway greenhouse). Either condition could trigger the other, causing a permanent loss of water and a run-away greenhouse event as is assumed to have taken place on Venus. For planets with an Earth-like water inventory, the water vapor absorption features can become broad enough to close all windows in the infrared region in the atmosphere, thereby capping the amount of mid-infrared radiation that can be successfully re-emitted to $\sim$291 W/m^2 (Kasting 1988; Kopparapu et al. 2013; Goldblatt et al. 2013). Recent updates to include collisional induced absorption and new absorption coefficients calculated from HITEMP have moved the HZ uncomfortably close to Earth's orbit at 0.97 AU or 0.99 AU (or in terms of the effective solar flux, S_{eff} = 1.04 or 1.01) for the runaway or moist greenhouse limit, respectively.

The inner edge can be further moved inward due to clouds/hazes or a drier "Dune-like" planet. A planet with 100% global cloud cover will have a much higher albedo and therefore extend the HZ inward to 0.5 AU (S_{eff} = 4) (see Selsis et al. 2007). One concern would be that such a planet would block access to atmospheric features below the cloud layer in the visible region or in transmission spectroscopy. Indeed, many of the first planets characterized display a flat transmission spectrum, indicative

---

[3] 0.95AU is the run-away greenhouse limit. The moist greenhouse limit is 0.84AU (Kasting 1992).

[4] Note: when HZ limits are given in terms of AU, this is assumed for present solar luminosity. Alternatively HZ limits are quoted in terms of solar flux, but this number will also need to be adjusted with stellar type due to the shift in the spectral energy distribution and increased or decreased Rayleigh scattering affecting planetary albedo.

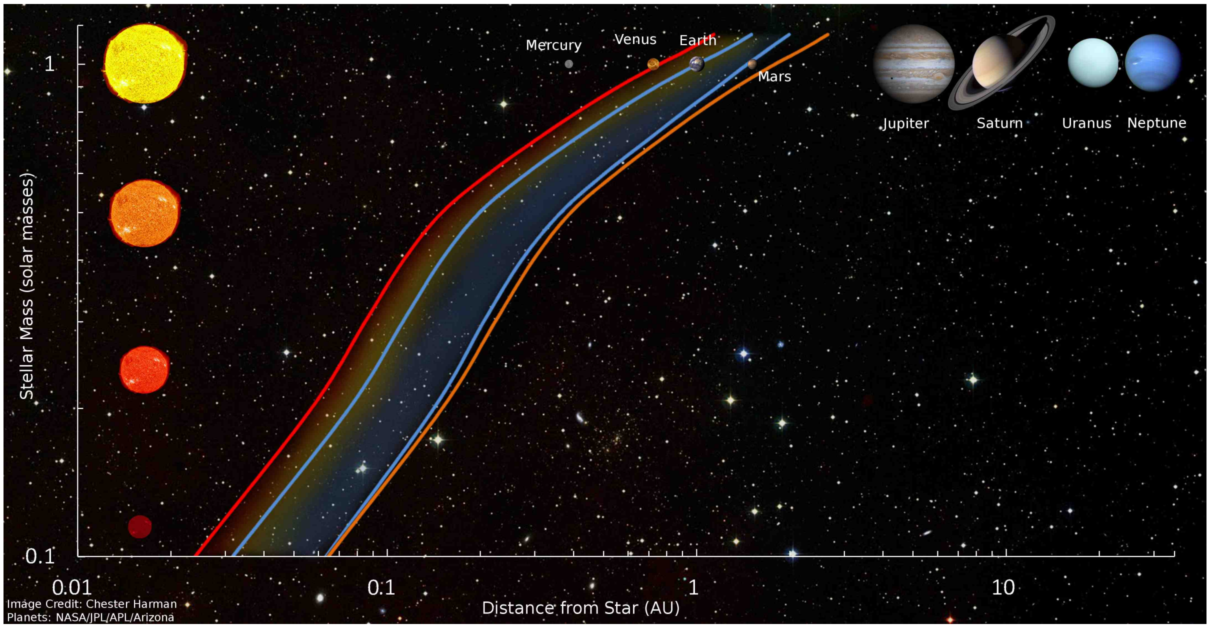

Figure 1.3: Habitable Zone around FGKM Stars with the Solar System planets for reference. Image Credit: Chester Harman

of clouds/hazes in the atmosphere or a high mean molecular weight atmosphere (see e.g. Knutson et al. 2014a,b; Ehrenreich et al. 2014; Kreidberg et al. 2014b; Crossfield et al. 2013; Berta et al. 2012). Although it has yet to be shown that a planet can be covered 100% by condensation clouds. A planet with 50% cloud cover, like Earth, would have an inner edge around 0.76AU (Selsis et al. 2007). A dry planet with 1-10% relative humidity of Earth could also move the HZ inward to 0.5 AU and 0.76AU respectively (Zsom et al. 2013; Abe et al. 2011). However such planets may not be geologically plausible given the propensity for rock and minerals to uptake water (Kasting & Harman 2013). Kasting & Harman (2013) argues that any limit inward of 0.59AU is unrealistic.

The outer edge of the habitable zone is defined to be the maximum distance where the addition of CO_2 creates more cooling due to Rayleigh scattering than heating. This limit may be further limited by including the effect of CO_2 clouds, which may reflect incoming radiation and increase the albedo of the planet, pushing it closer to a snowball scenario. However CO_2 clouds may also heat the surface by reflecting IR radiation back to the surface (Forget & Pierrehumbert 1997). Future research is needed to properly account for the radiative effects of CO_2 clouds. The outer edge based on the maximum greenhouse effect of CO_2 is 1.67 AU ($S_{\mathrm{eff}}-0.36$)

The HZ may also be extended outward by considering an enhanced greenhouse effect from H_2. Because H_2 is non-condensible (unlike CO_2 and H_2O) and doesn't reflect at short wavelengths, large abundances of this greenhouse gas can extend the HZ for terrestrial planets out to $\sim$10AU (Pierrehumbert & Gaidos 2011; Wordsworth & Pierrehumbert 2013). However, which biosignatures would be present and observable on such a planet has not been worked out. Using direct detection methods, such a planet would have a contrast ratio in the visible 100 times worse than an Earth-Sun analogue due to larger orbital distances.

The above HZs are mostly from 1D climate code calculations (Abe et al. (2011) uses a 3D code). However there is another HZ definition, the empirical HZ, often preferred since 1D cloud models do not include cloud feedback. The inner edge of the empirical HZ is the flux received by "recent Venus" 1 Ga since Venus is thought to not have had liquid water on the surface for at least one billion years (Solomon & Head 1991). The outer edge is based on early Mars at 3.8 Ga when it is thought liquid water flowed on the red planet. The empirical HZ limits are 0.75 AU - 1.77 AU.

Often quoted in the literature is the equilibrium temperature of a planet, T_{eq} with an assumed albedo usually taken as the the Bond albedo of modern Earth, 0.3 for any orbital distance and surface pressure. However planets near the inner edge of the HZ are predicted to have Bond albedos closer to 0.2 and near the outer edge closer to 0.4 (Kasting et al. 1993). As well, the planetary albedo changes dramatically with stellar type and atmospheric composition due to variation in Rayleigh scattering from the availability of short wavelength photons (see Chapters 2, 3 and 5 or Rugheimer et al. 2013, 2015a,b). Without knowing the atmosphere or albedo of the planet, T_{eq} has limited utility.

All of these different Habitable Zones beg the question: which should we choose when designing the next mission? Kasting & Harman (2013) argue, and I agree, that the conservative limits should be used when determining $\eta_{\oplus}$ and building the minimum size of telescope. This is to ensure that we at least observe the target number of planets we aim to characterize which have the potential to be Earth-like. But when actually searching for other interesting worlds, we should be more liberal in our limits. We will certainly discover interesting worlds no matter where we look around a star. Characterizing planets in the more optimistic HZ will also provide interesting clues valuable in settling the modeling debates described above.

1.3 Advances in Modeling

Detecting potentially habitable planets is the first step to finding an *in*habited world outside the solar system. The second step will be to characterize their atmospheres and to search for biosignatures and habitability markers. The best studied super-Earth is GJ 1214b orbiting a nearby M dwarf (Charbonneau et al. 2009; Berta-Thompson et al. 2011). Even with 15 transit observations by the Hubble Space Telescope (HST), the visible and near-infrared transmission spectrum is flat, ruling out a high mean molecular weight atmosphere and indicating the presence of clouds or hazes blocking the spectrum below (Kreidberg et al. 2014b). GJ 1214b is a super-Earth sized object orbiting too close to it's parent star to be habitable. No telescope is currently able to detect biosignatures in the atmosphere of a rocky exoplanet in the HZ. The first missions capable of detecting the atmospheres of habitable planets will be the James Webb Space Telescope (JWST) or large ground based observatories such as the Giant Magellan Telescope (GMT) and the European Extremely Large Telescope (E-ELT). Horizon missions such as Exo-S, Exo-C, and the High Definition Space Telescope (HDST) will have the capability to observe smaller and more terrestrial planets through direct detection spectroscopy.

My thesis focuses on forward modeling of habitable extrasolar worlds orbiting different stars in order to determine viable observational strategies, expectations, and resolution required for future missions. Remotely detectable spectral modeling has two main sub-disciplines: retrieval modeling and forward modeling. Retrieval models attempt to tease out which molecular constituents in an atmosphere could fit the observed data. Creating accurate retrieval models is a necessary preparation for future detections of planetary atmospheres. However, retrieval models do not generally provide physical understanding of the atmospheric chemistry and geobiology responsible for the atmosphere. Forward modeling uses known physics, geology and chemistry to simulate physically motivated atmospheres and spectra to create a phase space on which to interpret future observations. Both retrieval modeling and forward modeling constitute vital theoretical backbones for the next few decades of exoplanet observations.

Since I started graduate school, there have been several notable advances in theoretical modeling. One hotly debated topic currently is recent work on abiotic oxygen formation. It has been known that abiotic oxygen can be formed through photolysis of

H_2O in a run-away greenhouse scenario. Thus, the most reputable biosignature has been the combination of an oxidizing and reducing gas together in chemical disequilibrium as first postulated by Lederberg (1965); Lovelock (1975). Yet it is important to note that the absence of an extremely thermodynamic disequilibrium state such as $O_2/O_3 + CH_4$ doesn't mean there is no life. Earth's biosphere flourished long before O_2 was present in the atmosphere. There are also examples of abiotic atmospheres out of thermodynamic equilibrium, such as an atmosphere with H_2 and CO (Kasting et al. 1993).

Seager et al. (2012, 2013) proposes an interesting framework for the classification of biosignatures. Type I biosignatures are redox gradient energy extraction by-products such as CH_4 or NH_3. This means these biosignatures will always have a high chance of a false positive since they are energetically advantageous for biology as well as geology (any reaction with a negative Gibbs free energy). One exception is N_2O, which is considered a Type I biosignature, although it doesn't have any known abiotic sources and thus is considered a strong biosignature by itself. Type II biosignatures are biomass building by-products like O_2. Type II reactions require energy, such as sunlight driving photosynthesis. Type III biosignatures are secondary metabolic byproducts which are produced by life for functions such as defense, signaling, or physiological control. These highly specialized gas byproducts are typically not produced in high abundance but since they are specialized, they often are not naturally occurring and thus the false positive rate is low. Two examples of Type III biosignatures are DMS (dimethyl sulfide) and CH_3Cl. These gases are typically photolyzed quickly and therefore may be detectable only on planets with a low UV environment. Seager et al. (2013) calculates the minimum spectral feature needed for detection and then attempts to calculate the source flux and if the biomass necessary to produce such a signature is reasonable (See Fig. 1.4).

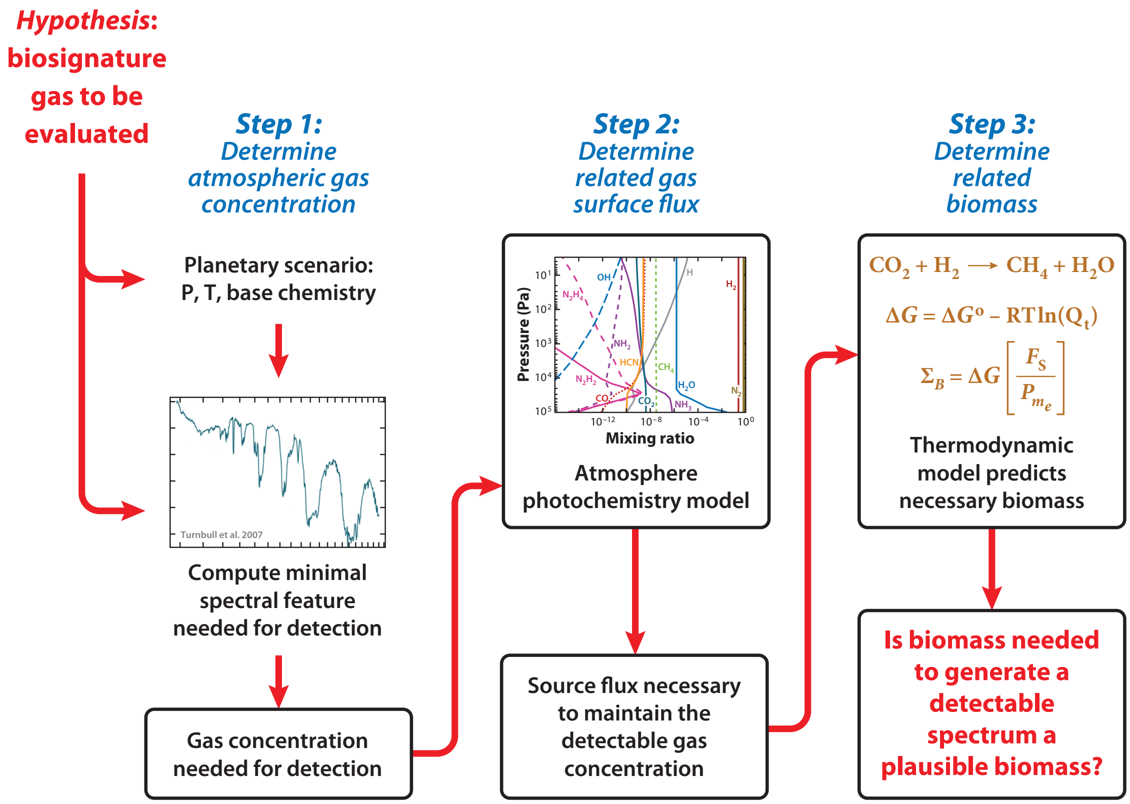

Figure 1.4: Schematic on how to identify remotely detectable biosignatures (Seager et al. 2013).

I am often asked, "why would we expect oxygenic photosynthesis on another planet". While it is true that we only have one example of evolution of life in the Universe, there are physical reasons to assume evolution on another planet would stumble upon oxygenic photosynthesis eventually. One reason is that in an atmosphere where available carbon is found predominately in CO_2, oxygen is the most plausible oxidized by-product to reduce CO_2 to biomass. A second reason is oxygen has over twice the redox potential as the next highest oxidizer. The high amount of energy available for a redox gradient from oxygen is thought to be necessary for the evolution of complex multicellular life.

Recently, several groups have looked into the possibility of detectable levels of abiotic oxygen and ozone formation in CO_2-rich planets orbiting M dwarfs (Hu et al. 2012; Tian et al. 2014), around FGKM stars with low-H_2/high-CO_2 atmospheres (Domagal-Goldman et al. 2014), around pre-main sequence M stars (Luger & Barnes 2014), or in low pressure atmospheres (Wordsworth & Pierrehumbert 2014). In particular, Domagal-Goldman et al. (2014) predicts simultaneously detectable levels of abiotic O_3 (in the Hartley band) and abiotic CH_4 in the UV-VIS region of the spectrum of a theoretical planet around an M star, GJ 876. Thus, this combination of O_3 and CH_4 will not be a strong biosignature without the additional detection of O_2 in the VIS or the detection of O_3 in the IR, both of which do not build up to detectable levels through abiotic formation. However as my research shows, the O_2 feature at 0.76μm is much more difficult to detect for planets around late M stars (M7V-M9V) even at modern Earth levels (21%) (Rugheimer et al. 2015b). When modeling abiotic O_2, it is important to account for geological sinks via reductants in the surface or oceans and reasonable boundary conditions for the deposition velocities of H_2, CO and O_2 which are currently disputed. Using two different atmospheric boundary conditions for these three species Tian et al. (2014) and Domagal-Goldman et al. (2014) find 4 orders of magnitude difference in the O_2 column depth for the same atmosphere and stellar flux. For a more detailed discussion of details of redox reactions and boundary conditions used in the models finding abiotic O_2/O_3 see Domagal-Goldman et al. (2014). Any future detections of potential biosignatures will need to be carefully vetted in the context of their planetary and stellar environments to identify false positives such as photolysis of H_2O or CO_2.

One possible way to distinguish between abiotic and biotic origins of O_2 is to use the O_2 dimer to get an estimate of the partial pressure of O_2 (Misra et al. 2014). The

O_2-O_2 dimer absorption feature at 1.06μm or 1.27μm in the NIR could be detectable in transmission during transit with JWST. In combination with the O_2 feature at 0.76μm, one can determine the surface pressure of the planet. The O_2 dimer is present in the spectrum for atmospheres with terrestrial levels of O_2 and greater at 1.27μm and at 200% terrestrial O_2 (42%) concentrations for the 1.06μm dimer (Misra et al. 2014). However, it is thought that any partial pressure above $\sim$ 30% O_2 would result in wide-spread fires. O_2 concentrations as high as 30% are thought to have occurred in during Earth's Carboniferous period (Berner 1999) but may have resettled back to our 21% due to fire feedbacks. Misra et al. (2014) also shows that the primary O_2 feature at 0.76μm is not detectable above a SNR of 1.1 with JWST for any O_2 concentration up to 42% or atmospheric pressure up to 10 bars. Thus, a detectable feature with currently planed missions may not be physically plausible. Another way to determine atmospheric pressure could be to observe $(N_2)_2$ dimer suppression of the disk integrated spectrum in the 4.0-4.2μm region that indicates higher atmospheric pressures (Schwieterman et al. 2014), though it will be difficult to detect $(N_2)_2$ in low resolution spectra.

One exciting possibility is the detection of biogeochemical cycles on exoplanets. Detectable amounts of SO_2 (levels as low as 1ppm) in low resolution in the IR can be reached in large volcanic eruptions and have no other large atmospheric source (Kaltenegger & Sasselov 2010; Kaltenegger et al. 2010). For a high spectral resolution instrument, a second by-product of volcanoes, H_2S may become detectable. In a planet with extreme volcanism, the sulfur cycle could dominate (Kaltenegger & Sasselov 2010).

Also, by using the colors of extrasolar planets, we can prioritize which planets to follow-up with higher resolution spectroscopy (Hegde & Kaltenegger 2013). Such colors may indicate surfaces and habitable niches for extremophiles. A color-color diagram also distinguishes giant from rocky planets in our solar system and provides an estimate for basic physical properties and general atmospheric composition (Traub 2003b,a; Crow et al. 2011). While the vegetation red edge at 0.7μm on Earth indicates reflection of widespread planet coverage, extremophiles may have a similar impact on the color of a pre-complex life world (Hegde & Kaltenegger 2013).

The atmospheres of planets are inextricably linked to the interior of planets. Schaefer & Sasselov (2015) details the deep water cycle on super-Earths and how this is linked to surface water content. Our work on *Kepler*-62*e* and -62*f* shows that such water worlds could be distinguishable from rocky worlds in transmission spectroscopy (Kaltenegger et al. 2013). Levi et al. (2014) shows that methane can be taken up in clathrates and incorporated into high pressure ices. Such ices may be common at the bottom of oceans and could act as a way to cycle greenhouse gases like CH_4 and CO_2 through modes of ice plate tectonics. My fellow grad student, Li Zeng, wrote a nice applet to explore the compositions of planets and interior structures for rocky planets (applet on www.astrozeng.com detailed in Zeng & Sasselov 2014, 2013).

Another advance in atmospheric modeling has been in simulating ultra-high resolution ground spectroscopy observations with a extremely large telescope like the GMT or E-ELT. Previously, the consensus was that most Earth-like exoplanet atmosphere observations would need to occur from space to avoid confusion with Earth's atmospheric lines. Snellen et al. (2013) demonstrated that by using the doppler shift of the planet, one can see the shift in the exoplanet atmosphere lines compared to the stationary Earth atmospheric lines if a resolution of $\sim$ 100,000 is used. Rodler & López-Morales (2014) used the modern Earth atmosphere to simulate the detection of the 0.76μm feature from the ground.

My thesis is focused on modeling the effect of UV irradiation and stellar spectral type on planetary atmospheres and their remotely detectable emission spectra. In the second chapter, I present a detailed suite of stellar models for FGK stars with UV data from the IUE satellite ranging from T_{eff}=7000K to 4250K (in 250K steps). I first validated our model against EPOXI observations of Earth, the most comprehensive dataset of Earth as a directly-imaged exoplanet. I targeted the importance of UV vs stellar effective temperature by creating toy model stellar spectra, where I changed only the UV or SED portion of the spectrum to separate the effects of specific changes in stellar radiation on the salient planetary physics and atmospheric chemistry. Previously, planets orbiting main sequence F stars were thought to have an ozone feature that is difficult to detect (Selsis 2000). I showed that for planets orbiting the hottest F stars, the ozone feature at 9.6μm is detectable and is in emission. I also examined the effect of clouds on the VIS – IR spectrum and the detectability of spectral features including biosignatures and surface vegetation.

Since M dwarfs remain active for longer than FGK stars and span three orders of magnitude in luminosity, in the third chapter I present extensive models for the entire M dwarf spectral class, with separate models for active (AD Leo type stars), medium-active (MUSCLES stars), and inactive stars (PHOENIX models). My active and inactive stellar models represent extreme limits and are separated by up to 25 orders of magnitude in UV flux. In this chapter, I also examine the possibility of detecting N_2O as a biosignature and the effect of Ly-α on a terrestrial planet atmosphere. M dwarfs may also be more resilient against global glaciation than FGK stars (Shields et al. 2013, 2014)

In the fourth chapter, I model conditions for the UV surface environments for geological epochs through Earth's evolution. I explored four different atmospheres corresponding to an early Earth atmosphere at 3.9 Ga (pre-biology) and three atmospheres covering the rise of oxygen to present day levels at 2.0 Ga, 0.8 Ga and modern Earth for the grid of FGKM host stars from chapters 1 and 2. To estimate biologically relevant UV fluxes, I calculated damage to DNA and other carbon-based biomolecules. My models provide boundary conditions for the UV environment on the surface of Earth-like exoplanets orbiting a variety of stellar types to inform photo-biological assessments, pre-biotic chemistry, and early life evolution experiments.

In the fifth chapter, I model the observable spectra for planets at different geological epochs orbiting FGKM stars. In these models, I show when O_2/O_3 is detectable in combination with CH_4. Modeling atmospheres representing different geological epochs will provide a framework for identifying the possible stages an exoplanet is in during its own planetary history.

In my thesis work, I've been fortunate enough to have modeled a wide variety of terrestrial planet atmospheres from prebiotic worlds, early-life worlds, ocean planets, mini-Earths, super Earths, and the first known exoplanet system with two Super-Earth sized planets in the same HZ (see Kaltenegger et al. 2013; Rugheimer et al. 2013, 2015b; Miguel et al. 2015). These projects along with my proposed postdoctoral work, provide predictions to prepare for future exoplanet observations with JWST and other telescopes.

1.4 Future Missions

The James Webb Space Telescope (JWST) is scheduled to launch in 2018, with the capability to observe the atmospheres of potentially habitable transiting exoplanets by the transit method. When a planet transits we can measure the depth of the transit at different wavelengths. Since molecules absorb at specific frequencies, it is possible to tease out the presence of an individual molecular species. One important effort will be uncovering recognizable biosignatures indicative of a planet similar to Earth. Direct detection technologies such as starshades and coronographs are also being pursued to maximize our chances of finding evidence of a second origin of life in the Universe.

The first step toward detecting atmospheric features was taken already a decade past when sodium was measured with the Hubble Space Telescope in the atmosphere of HD 209458, the same planet found by Charbonneau in the Colorado parking lot (Charbonneau et al., 2002). This represented the first observation of an element in the atmosphere, and indeed the atmosphere itself, of an extrasolar planet.

A few years ago, a team at Jet Propulsion Laboratory analyzed the transit of HD 189733b in the infrared portion of the spectrum at 3.6μm, 5.8μm, and 8μm using the Spitzer Space Telescope and inferred the presence of water and methane in the atmosphere (Tinetti et al, 2007; Swain et al., 2008). However, these features may be alternatively explained by Rayleigh scattering combined with a featureless spectrum (Pont et al., 2012). A sobering paper by Hansen et al. (2014) demonstrated how many of the single eclipse “detections” with Spitzer have no statistical significance over a blackbody fit since the errors may be larger than previously assumed. Pushing into the limits of the systematics of Spitzer and making overreaching claims is a cautionary tale for future terrestrial atmosphere observations with JWST. Most recently, water has been more definitively detected using HST in the atmosphere of a hot Jupiter, WASP-43b (Kreidberg et al. 2014a).

The detection of atmospheres on other worlds is already a difficult endeavor for large, gaseous planets, as seen by how hard it is to conclusively detect even strongly absorbing species like water and carbon dioxide. This difficulty is only intensified for small and potentially rocky worlds – but the ambition to make the first discovery is strong and care must be taken to avoid over-interpreting models (Hansen et al. 2014). Each year observers push the detection limits to smaller and more Earth-like exoplanets. GJ 1214b is a mere 6.3 Earth masses, one of the nearest known cousins to Earth, but early observations couldn't distinguish between a high mean molecular weight atmosphere (perhaps water dominated) or a cloudy/hazy atmosphere (Berta et al. 2012). Earlier this year with 15 HST transits, Kreidberg et al. (2014b) demonstrated GJ 1214b is featureless with a cloud/haze blocking access to the lower atmosphere. Water has also been claimed in the atmosphere of a Neptune-sized planet, HAT-P-11b with observations by HST and Spitzer (Fraine et al. 2014).

The Transiting Exoplanet Survey Satellite (TESS) is slated for launch in 2017 with the goal of detecting nearby transiting planets (Ricker et al. 2014). TESS will be sensitive primarily to shorter period exoplanets will concentrate on spectral types F5 - M5 and monitor of 200,000 main sequence stars. The period sensitivity chosen accommodates Earth-like planets in the HZ of M dwarfs, which will be prime follow-up targets for radial velocity mass measurements and characterization with transit spectrophotometry with JWST. CHaracterizing ExOPlanet Satellite (CHEOPS) is also a 2017 European mission to follow-up known RV planets to search for transits over a 3.5 year mission lifetime (Broeg et al. 2013).

In 2018, JWST will start a new era of exoplanet characterization. At 6.5 m, JWST will be able to easily characterize the atmospheres of hot Jupiters. For smaller, Earth-like planets, JWST may be able to detect biosignatures for the closest habitable worlds by adding together enough transits to get the 10s-100s of hours required for characterization (Kaltenegger & Traub 2009; Deming et al. 2009). Habitable planets transiting M stars will be the most amenable to follow-up observations given their high abundance in our solar neighborhood, large planet to star radius ratio, and shorter orbital periods. Two instruments will be key for exoplanet characterization: MIRI[5] covering 5-28μm and NIRSpec[6] from 0.6-5 μm. Some molecules with strong absorption, such as as O_3, H_2O, and CO_2 will take fewer transits to detect for small terrestrial planets. CH_4 will be particularly difficult at Earth-level concentrations even with 200 hours of JWST time (Kaltenegger & Traub 2009), although CH_4 is an important feature to pair with O_3. Typically RV follow-up is used to obtain mass measurements which when paired with the radius derived from the transit method provides a bulk composition estimate, though it may be possible to get a mass estimate from transmission spectroscopy alone (de Wit & Seager 2013).

Another challenge for JWST is that atmospheric refraction fundamentally limits the depth probed during primary eclipses (Bétrémieux & Kaltenegger 2013). During a transit event, light is scattered away from the observer when refracted from the deeper atmosphere. On the other hand, right before and after a transit, the deeper atmosphere is probed. With copious amounts of JWST time, determining altitude-dependent mixing ratio profiles might be possible (Misra et al. 2014). However due to the integration times required, this may only be possible for extrasolar giant planets in the near future. The

---

[5] Mid-Infrared Instrument

[6] Near-Infrared Spectrograph

critical deflection angle depends on the geometry of the system and therefore varies with stellar temperature for planets at equivalent T_{eq}. For the Earth-Sun system the limiting altitude probed during a transit is 12.7 km, and only for planets orbiting M dwarfs is the surface of a 1 bar N_2/O_2 atmosphere probed (Bétrémieux & Kaltenegger 2013).

TESS-JWST transiting surveys are very powerful, but are limited to the fraction of planets in ideal orbits that transit their star. Direct detection will increase the number of planets we can characterize, and therefore increases our chances of detecting biosignatures by not requiring the planet to transit. Feasible direct detection spectral characterization requires starlight suppression. Two methods are being pursued by NASA for further development: a starshade (EXO-S) and a coronograph (EXO-C) (Stapelfeldt et al. 2014; Seager 2014). A starshade would be deployed separately from the telescope and fly in formation several tens of thousands of kilometers away, effectively blocking the star while leaving the reflected light from the planet unscathed. The main advantages of starshades are that they are not limited by diffraction for the inner working angle, they can be flown after the main telescope has launched (and thus could be added to JWST), and they are based on an existing technology of radio antenna deployment (Seager 2014). A coronograph is a telescope attachment to block out light from a star so that the light from the planets in the star system can be imaged directly. While a coronograph is limited to a inner working angle of $\sim 2\lambda/D$, it has the distinct advantage of not needing to be repositioned when moving to a new target. Both EXO-S and EXO-C will need to overcome specific technology gaps before implementation (see Lawson et al. 2014, for a detailed review of existing and needed technology).

Several large ground based observatories are currently being built and scheduled to come online in the 2020s. The GMT[7] is a 24.5 m telescope being built by an international consortium of universities (including Harvard) and science institutions planned for completion in 2020 in Chile. The TMT[8] is a 30 m telescope with international collaboration from the US, Japan, China, Canada and India being constructed on Maunakea, situated at the highest altitude among the large observatories and scheduled for 2022 completion. The E-ELT[9] is a European 39.3 m telescope in Chile set for first light in 2024 with currently 90% of its funding secured. Each of these telescopes, using high resolution spectroscopy, such as METIS on the E-ELT with a R $\sim$ 100,000, may be able to separate out telluric lines and detect biosignatures around nearby habitable exo-Earths (Snellen et al. 2013; Rodler & López-Morales 2014).

On the long-term horizon, the AURA[10] report entailed "Beyond JWST: The Future of UVOIR Space Astronomy" has recommended the next flagship mission post JWST to be a 8-16 m space based observatory with coverage from Ly-α to 2.5μm and a spectral resolution of 50-500. The report is still in progress, but preliminary reports at this year's AAS were exciting for exoplanets to say the least. Currently nicknamed "HDST" for High-Definition Space Telescope, such an observatory could spatially resolve in the VIS every galaxy in the Universe down to 100pc, and everywhere in our Milky Way down to 100AU. Such a mission would be paired with a coronograph with an inner working angle of 2.5-3λ/D or an 80 m starshade to suppress starlight and directly image habitable

---

[7] Giant Magellan Telescope

[8] Thirty Meter Telescope

[9] European Extremely Large Telescope

[10] Association of Universities for Research in Astronomy

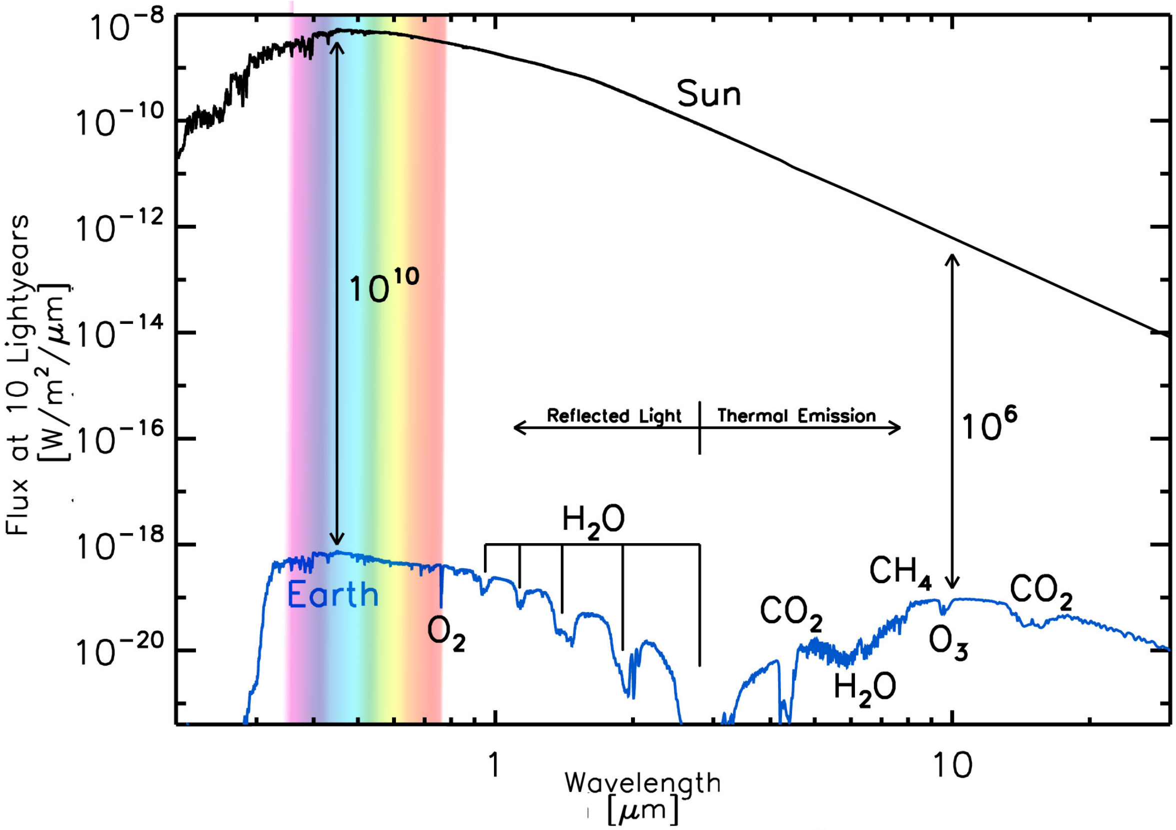

Figure 1.5: Earth reflected light and thermal emission flux (blue) compared with a Sun-analogue (black) at 10 ly. Note the contrast ratio (star flux to planet flux) is 10^{10} in the VIS and 10^6 in the IR. Figure credit: Ty Robinson created for Astrobiology Primer 2.0.

worlds. Fig. 1.5 shows the direct detection spectrum for Earth in relation to the Solar flux at 10pc. The coronograph and starshade proposed for HDST are designed to achieve a contrast ratio of 10^{10} needed for the VIS. The signal to noise would be sufficient to get diurnal variations in a nearby exo-Earth. The average time to launch from being selected for NASA flagship missions is 17 years, and so *if* chosen in the next decadal survey, HDST would fly around 2037.

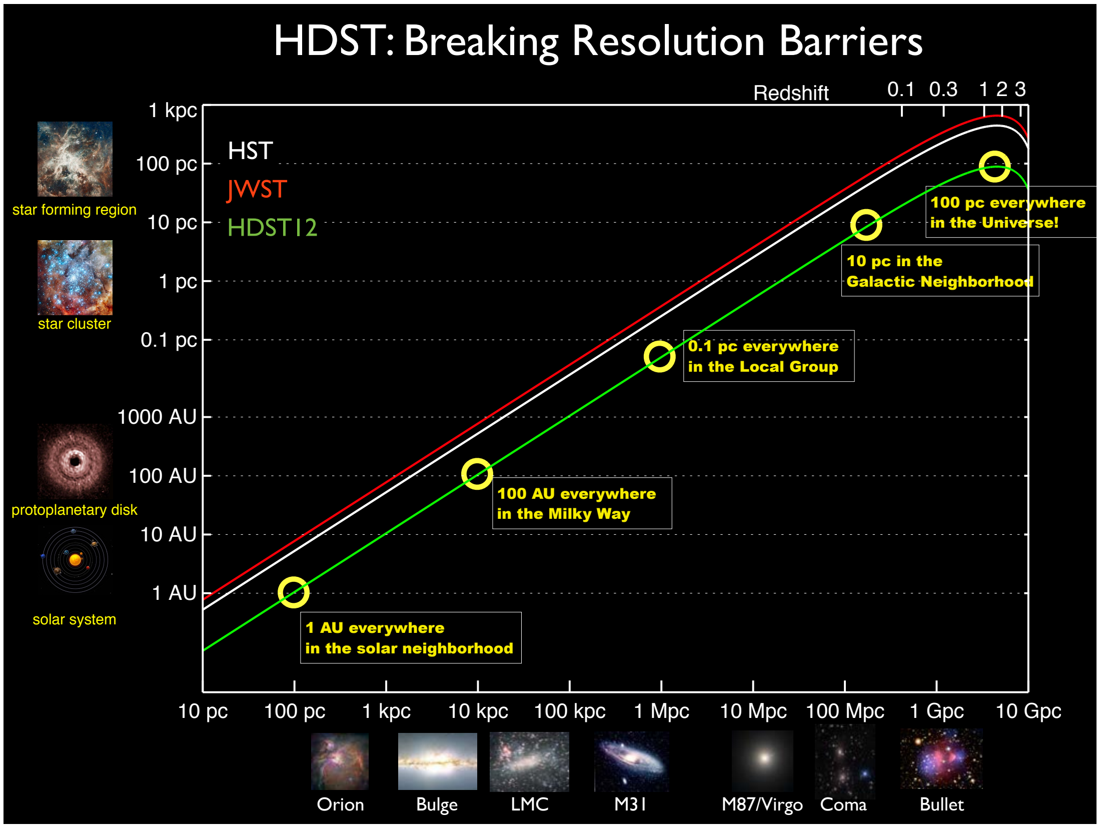

Figure 1.6: Spatial resolution capabilities of the proposed High Definition Space Telescope (HDST). Image from: www.aura-astronomy.org

1.5 The Last Generation of Lonely Astronomers

In 2013, we reached the era in which all graduating high-school students have never known a time in which our solar system planets comprised the only known worlds. For thousands of years scientists and philosophers supposed other planets must exist, yet there was no direct evidence until 1995. In the first discoveries we learned about a type of planet no one had ever even dreamed of – hot Jupiters. Then, in the past decade, Neptune-sized planets were discovered. And it is in the past few years and even months that we are pushing our detection limits toward true Earth-like planets. In 2012, an Earth-mass planet was found orbiting Alpha Centauri B (Dumusque et al. 2012). Though the planet is far to close to its star to be habitable, smaller planets are often not alone in their star system and Alpha Centauri is in our stellar backyard. Even more promising, in a press release at the 225th AAS meeting in Seattle, 12 habitable planets were announced with nine small enough to be rocky (Torres et al. 2015). While the Kepler field is too far away for characterization follow-up, such discoveries indicate that someday soon we will find Earth 2.0 in our solar neighborhood.

Eta-Earth, $\eta_{\oplus}$, is still a work in progress, but one exciting result from Kepler Space Telescope is that small planets are common, far more so than Jupiter-sized planets at our current detection sensitivities (Batalha et al. 2013; Howard et al. 2012). Furthermore, they appear to be common around the smallest stars, increasing our chances for follow-up observations with the next generation of missions. These discoveries are heartening for our prospects of finding and characterizing other Earths in the Habitable Zone in the next decade. With the launch of JWST and the construction of large ground based observatories we can proceed to the next landmark: devoting hundreds of hours of telescope time to the characterization of the atmospheres of these worlds, with a particular eye toward biosignatures.

The holy grail, combining these techniques and others, is to detect molecular species indicating habitability in the atmosphere of a terrestrial extrasolar planet. If we can find biosignatures, such as the combination of ozone and methane in the presence of habitability markers like water and carbon dioxide, we would potentially be finding not only a habitable planet, but perhaps an *inhabited* planet.

An alien astronomer based on similar carbon chemistry looking at Earth's spectrum would have several good lines of evidence through the presence of oxygen/ozone and methane to support a hypothesis that our Earth is inhabited in addition to being habitable. The possibility that the reverse is also true keeps me waking up every morning with excitement. Are we the last generation of lonely astronomers?[11] I hope so.

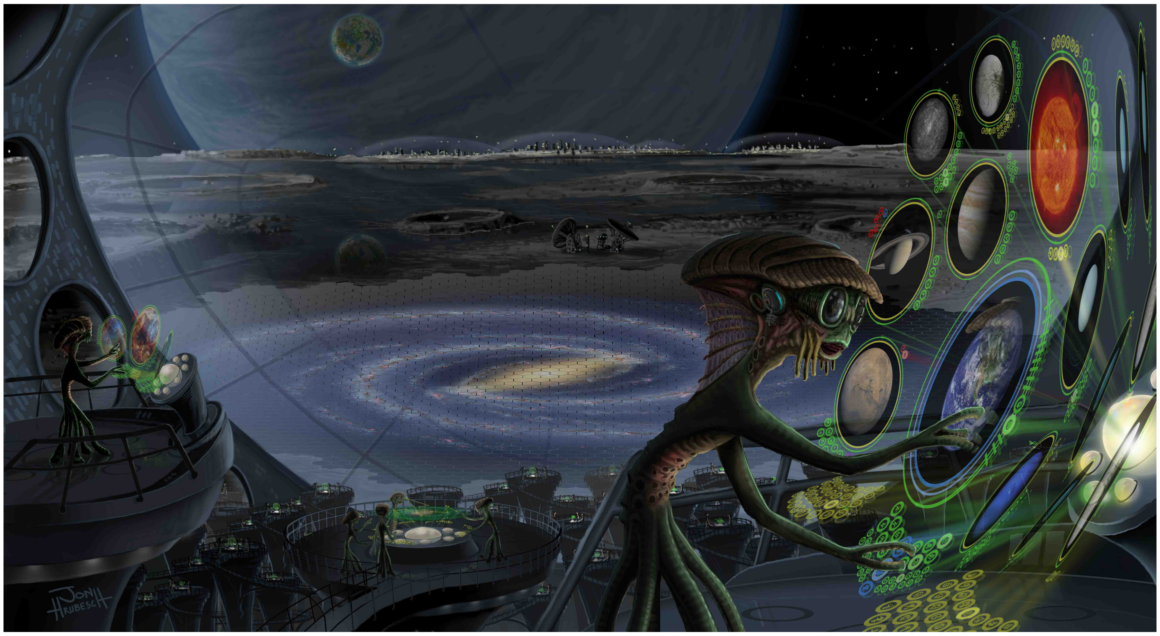

Figure 1.7: Alien Astronomer. Artwork used with permission, credit: Jon Hrubesch

---

[11] Question posed first by Dave Charbonneau.

Chapter 2

Spectral Fingerprints of Earth-like Planets Around FGK Stars

This thesis chapter originally appeared in the literature as

S. Rugheimer, L. Kaltenegger, A. Zsom, A. Segura, and D. Sasselov, *Astrobiology*, 13, 3, 2013

Abstract

We present model atmospheres for an Earth-like planet orbiting the entire grid of main sequence FGK stars with effective temperatures ranging from T_{eff} = 4250K to T_{eff} = 7000K in 250K intervals. We model the remotely detectable spectra of Earth-like planets for clear and cloudy atmospheres at the 1AU equivalent distance from the VIS to IR (0.4μm - 20μm) to compare detectability of features in different wavelength ranges in accordance with JWST and future design concepts to characterize exo-Earths. We also

explore the effect of the stellar UV levels as well as spectral energy distribution on a terrestrial atmosphere concentrating on detectable atmospheric features that indicate habitability on Earth, namely: H_2O, O_3, CH_4, N_2O and CH_3Cl.

Increased UV dominates changes of O_3, OH, CH_4, N_2O and CH_3Cl whereas the increase in stellar temperature dominates changes in H_2O. The overall effect as stellar effective temperatures and corresponding UV increase, is a lower surface temperature of the planet due to a bigger part of the stellar flux being reflected at short wavelengths, as well as increased photolysis. Earth-like atmospheric models show more O_3 and OH but less stratospheric CH_4, N_2O, CH_3Cl and tropospheric H_2O (but more stratospheric H_2O) with increasing effective temperature of Main Sequence stars. The corresponding spectral features on the other hand show different detectability depending on the wavelength observed.

We concentrate on directly imaged planets here as framework to interpret future lightcurves, direct imaging and secondary eclipse measurements of atmospheres of terrestrial planets in the HZ at varying orbital positions.

2.1 Introduction

Over 830 extrasolar planets have been found to date with thousands more candidate planets awaiting confirmation from NASA's Kepler Mission. Several of these planets have been found in or near the circumstellar Habitable Zone (see e.g. Batalha et al. 2013; Borucki et al. 2011; Udry et al. 2007; Kaltenegger & Sasselov 2011) with masses and radii consistent with rocky planet models. Recent radial velocity results as well as Kepler demonstrate that small planets in the Habitable Zone (HZ) exist around solar type stars. Future mission concepts to characterize Earth-like planets are designed to take spectra of extrasolar planets with the ultimate goal of remotely detecting atmospheric signatures (e.g. Beichman et al. 1999, 2006; Cash 2006; Traub et al. 2006). For transiting terrestrial planets around the closest stars, the James Web Space Telescope (JWST, see Gardner et al. 2006) as well as future ground and space based telescopes might be able to detect biosignatures by adding multiple transits for the closest stars (see discussion).

Several groups have explored the effect of stellar spectral types on the atmospheric composition of Earth-like planets by considering specific stars: F9V and K2V (Selsis 2000), F2V and K2V (Segura et al. 2003; Grenfell et al. 2007; Kitzmann et al. 2011a,b). In this paper we expand on this work by establishing planetary atmosphere models for the full FGK main sequence, using a stellar temperature grid from 7000K to 4250K, in increments of 250K, to explore the effect of the stellar types on terrestrial atmosphere models. We show the effects of stellar UV and stellar temperature on the planet's atmosphere individually to understand the overall effect of the stellar type on the remotely detectable planetary spectrum from 0.4-20μm for clear and cloudy atmosphere models. This stellar temperature grid covers the full FGK spectral range and corresponds roughly to F0V, F2V, F5V, F7V, F9V/G0V, G2V, G8V, K0V, K2V, K4V, K5V and K7V main sequence stars (following the spectral type classification by Gray 1992).

In this paper we use "Earth-like", as applied to our models, to mean using modern Earths outgassing rates (following Segura et al. 2003). We explore the influence of stellar spectral energy distribution (SED) on the chemical abundance and planetary atmospheric spectral features for Earth-like planets including biosignatures and their observability from the VIS to IR. Atmospheric biosignatures are chemical species in the atmosphere that are out of chemical equilibrium or are byproducts of life processes. In our analysis we focus particularly on spectral features of chemical species that indicate habitability for a temperate rocky planet like Earth, H_2O, O_3, CH_4, N_2O and CH_3Cl (Lovelock 1975; Sagan et al. 1993).

In §2.1 we introduce the photochemistry of an Earth-like atmosphere. In §2.2, we describe our model for calculating the stellar spectra, atmospheric models, and planetary spectra. §2.3 presents the influence of stellar types on the abundance of various atmospheric chemical species. In §2.4 we examine the remote observability of such spectral features, and in §2.5 and §2.6 we conclude by summarizing the results and discussing their implications.

2.1.1 Photochemistry for Earth-like planets including potential biosignatures

For an Earth-like biosphere, the main detectable atmospheric chemical signatures that in combination could indicate habitability are O_2/O_3 with CH_4/N_2O, and CH_3Cl. Note that a single spectral feature, e.g. O_2, does not constitute a biosignature by itself as the planetary context (like bulk planet, atmospheric composition and planet insolation) must be taken into account to interpret this signature. Detecting high concentrations of a reducing gas concurrently with O_2 or O_3 can be used as a biosignature since reduced gases and oxygen react rapidly with each other. Both being present in significant and therefore detectable amounts in low resolution spectra implies a strong source of both. In the IR, O_3 can be used as a proxy for oxygen at 10^{-2} Present Atmospheric Level of O_2, the depth of the 9.6μm O_3 feature is comparable to the modern atmospheric level (Kasting et al. 1985; Segura et al. 2003). At the same time, because of the 9.6μm O_3 feature's non-linear dependence on the O_2 concentration, observing in the visible at 0.76μm would be a more accurate O_2 level indicator, but requires higher resolution than detecting O_3.

N_2O and CH_3Cl are both primarily produced by life on Earth with no strong abiotic sources. However, their spectral features are likely too small to detect in low resolution with the first generation of missions. While H_2O or CO_2 are not considered biosignatures as both are produced through abiotic processes, they are important indicators of habitability as raw materials and can indicate the level of greenhouse effect on a planet. We refer the reader to other work (e.g. Des Marais et al. 2002; Meadows 2005; Kaltenegger et al. 2010) for a more in depth discussion on habitability and biosignatures. In this section we briefly discuss the most important photochemical reactions involving: H_2O, O_2, O_3, CH_4, N_2O, and CH_3Cl.

Water, H_2O: Water vapor is an important greenhouse gas in Earth's atmosphere. Over 99% of H_2O vapor is currently in the troposphere, where it is an important source of OH via the following set of reactions:

$$\mathrm{O_3} + h\nu \rightarrow \mathrm{O_2} + \mathrm{O(^1D)} \tag{R1}$$

$$\mathrm{H_2O} + \mathrm{O(^1D)} \rightarrow \mathrm{OH} + \mathrm{OH} \tag{R2}$$

In the troposphere, the production of $O(^1D)$ takes place for $3000\ \text{Å} < \lambda < 3200\ \text{Å}$, the lower limit of which is set by the inability of wavelengths, λ shorter than 3000 Å to reach the troposphere due to O_3 shielding. H_2O, while photochemically inert in the troposphere, can be removed by photolysis primarily by wavelengths shortward of 2000 Å in the stratosphere. The photodissociation threshold energy is 2398 Å, but the cross-section of the molecule above 2000 Å is very low. Stratospheric H_2O can be transported from the troposphere or be formed in the stratosphere by CH_4 and OH.

$$\mathrm{CH_4 + OH \rightarrow CH_3 + H_2O} \tag{R3}$$

Oxygen and Ozone, O_2 and O_3: In an atmosphere containing O_2, O_3 concentrations are determined by the absorption of ultraviolet (UV) light shortward of 2400 Å in the stratosphere. O_3 is an oxidizing agent more reactive than O_2, the most stable form of oxygen, due to the third oxygen atom being loosely bound by a single bond. O_3 is also an indirect measure of OH since reactions involving O_3 and H_2O are sources of OH. OH is very reactive and is the main sink for reducing species such as CH_4. O_3 is formed primarily by the Chapman reactions (1930) of the photolysis of O_2 by UV photons (1850 Å $< \lambda <$ 2420 Å) and then the combining of O_2 with O.

$$\mathrm{O_2} + h\nu \rightarrow \mathrm{O + O}\ (\lambda < \ 240\ \mathrm{nm}) \tag{R4}$$

$$\mathrm{O + O_2 + M \rightarrow O_3 + M} \tag{R5}$$

$$\mathrm{O_3} + h\nu \rightarrow \mathrm{O_2 + O}\ (\lambda < \ 320\ \mathrm{nm}) \tag{R6}$$

$$\mathrm{O_3 + O \rightarrow 2\ O_2} \tag{R7}$$

where M is any background molecule such as O_2 or N_2. Reactions [R5] and [R6] are relatively fast compared with [R4] and [R7] which are the limiting reactions in Earth's atmosphere. However, considering the Chapman mechanism alone would overpredict the concentration of O_3 by a factor of two on Earth. Hydrogen oxide (HO_x), nitrogen oxide (NO_x), and chlorine (ClO_x) radicals are the additional sinks controlling the O_3 abundance (Bates & Nicolet 1950; Crutzen 1971; Molina & Rowland 1974, respectively), with NO_x and HO_x being the dominant and second-most dominant sink, respectively.

Methane, CH_4: Since CH_4 is a reducing gas, it reacts with oxidizing species and thus has a short lifetime of around 10^{-12} years in modern Earth's atmosphere (Houghton et al. 2004). In both the troposphere and stratosphere, CH_4 is oxidized by OH, which is the largest sink of the global methane budget. In the stratosphere, CH_4 is also destroyed by UV radiation. Though its photodissociation energy is 2722 Å, its absorption cross-section isn't sufficient for $\lambda > 1500$ Å. CH_4 is produced biotically by methanogens and termites, and abiotically through hydrothermal vent systems. In the modern atmosphere there is a significant anthropogenic source of CH_4 from natural gas, livestock, and rice paddies. CH_4 is 25x more effective as a greenhouse gas than CO_2 in modern Earth's atmosphere (Forster et al. 2007) and may have been much more abundant in the early Earth (see e.g. Pavlov et al. 2003).

Nitrous Oxide, N_2O: Nitrous oxide, N_2O, is a relatively minor constituent of the modern atmosphere at around 320 ppbv, with a pre-industrial concentration of 270 ppbv (Forster et al. 2007). It is important for stratospheric chemistry since around 5% is converted to NO, an important sink of O_3, and 95% produces N_2.

$$\mathrm{H_2O} + \mathrm{O}(^1\mathrm{D}) \rightarrow 2\mathrm{NO} \tag{R8}$$

On current Earth, N_2O is emitted primarily by denitrifying bacteria with anthropogenic sources from fertilizers in agriculture, biomass burning, industry and livestock.

Methyl Chloride, CH_3Cl: CH_3Cl has been proposed as a potential biosignature because its primary sources are marine organisms, reactions of sea foam and light, and biomass burning (Segura et al. 2005). The primary loss of CH_3Cl in Earth's atmosphere is by OH as seen in [R9], but it can also be photolyzed or react with atomic chlorine. Because CH_3Cl is a source of chlorine in the stratosphere, it also plays a role in the removal of O_3 as discussed earlier.

$$CH_3Cl + OH \rightarrow Cl + H_2O \tag{R9}$$

$$CH_3Cl + h\nu \rightarrow CH_3 + Cl \tag{R10}$$

$$CH_3Cl + Cl \rightarrow HCl + Cl \tag{R11}$$

2.2 Model Description

We use EXO-P (Kaltenegger & Sasselov 2010) a coupled one-dimensional radiative-convective atmosphere code developed for rocky exoplanets based on a 1D climate (Kasting & Ackerman 1986; Pavlov et al. 2000; Haqq-Misra et al. 2008), 1D photochemistry (Pavlov & Kasting 2002; Segura et al. 2005, 2007) and 1D radiative transfer model (Traub & Stier 1976; Kaltenegger & Traub 2009) to calculate the model spectrum of an Earth-like exoplanet.

2.2.1 Planetary Atmosphere Model

EXO-P is a model that simulates both the effects of stellar radiation on a planetary environment and the planet's outgoing spectrum. The altitude range extends to 60km with 100 layers. We use a geometrical model in which the average 1D global atmospheric model profile is generated using a plane parallel atmosphere, treating the planet as a Lambertian sphere, and setting the stellar zenith angle to 60 degrees to represent the average incoming stellar flux on the dayside of the planet (see also Schindler & Kasting 2000). The temperature in each layer is calculated from the difference between the incoming and outgoing flux and the heat capacity of the atmosphere in each layer. If the lapse rate of a given layer is larger than the adiabatic lapse rate, it is adjusted to the adiabat until the atmosphere reaches equilibrium. A two-stream approximation (see Toon et al. 1989), which includes multiple scattering by atmospheric gases, is used in the visible/near IR to calculate the shortwave fluxes. Four-term, correlated-k coefficients parameterize the absorption by O_3, H_2O, O_2, and CH_4 in wavelength intervals shown in Fig. 2.1 (Pavlov et al. 2000). In the thermal IR region, a rapid radiative transfer model (RRTM) calculates the longwave fluxes. Clouds are not explicitly calculated. The effects of clouds on the temperature/pressure profile are included by adjusting the surface albedo of the Earth-Sun system to have a surface temperature of 288K (see Kasting et al. 1984; Pavlov et al. 2000; Segura et al. 2003, 2005). The photochemistry code, originally developed by Kasting et al. (1985) solves for 55 chemical species linked by 220 reactions using a reverse-Euler method (see Segura et al. 2010, and references therein).

The radiative transfer model used to compute planetary spectra is based on a model originally developed for trace gas retrieval in Earth's atmospheric spectra (Traub & Stier 1976) and further developed for exoplanet transmission and emergent spectra (Kaltenegger et al. 2007; Kaltenegger & Traub 2009; Kaltenegger 2010; Kaltenegger et al. 2010). In this paper we model Earth's reflected and thermal emission spectra using 21 of the most spectroscopically significant molecules (H_2O, O_3, O_2, CH_4, CO_2, OH, CH_3Cl, NO_2, N_2O, HNO_3, CO, H_2S, SO_2, H_2O_2, NO, ClO, HOCl, HO_2, H_2CO, N_2O5, and HCl).

Using 34 layers the spectrum is calculated at high spectral resolution, with several points per line width, where the line shapes and widths are computed using Doppler and pressure broadening on a line-by-line basis, for each layer in the model atmosphere. The overall high-resolution spectrum is calculated with 0.1 cm^{-1} wavenumber steps. The figures are shown smoothed to a resolving power of 250 in the IR and 800 in the VIS

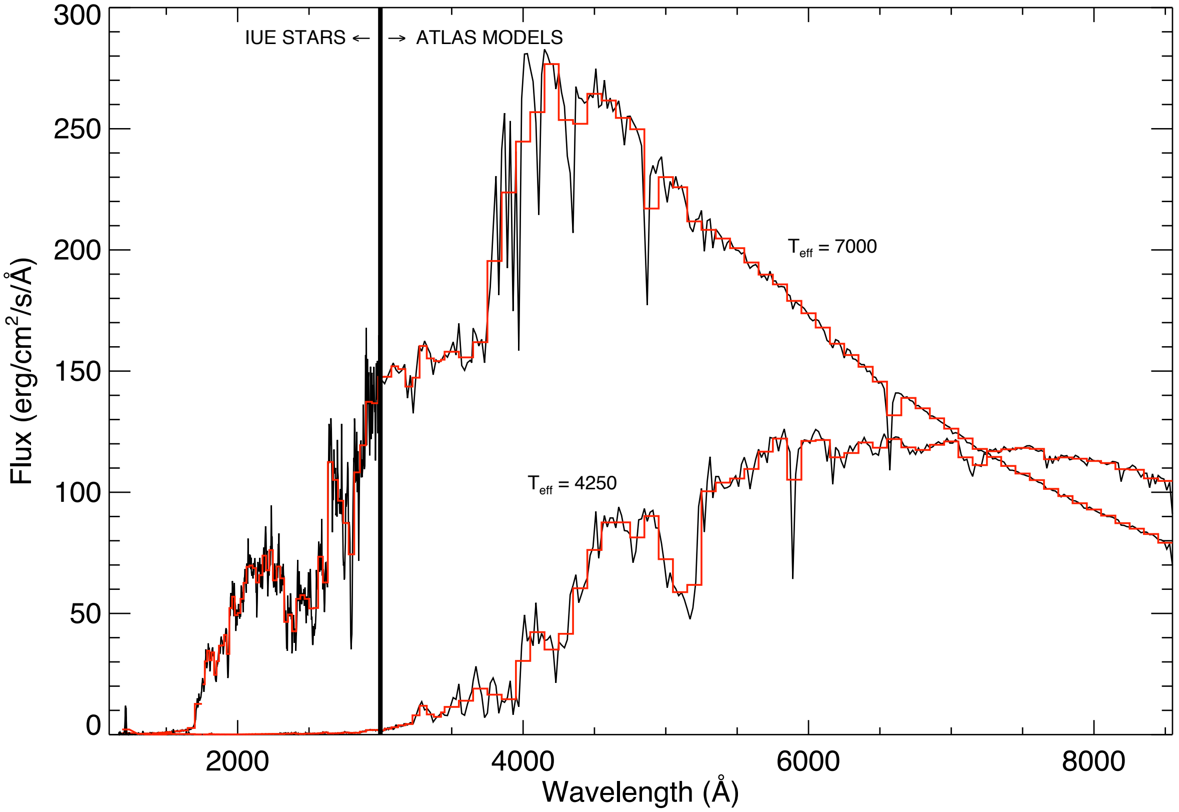

Figure 2.1: F0V and K7V composite input stellar spectrum of IUE observations coadded to (black) ATLAS photospheric models (Kurucz 1979) and (red) binned stellar input. Note: the full input spectrum extends to 45450 Å. Only the hottest and coolest star in our grid are shown here for comparison.

using a triangular smoothing kernel. The spectra may further be binned corresponding to proposed future spectroscopy missions designs to characterize Earth-like planets.

2.2.2 Model Validation with EPOXI

We previously validated EXO-P from the VIS to the infrared using data from ground and space (Kaltenegger et al. 2007). Here we use new data by EPOXI in the visible and near-infrared (Livengood et al. 2011) for further validation (see Fig. 2.2). The data set we use to validate our visible and the near-infrared Earth model spectra is the first EPOXI observation of Earth which was averaged over 24 hours on 03/18/2008 - 03/19/2008 and taken at a phase angle of 57.7°. The uncertainty in the EPOXI calibration is ∼10% (Klaasen et al. 2008). Atmospheric models found the best match to be for a 50% cloud coverage with 1.5km and 8.5km cloud layer respectively (Robinson et al. 2011).

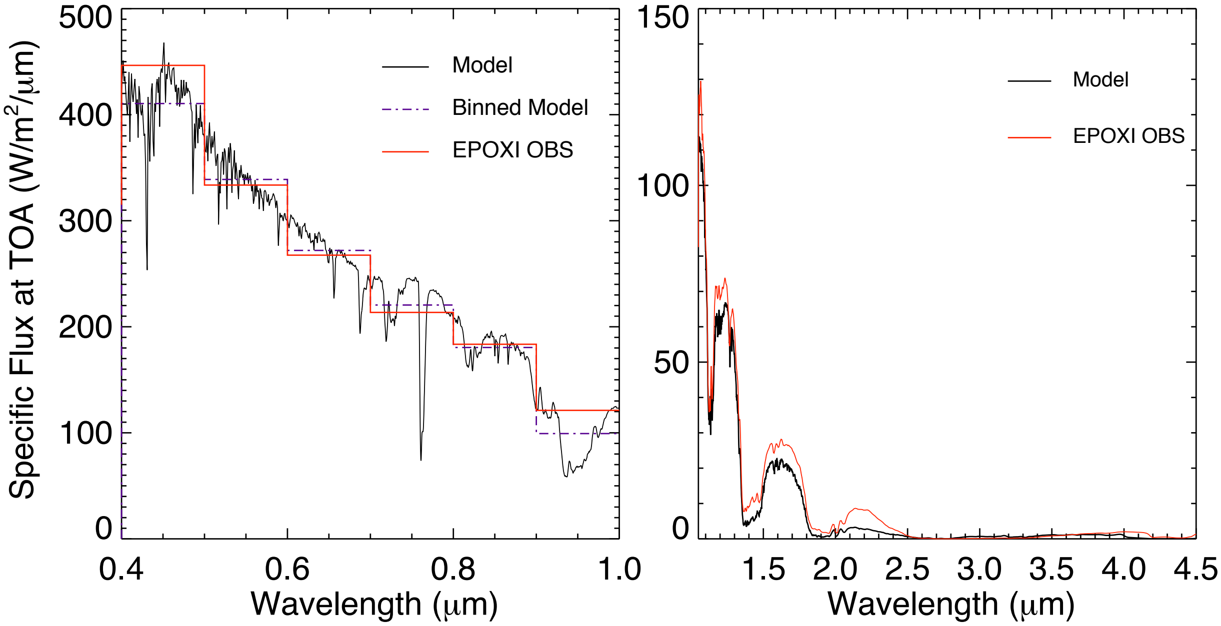

Figure 2.2: Comparison of EPOXI data (red) with the Earth model, top-of-atmosphere spectrum at full phase from EXO-P (black) in the visible (left) and near-infrared (right).

Here we use a 60% global cloud cover spectrum divided between three layers: 40% water clouds at 1km, 40% water clouds at 6km, and 20% ice clouds at 12km (following Kaltenegger et al. 2007) consistent with an averaged Earth profile to compare our model to this 24hr data set, which should introduce slight discrepancies. To correct the brightness values to match to our full-phase model we use a Lambert phase function.

Our model agrees with EPOXI on an absolute scale within 1-3% for the middle photometric points. The largest discrepancies in the visible are at 0.45μm and 0.95μm (with a 8% and 18% error respectively).

2.2.3 Stellar Spectral Grid Model

The stellar spectra grid ranges from 4250K to 7000K in effective temperature increments of 250K. This temperature range effectively probes the F0 to K7 main sequence spectral types. For each model star on our grid we concatenated a solar metallicity, unreddened synthetic ATLAS spectrum, which only considers photospheric emission (Kurucz 1979), with observations from the International Ultraviolet Explorer (IUE) archive. We use IUE measurements to extend ATLAS synthetic spectra, to generate input spectra files from 1150Å to 45,450Å (see Figs. 2.1 and 2.2). We choose main sequence stars in the IUE archive with corresponding temperatures close to the grid temperatures and near solar metallicity, as described below.

The IUE satellite had three main cameras, the longwave (LWP/LWR) cameras (1850Å - 3350Å), and the shortwave (SW) camera (1150Å - 1975Å). When preparing the IUE data (following Segura et al. 2003; Massa & Fitzpatrick 1998, 2000), we used a sigma-weighted average to coadd the multiple SW and LW observations. We used a linear interpolation when there was insufficient high quality measurements to merge the wavelength region from the SW to the LW cameras. IUE measurements were joined to ATLAS model spectra at 3000Å. In a few cases, a shift factor is needed to match the IUE data to the ATLAS model (Segura et al. 2003, see also) but unless stated explicitly no shift factor was used. Effective temperatures and metallicities are taken from NStED (derived from Flower 1996; Valenti & Fischer 2005, , respectively) unless otherwise cited. See Table 2.1 for a summary list of the representative IUE stars chosen.

Table 2.1:: List of representative IUE stars with their measured Teff, the Teff which corresponds to our grid of stars, their metallicity, and their approximate stellar type following Gray (1992).

Star	T_{eff} (K)	T_{eff}(K) Grid	[Fe/H]	Spectral Type Grid
η Lep	7060	7000	-0.13	F0V
σ Boo	6730	6750	-0.43	F2V
π^3 Ori	6450	6500	0.03	F5V
ι Psc	6240	6250	-0.09	F7V
β Com	5960	6000	0.07	F9V/G0V
α Cen A	5770	5750	0.21	G2V
τ Ceti	5500	5500	-0.52	G8V
HD 10780	5260	5250	0.03	K0V
ϵ Eri	5090	5000	-0.03	K2V
ϵ Indi	4730	4750	-0.23	K4V
61 Cyg A	4500	4500	-0.43	K5V
BY Dra	4200	4250	0.00	K7V

HD 40136, η Lep, is at 15.04pc with a T_{eff} = 7060K and [Fe/H] = -0.13 (Cayrel de Strobel et al. 2001), corresponding to an F0V, the hottest model grid star. Two LW and four SW spectra were coadded and merged with a 7000K ATLAS spectrum.

To compare with previous work (Segura et al. 2003; Grenfell et al. 2007; Selsis 2000), we chose HD 128167, σ Boötis, for our model F2V grid star. σ Boötis is an F2V star at 15.47pc with T_{eff} = 6730K and [Fe/H] = -0.43. Two LW and five SW spectra were coadded and merged with a 6750K ATLAS spectrum. A slight downward shift of a factor of 0.88 is necessary to match the IUE data with a ATLAS spectrum (see also Segura et al. 2003).

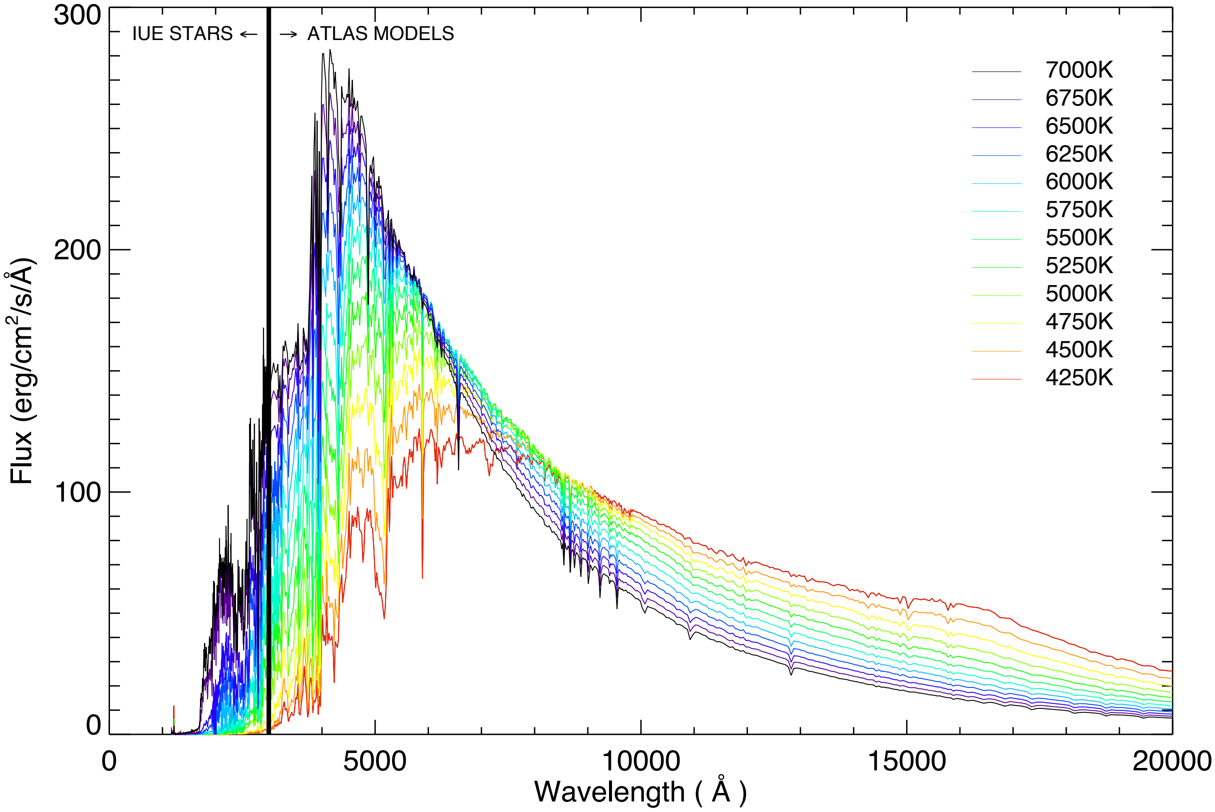

Figure 2.3: Composite stellar input spectra from IUE observations merged to a ATLAS photosphere model at 3000 Å for each grid star. We display up to 20,000 here however the complete input files extend to 45,450 Å.

π^3 Orionis, HD 30652, is at 8.03pc with a $T_{\rm eff}$ = 6450K and [Fe/H] = 0.03, corresponding to an F5V grid star. Two LW and three SW spectra were coadded and merged with a 6500K ATLAS spectrum.

ι Piscium, HD 222368, is at 13.79pc with a $T_{\rm eff}$ = 6240K and [Fe/H]= -0.09, corresponding to an F7V grid star. Two LW and four SW spectra were coadded and merged with a 6250K ATLAS spectrum.

β Com, HD 114710, is at 9.15pc with a $T_{\rm eff}$ = 5960K and [Fe/H]= 0.07, corresponding to an G0V grid star. Only one LW spectrum was correctable with the Massa routines and thus one LW and five SW spectra were coadded and merged with a 6000K ATLAS spectrum.

α Centauri A, HD 128620, is at 1.35 pc with a $T_{\text{eff}} = 5770$K and [Fe/H]= 0.21, corresponding to a G2V grid star. Three LW and 93 SW spectra were coadded and merged with an upward shift of 1.25 to a 5750K ATLAS spectrum.

τ Ceti, HD 10700, is at 3.65pc with $T_{\text{eff}} = 5500$K and [Fe/H]=-0.52, corresponding to a G8V grid star. Two LW and eight SW spectra were coadded and merged with a 5500K ATLAS spectrum.

HD 10780 is at 9.98pc with $T_{\text{eff}} = 5260$K and [Fe/H] = 0.03, corresponding to a K0V grid star. It is a variable of the BY Draconis type. Five LW and four SW spectra were coadded and merged with a 5250K ATLAS spectrum.

ϵ Eridani, HD 22049, is at 3.22pc with $T_{\text{eff}} = 5090$K and [Fe/H] = -0.03, corresponding to a K2V gird star. ϵ Eri was chosen to compare with previous work (Segura et al. 2003; Grenfell et al. 2007; Selsis 2000). ϵ Eri is a young star, only 0.7 Ga (Di Folco et al. 2004), and is thus more active than a typical K-dwarf. Due to its variability and close proximity there are frequent IUE observations. 17 LW and 72 SW IUE spectra were coadded and merged these with a 5000K ATLAS spectrum.

ϵ Indi, HD 209100, is at 3.63 pc with $T_{\text{eff}} = 4730$K and [Fe/H] = -0.23, corresponding to a K4V grid star. Seven LW and 30 SW IUE spectra were coadded and merged with a 4750K ATLAS spectrum.

61 Cyg A, HD 201091, is at 3.48 pc with $T_{\text{eff}} = 4500$K and [Fe/H] = -0.43 (Cayrel de Strobel et al. 2001), corresponding to a K5V grid star. 61 Cyg A is a variable star of

the BY Draconis type. Six LW and twelve SW spectra were coadded and merged with an upward shift of 1.15 to match the 4500K ATLAS spectrum.

BY Dra, HD 234677, is at 16.42pc with a $T_{\rm eff}$ = 4200K (Hartmann et al., 1977) and [Fe/H] = 0 (Cayrel de Strobel et al. 1997), corresponding to a K7V grid star. It is, not surprisingly, a variable of the BY Draconis type. Eight LW and 30 SW spectra were coadded and merged to the 4250K ATLAS spectrum.

All input stellar spectra are shown in Fig. 2.3.

2.2.4 Simulation Set-Up

To examine the effect of the SED of the host star on an Earth-like atmosphere, we build a temperature grid of stellar models ranging from 7000K to 4250K in steps of 250K, corresponding to F type stars to K dwarfs. We simulated an Earth-like planet with the same mass as Earth at the 1AU equivalent orbital distance, where the wavelength integrated stellar flux received on top of the planet's atmosphere is equivalent to 1AU in our solar system, 1370 W/m^{-2}.

The biogenic fluxes were held fixed in the models in accordance with the fluxes that reproduce the modern mixing ratios in the Earth-Sun case (following Segura et al., 2003). We first calculate the surface fluxes for long-lived gases H_2, CH_4, N_2O, CO and CH_3Cl. Simulating the Earth around the Sun with 100 layers yields a $T_{\rm surf}$ = 288K for surface mixing ratios: $cH_2 = 5.5 \times 10^{-7}$, $cCH_4 = 1.6 \times 10^{-6}$, $cCO_2 = 3.5 \times 10^{-4}$, $cN_2O = 3.0 \times 10^{-7}$, $cCO = 9.0 \times 10^{-8}$, and $cCH_3Cl = 5.0 \times 10^{-10}$. The corresponding surface fluxes are -1.9 x 10^{12} g H_2 yr^{-1}, 5.3 x 10^{14} g CH_4 yr^{-1}, 7.9 x 10^{12} g N_2O yr^{-1}, 1.8 x 10^{15} g CO yr^{-1}, and 4.3 x 10^{12} g CH_3Cl yr^{-1}. The best estimate for the modern CH_4 flux is 5.35 x

10^{14} g yr^{-1} (Houghton et al., 2004) and corresponds to the value derived in the model. Fluxes for the other biogenic species are poorly constrained. The N_2 concentration is set by the total surface pressure of 1 bar. To explore the effect of UV and temperature separately, we combine a certain ATLAS model with varying UV files and vise versa.

2.3 Atmospheric Model Results and Discussion

The stellar spectrum has two effects on the atmosphere: first, the UV effect (§2.3.1) that primarily influences photochemistry and second, the temperature effect (§2.3.2) resulting from the difference in absorbed flux as a function of stellar SED. The same planet has a higher Bond albedo around hotter stars with SEDs peaking at shorter λ, where Rayleigh scattering is more efficient, than around cooler stars, assuming the same total stellar flux (Sneep & Ubachs 2005). The overall resulting planetary Bond albedo that includes both atmospheric as well as surface albedo is calculated by the climate/photochemistry model and varies between 0.13 - 0.22 for planets around F0 stars to K7 stars respectively because of the stars' SED. Note that these values are lower than Earth's planetary Bond albedo of 0.31 because the warming effect of clouds is folded into the albedo value in the climate code, decreasing it artificially.

2.3.1 The influence of UV levels on Earth-like atmosphere models (UV effect)

To explore the effects of UV flux alone on the atmospheric abundance of different molecules, we combined specific IUE data files for stars with T_{eff} = 7000K, 6000K and

4500K (representing high, mid and low UV flux) with a fixed ATLAS photospheric models of $T_{\text{eff}} = 6000$K. The temperature/pressure and chemical profiles of this test are shown in panels a) of Figs. 2.4 and 2.5. Hot stars provide high UV flux in the 2000 - 3200 Å range, e.g. a F0V grid star emits 130x more flux in this wavelength range than a K7V grid star (Figs. 2.1 and 2.3).

Table 2.2:: Surface temperature and O_3 column depth for an Earth-like planet model orbiting the grid stars.

T_{eff}(K) Grid	Spectral Type Grid	Surface Temp (K)	Ozone Column Depth (cm^{-2})
7000	F0V	279.9	1.210^{19}
6750	F2V	281.7	1.110^{19}
6500	F5V	283.2	9.610^{18}
6250	F7V	284.6	8.310^{18}
6000	F9V/G0V	286.4	7.310^{18}
SUN	G2V	288.1	5.310^{18}
5750	G2V	287.7	5.110^{18}
5500	G8V	289.1	3.210^{18}
5250	K0V	290.9	4.110^{18}
5000	K2V	291.9	3.310^{18}
4750	K4V	292.8	2.610^{18}
4500	K5V	297.0	2.610^{18}
4250	K7V	300.0	3.510^{18}

The Chapman reactions are driven primarily by photolysis in this wavelength range and the atmosphere models show an according increase in O_3 concentration and subsequent strong temperature inversion for planets orbiting hot grid stars (Table 2.2). The maximum heating in the stratosphere is a few kilometers above the peak of the O_3 concentration where both a high enough concentration of O_3 and a high enough flux of photons is present. O_3 abundance increases OH abundance, the primary sink of CH_4 and

CH_3Cl. Figs. 2.5 and 2.7 shows a corresponding decrease in those molecules for high UV environment. O_3 shields H_2O in the troposphere from UV environments. Stratospheric H_2O is photolyzed by $\lambda < 2000$ Å or reacts with excited oxygen, $O(^1D)$ to produce OH radicals. Accordingly stratospheric H_2O concentration decreases with decreasing UV flux. N_2O decreases with increasing UV flux because of photolysis by $\lambda < 2200$ Å. N_2O is also an indirect sink for stratospheric O_3 when it is converted to NO. Therefore decreasing N_2O increases O_3 abundance. O_2 and CO_2 concentrations remain constant and well mixed for all stellar types.

2.3.2 The influence of stellar T_{eff} on Earth-like atmosphere models (Temperature effect)

To explore the effects of stellar T_{eff} alone on the atmospheric abundance of different molecules, we combined specific photospheric ATLAS spectrum of T_{eff} = 7000K, 6000K and 4500K (representing high, mid and low stellar T_{eff}) with a fixed UV data file of T_{eff} = 6000K. The temperature/pressure and chemical profiles of this test are shown in panels b) of Figs. 2.4 and 2.5. T_{eff} affects H_2O vapor concentrations due to increased evaporation for high planetary surface temperature which is transported to the stratosphere. Fig. 2.4 shows an overall increase in tropopause and stratopause height for low stellar T_{eff} with according hot planetary surface temperatures.

The response of O_3 to stellar T_{eff} is weak due to two opposing effects: high stellar T_{eff} and according low planetary surface and atmospheric temperatures increase O_3 concentration by slowing Chapman reactions that destroy O_3, but also increase NO_x, HO_x, and ClO_x concentrations which are the primary sinks of O_3 (see also Grenfell et al.

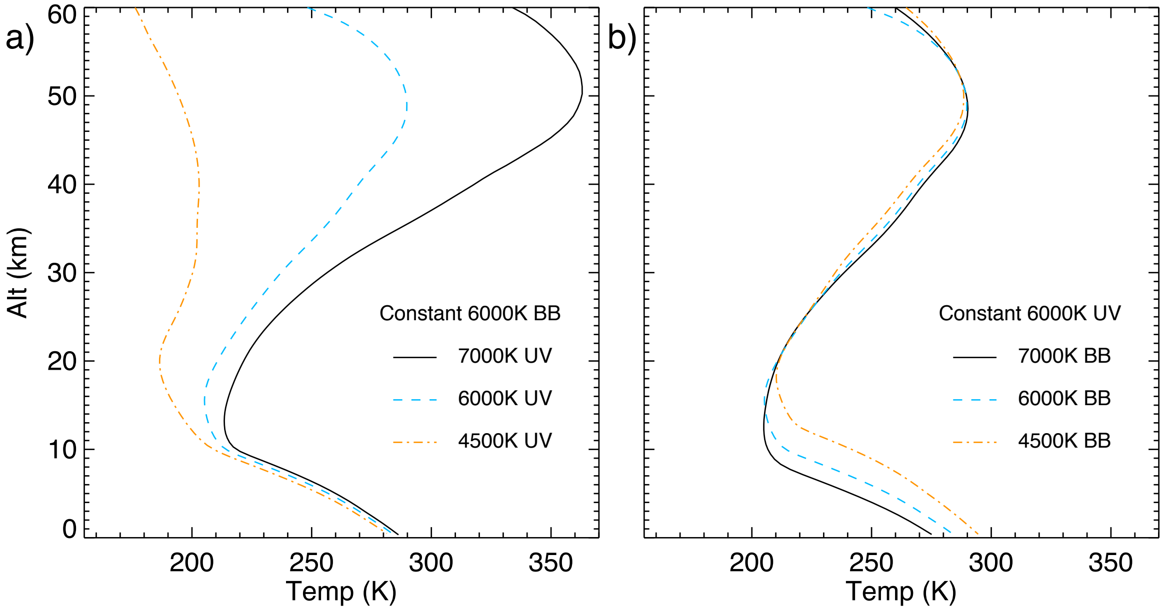

Figure 2.4: Temperature/altitude profiles for several unphysical test where we: a) combine high, mid, and low UV fluxes (IUE observations for stars with $T_{\rm eff}$ = 7000K, 6000K, and 4500K, respectively) with a fixed ATLAS photosphere model for $T_{\rm eff}$ = 6000K to show the "UV effect," and b) combine high, mid, and low stellar photosphere models (ATLAS models for $T_{\rm eff}$ = 7000K, 6000K, and 4500K, respectively) with a fixed UV flux for $T_{\rm eff}$ = 6000K to show the "Temperature effect."

2007).

Both CH_4 and CH_3Cl show only a weak temperature dependence. The rate of the primary reactions of CH_4 and CH_3Cl with OH slows with decreasing temperature, causing an increase in CH_4 and CH_3Cl for lower planetary surface temperatures. N_2O displays a similar weak temperature effect. All of our simulations used a fixed mixing ratio of 355ppm for CO_2 and 21% O_2. Since both O_2 and CO_2 are well mixed in the atmosphere, their vertical mixing ratio profiles are not shown.

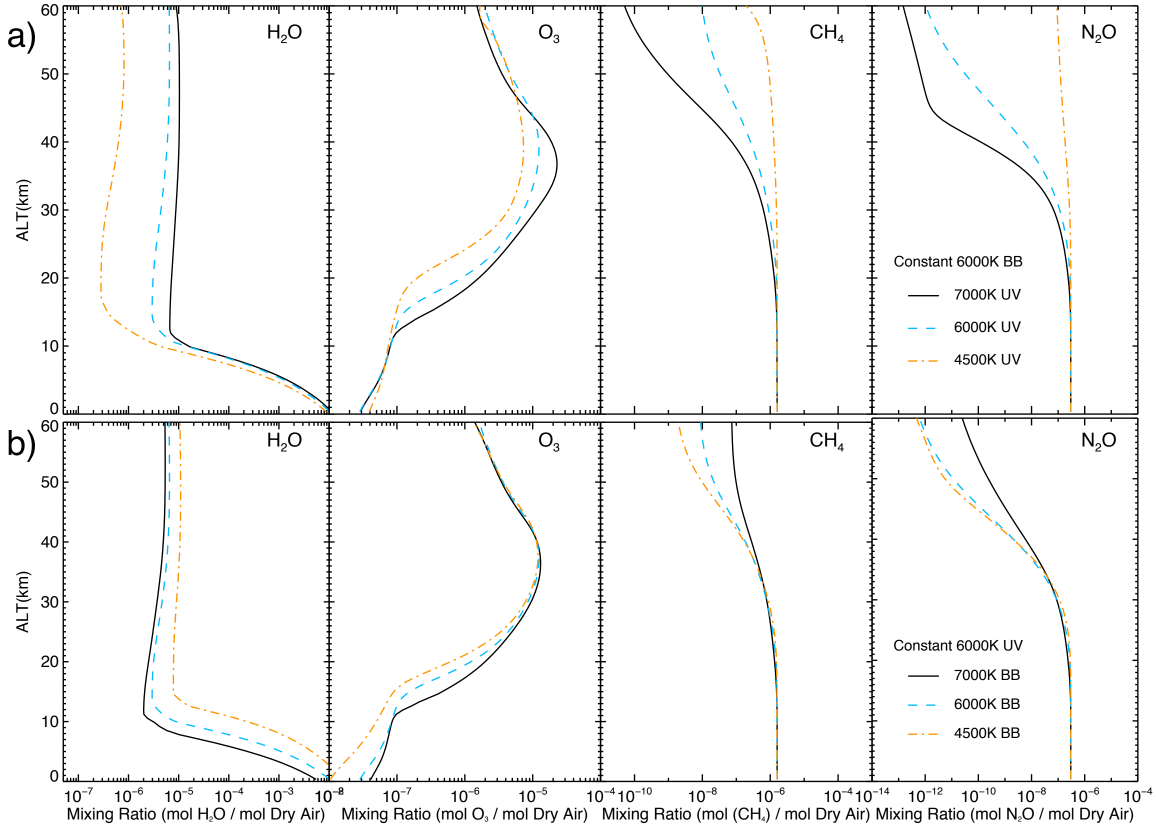

Figure 2.5: Chemical mixing ratio profiles for H_2O, O_3, CH_4, and N_2O from several unphysical test where we: a) combine high, mid, and low UV fluxes (IUE observations for stars with $T_{\mathrm{eff}} = 7000$K, 6000K, and 4500K, respectively) with a fixed ATLAS photosphere model for $T_{\mathrm{eff}} = 6000$K to show the "UV effect", and b) combine high, mid, and low stellar photosphere models (ATLAS models for $T_{\mathrm{eff}} = 7000$K, 6000K, and 4500K, respectively) with a fixed UV flux for Teff = 6000K to show the "Temperature effect."

2.3.3 The influence of stellar SED on Earth-like atmosphere models

Figs. 2.6 and 2.7 show the combined temperature and UV effect on Earth-like atmospheres. The surface temperature of an Earth-like planet increases with decreasing stellar effective temperature due to decreasing reflected stellar radiation and increasing IR absorption by H_2O and CO_2 (see Table 2.2 and Fig. 2.6). The late K-dwarf stars show in addition a near isothermal stratosphere.

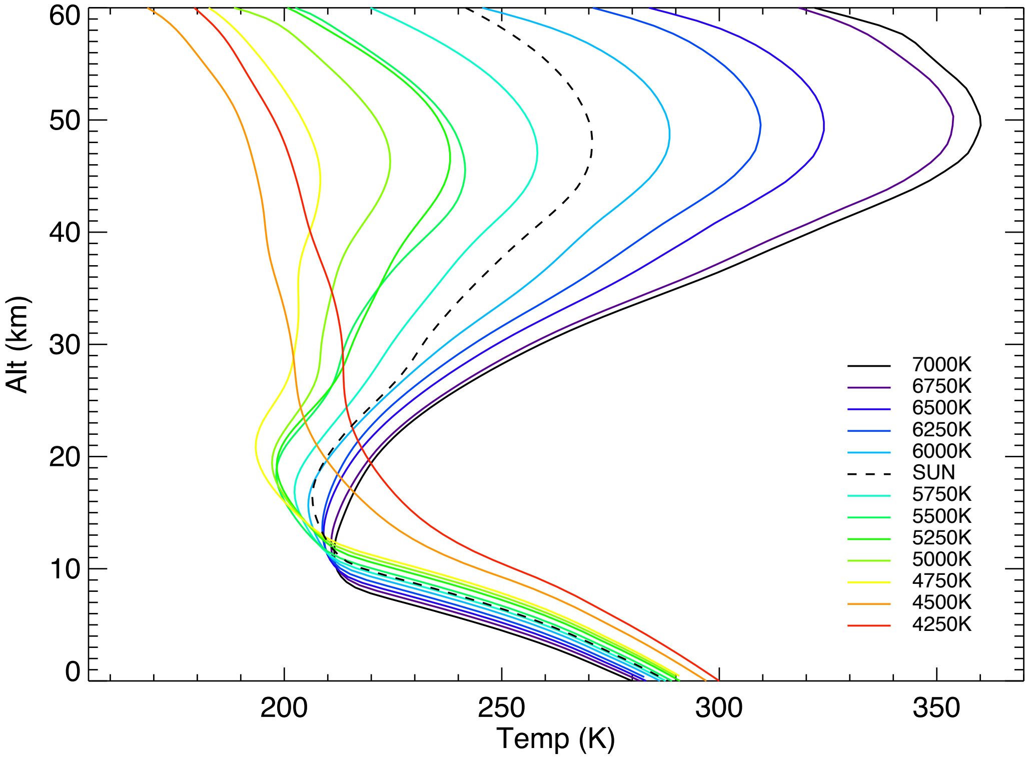

Figure 2.6: Planetary temperature/altitude profiles for different stellar types showing the combined temperature and UV effect.

Fig. 2.7 shows the corresponding atmospheric mixing ratios versus height for the grid stars. The top height considered in our atmosphere models is 60 km for a Sun-like star, which corresponds to 10^{-4} bar (following Segura et al. 2003). For hotter stars the stratosphere is warmer increasing the pressure at 60 km to 4.0 x 10^{-4} bars while for cooler stars the pressure at 60 km decreases to 3.0 x 10^{-5} bars.

Earth-like atmosphere models around hot grid stars show high O_3 concentration

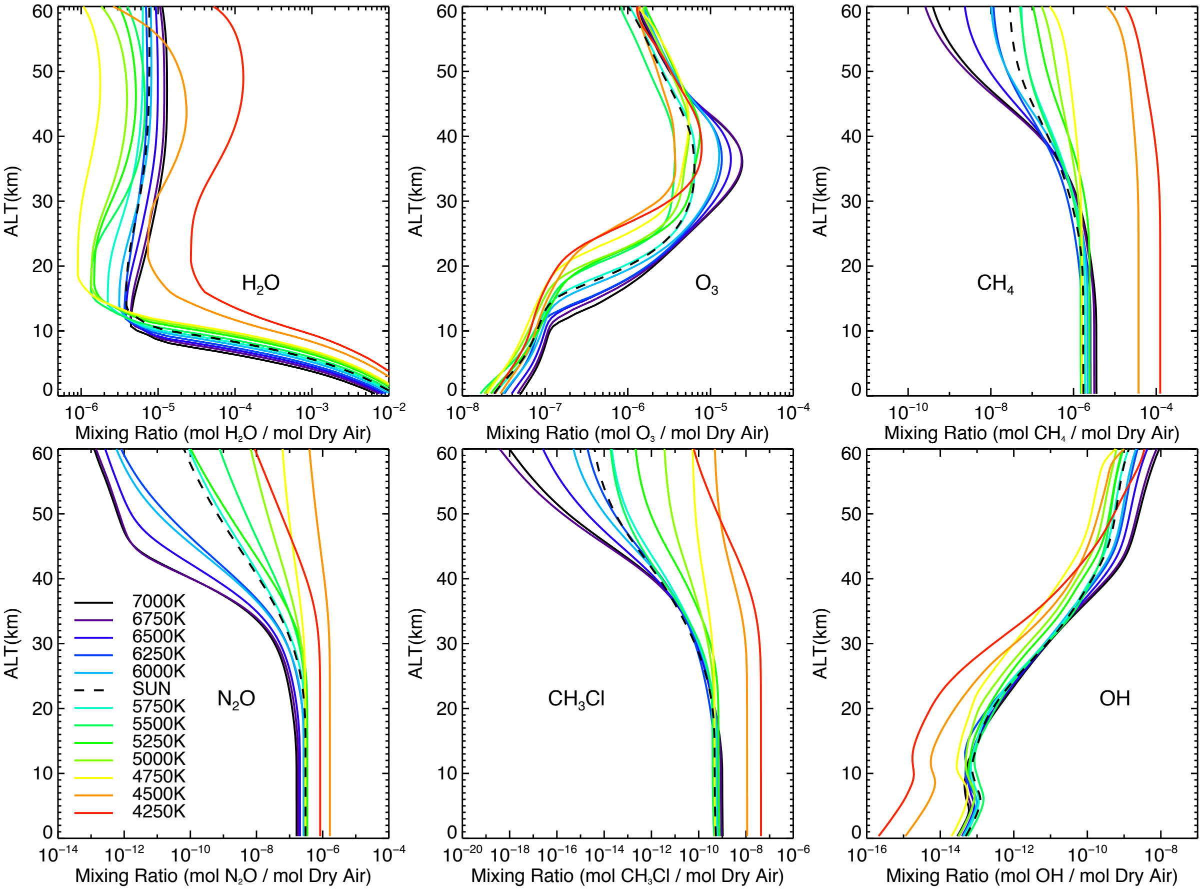

Figure 2.7: Photochemical model results for the mixing ratios of the major molecules H_2O, O_3, CH_4, N_2O, CH_3Cl, and OH for each stellar spectral type in our grid of stars showing the combined temperature and UV effect.

(see Table 2.2) and therefore strong temperature inversions due to the increased stellar UV flux (Fig. 2.6). Cooler stars often have stronger emission lines and higher activity. Accordingly the coldest two grid stars in our sample ($T_{\rm eff}$ = 4250K and 4500K) show a large O_3 abundance due to high stellar Ly-α flux. In fact, the UV output of the coldest grid star, $T_{\rm eff}$ = 4250K is almost 2x the UV flux of the second coldest grid star, $T_{\rm eff}$ = 4500K, also due to its younger age. Thus, there is more O_3 produced for the coldest star. However, in the 2000 - 3000 Å wavelength region these cold grid stars emit low UV flux and therefore produce near isothermal stratospheres (see also M-dwarf models in Segura et al. 2005). The detailed effect of Ly-α flux on the planet's atmosphere, will be modeled in a future paper.

Earth-like atmosphere models around hot grid stars also show high OH concentrations due to a higher availability of high energy photons, as well as O_3 and H_2O molecules (Fig. 2.7). Cold grid stars ($T_{\rm eff}$ = 4250K) show higher OH concentration in the stratosphere than expected from an extrapolation from the other grid stars due to the increased O_3 and H_2O concentrations at those altitudes.

CH_4 abundance increases with decreasing stellar temperature, dominated by the effects of decreasing stellar UV. Stratospheric CH_4 decreases in atmosphere models around hot grid stars since both OH concentration and UV flux increase with stellar $T_{\rm eff}$ and act as sinks of CH_4.

H_2O abundance in the troposphere is dominated by the surface temperature of the planet. Earth-like planet atmosphere models around cool grid stars, generate warmer planetary surface temperatures, and therefore high amounts of tropospheric H_2O. High UV flux generally decreases H_2O concentration in the stratosphere through photolysis but increased O_3 concentrations provides shielding from the photolysis of H_2O. Also cold grid stars ($T_{\rm eff}$ = 4250K and 4500K) show increased stratosphere H_2O concentration through increased vertical transport in the nearly isothermal stratospheres as well as production by stratospheric CH_4 (see e.g. Segura et al. 2005, for similar behavior in planets around M-dwarfs). In particular, the atmosphere models for a planet around $T_{\rm eff}$ = 4250K grid star has a high OH concentration in the stratosphere due to increased O_3 and H_2O at those altitudes.

N_2O is primarily produced by denitrifying bacteria and has increased linearly due to agriculture since the preindustrial era at a rate of around 0.26% yr^{-1} (Forster et al. 2007). Up to about 20km, there is no significant difference between stellar types in N_2O concentration. Above $\sim$ 20km, Fig. 2.7 shows a decrease in N_2O concentration for atmosphere models around hot compared to cool grid stars since UV is the primary sink of N_2O in the stratosphere. Below 20km N_2O is shielded from photolysis by the O_3 layer. Note that the general trend for increasing N_2O for colder grid stars reverses for our coldest grid star. This is due to the increased UV flux which destroys N_2O and an increase in O_3 which causes an increase in $O(^1D)$, another strong sink for N_2O.

CH_3Cl concentration decreases with increased stellar UV flux since OH which act as sink for CH_3Cl.

2.4 Results: Spectra of Earth-like Planets Orbiting F0V to K7V Grid Stars

We include both a clear sky as well as a 60% global cloud cover spectrum which has cloud layers analogous to Earth (40% 1km, 40% 6km and 20% 12km following Kaltenegger et al. (2007)) in Figs. 2.8-2.11 to show the importance of clouds on the reflected and emission planet spectra. We present the spectra as specific flux at the top of the atmosphere of Earth-like planets. In the VIS, the depth of the absorption features is primarily sensitive to the abundance of the species, while in the IR, both the abundance and the temperature difference between the emitting/absorbing layer and the continuum influences the depth of features.

We use a Lambert sphere as an approximation for the disk integrated planet in our model. The surface of our model planet corresponds to Earth's current surface of 70% ocean, 2% coast, and 28% land. The land surface consists of 30% grass, 30% trees, 9% granite, 9% basalt, 15% snow, and 7% sand. Surface reflectivities are taken from the USGS Digital Spectral Library[1] and the ASTER Spectral Library[2] (following Kaltenegger et al. 2007). Note the vegetation red edge feature at 0.76μm is only detectable in the clear sky model spectra in low resolution, see Fig. 2.8 (see e.g Kaltenegger et al. 2007; Seager et al. 2005; Pallé et al. 2008). No noise has been added to these model spectra to provide input models for a wide variety of instrument simulators for both secondary eclipse and direct detection simulations.

We assume full phase (secondary eclipse) for all spectra presented to show the maximum flux that can be observed. Note that we use an Earth-size planet to determine the specific flux and planet-to-star contrast ratio. A Super-Earth with up to twice Earth's radius will provide 4 times more flux and a better contrast ratio than shown in Figs. 2.8 to 2.14.

2.4.1 Earth-like Visible/Near-infrared Spectra (0.4μm - 4μm)

Fig. 2.8 shows emergent spectra from 0.4 to 2μm of Earth-like planets for both a clear-sky and Earth-analogue cloud cover for the grid stars (F0V-K7V). The high resolution spectra have been smoothed to a resolving power of 800 using a triangular smoothing kernel. Figs. 2.8 and 2.9 show that clouds increase the reflectivity of an

---

[1] http://speclab.cr.usgs.gov/spectral-lib.html

[2] http://speclib.jpl.nasa.gov

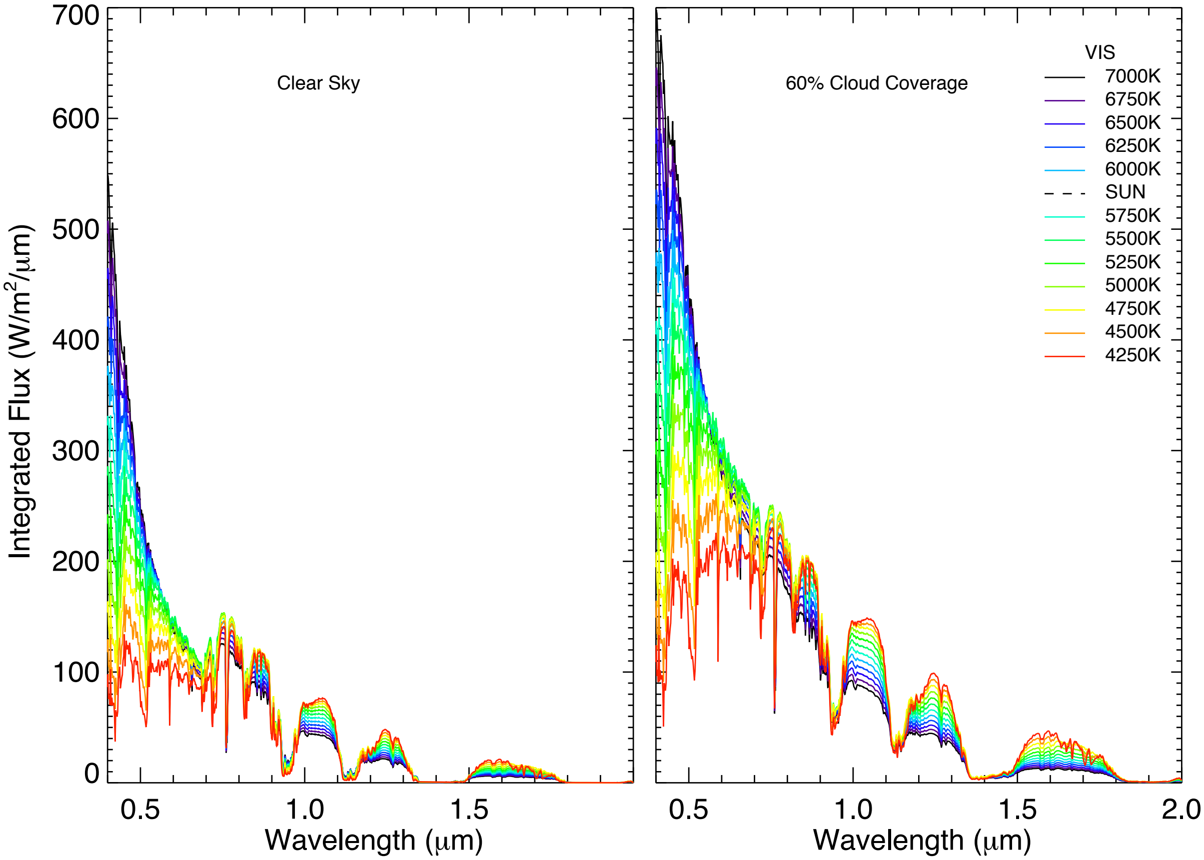

Figure 2.8: Smoothed, disk-integrated VIS/NIR spectra at the top of the atmosphere (TOA) for an Earth-like planet around FGK stars for both a clear sky (left) and 60% cloud coverage (right) model (region 2-4μm has low integrated flux levels and therefore is not shown here).

Earth-like planet in the VIS to NIR substantially and therefore overall increase the equivalent width of all observable feature, even though they block access to some of the lower atmosphere.

Fig. 2.9 shows individual features for the strongest atmospheric features from 0.4 to 4μm for Earth-like planets orbiting the grid stars: O_3 at 0.6μm (the Chappuis band), O_2 and 0.76μm, H_2O at 0.95μm, and CH_4 at 1.7μm. The left panel of each row shows the relative flux as planet-to-star contrast ratio, the middle and right panel show the specific, top-of-atmosphere flux for a clear and 60% cloud cover, respectively. From the planet-to-star contrast ratios in Figs. 2.9, 2.11 and 2.13 the photometric precision required to detect these features for Earth-like planets can be calculated. Note that any shallow spectral features like the visible O_3 feature would require a very high SNR to be detected.

The 0.6μm shallow O_3 spectral feature depth increases with $T_{\rm eff}$ of the star host since O_3 concentration increases with UV levels but is difficult to distinguish from Rayleigh scattering. The relative depth of the O_2 feature at 0.76μm is constant but the flux decreases for cool grid stars due to the decrease in absolute stellar flux received and reflected by the planet at short wavelengths. The depth of the H_2O absorption feature at 0.9μm (shown) 0.8, 1.1 and 1.4 μm increase for planets orbiting cool grid stars due to their increased H_2O abundance. The depth of the CH_4 absorption feature at 1.7μm increases with decreasing stellar $T_{\rm eff}$ due to the increase of CH_4 abundance.

From 2 to 4 μm there are CH_4 features at 2.3μm and 3.3μm, a CO_2 feature at 2.7μm, and H_2O absorption at 2.7μm and 3.7μm. However, due to the low emergent flux in this region, these features are not shown individually.

2.4.2 Earth-like Infrared Spectra, IR (4μm - 20μm)

Fig. 2.10 shows emergent spectra from 4 to 20μm of Earth-like planets for both a clear sky and Earth-analogue cloud cover for the grid stars (F0V-K7V). The high resolution spectra have been smoothed to a resolving power of 250 using a triangular smoothing kernel. Clouds decrease the overall emitted flux of an Earth-like planet in the IR.

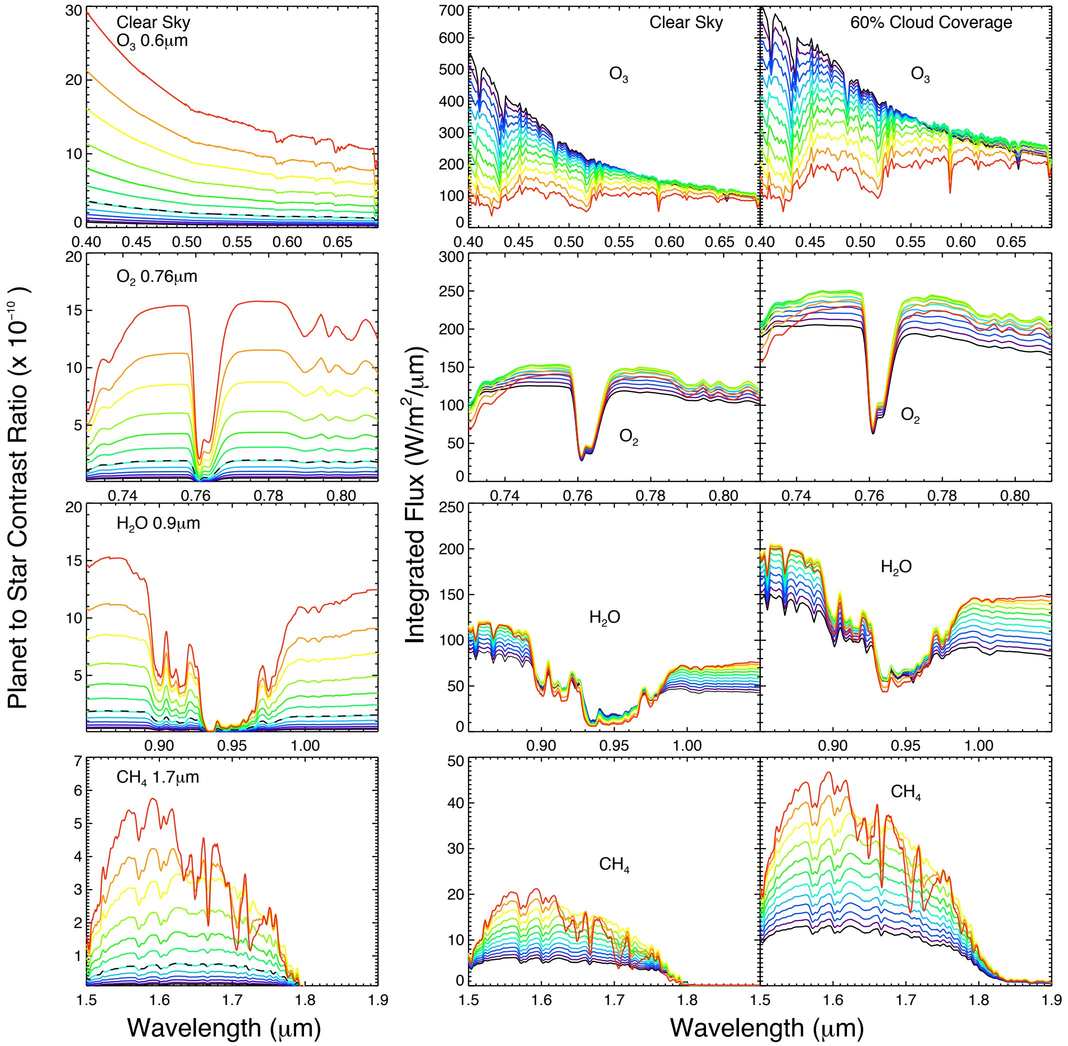

Figure 2.9: Individual features of O_3 at 0.6μm, O_2 and 0.76μm, H_2O at 0.95μm, and CH_4 at 1.7μm for F0V – K7V grid stars (left) planet-to-star contrast ratio and absolute flux levels (middle) for a clear sky and (right) 60% cloud coverage model. Note the different y-axes. Legend and color coding are the same in Figs. 2.6 to 2.8.

Fig. 2.11 shows individual features for the strongest atmospheric features from 4 to 20μm for Earth-like planets orbiting the grid stars: O_3 at 9.6μm, CO_2 at 15μm, H_2O at 6.3μm and CH_4 at 7.7μm for a cloud free and Earth-analogue cloud coverage model. The left panel of each row shows the relative flux as planet-to-star contrast ratio, the

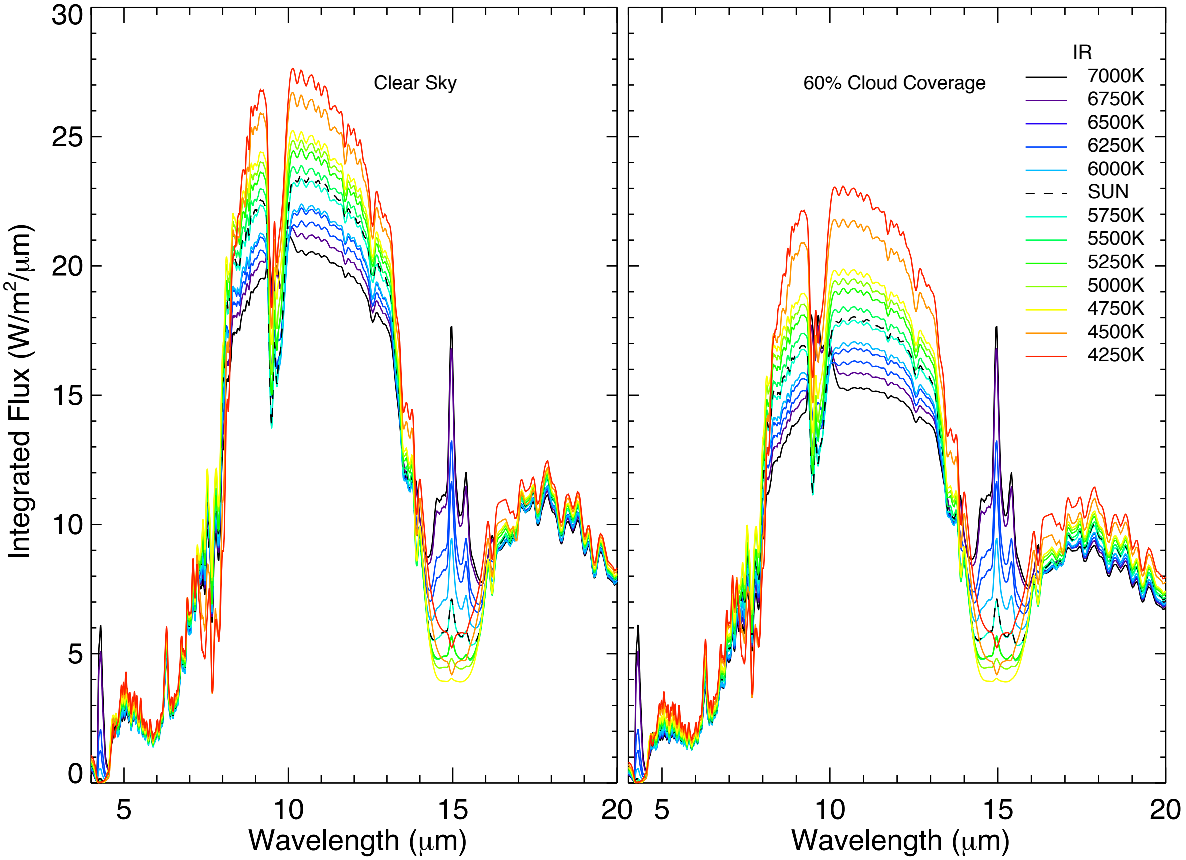

Figure 2.10: Smoothed, disk-integrated IR spectra at the top of the atmosphere (TOA) for Earth-like planets around F0V to K7V grid stars for both a clear sky (left) and 60% cloud coverage (right) model.

middle and right panel show the specific, top-of-atmosphere flux for a clear and 60% cloud coverage case, respectively.

In the clear sky model, the depth of the O_3 feature at 9.6μm decreases for planet models orbiting hot grid stars, despite increasing O_3 abundance, due to lower contrast between the continuum and absorption layer temperature. For Earth-analogue cloud cover, however, O_3 is seen in emission for $T_{\rm eff} > 6500$K due to the lower continuum temperature.

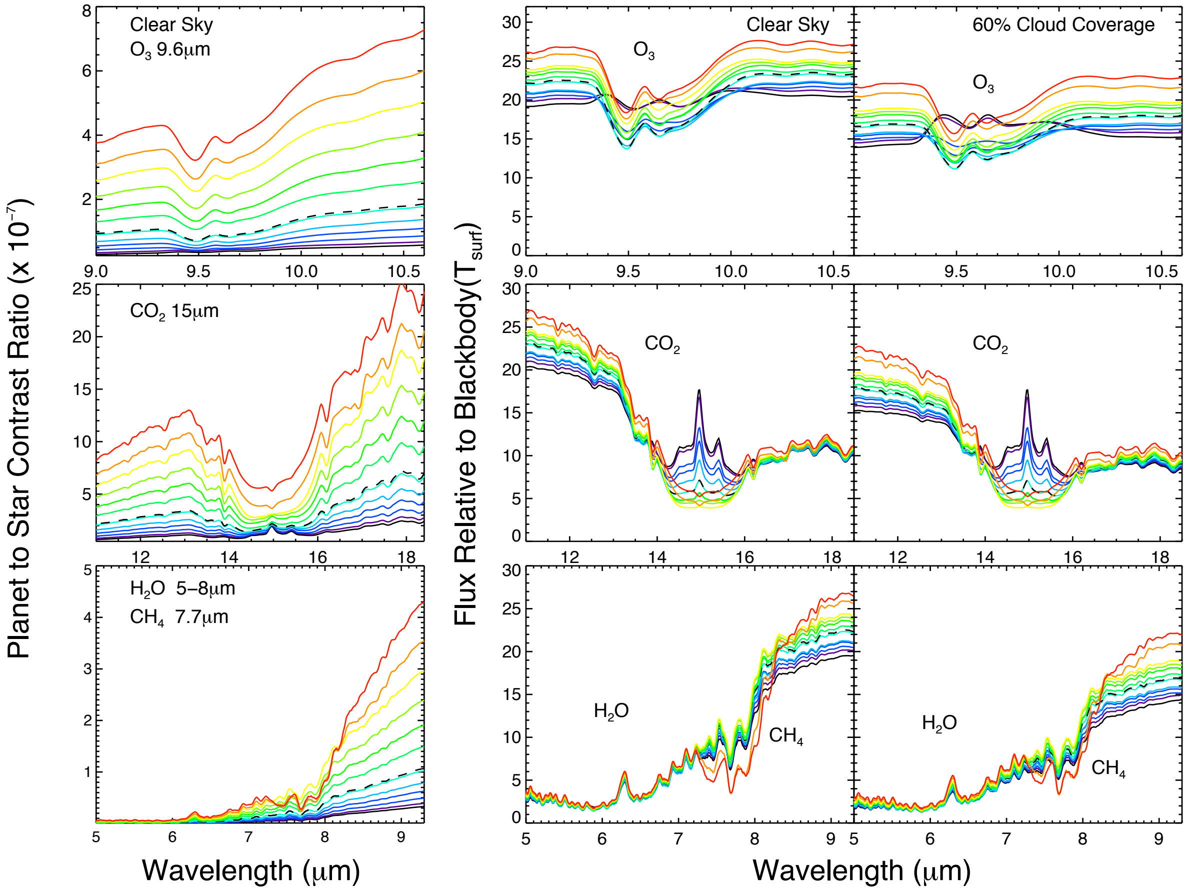

Figure 2.11: Individual features of O_3 at 9.6μm, CO_2 and 15μm, H_2O at 5-8μm, and CH_4 at 7.7μm for F0V – K7V grid stars (left) planet-to-star contrast ratio and absolute flux levels (middle) for a clear sky and (right) 60% cloud coverage model. Legend and color coding are the same in Figs. 2.6 to 2.8.

Due to the hot stratosphere for all grid stars with $T_{\text{eff}} > 6000$K, the CO_2 absorption feature at 15μm has a prominent central emission peak. Clouds reduce the continuum level and the depth of the observable CO_2 feature.

The CH_4 feature at 7.7μm is prominent in the planetary spectra around cool grid stars due to high CH_4 abundance in low UV environments. The CH_4 feature is also partially obscured by the wings of the H_2O feature at 5-8μm. The depth of the H_2O

features at 5-8μm and 18+μm do not change significantly even though H_2O abundance increases for cool grid stars. Clouds reduce the continuum level and the depth of the observable H_2O features.

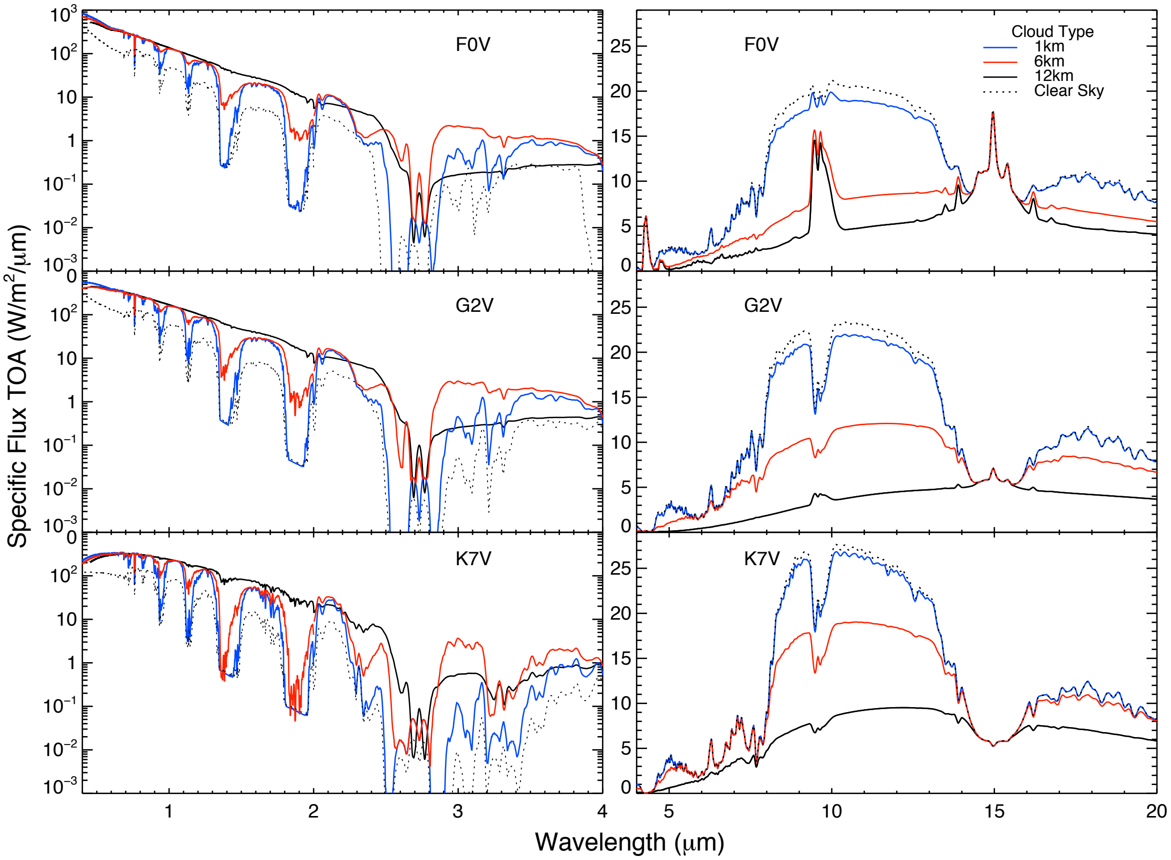

Figure 2.12: Spectra of Earth-like planets for 100% cloud coverage at 3 cloud heights (1km, 6km and 12km, blue, red and black line, respectively) as well as clear sky spectrum (dashed line) from 0.4 to 20 μm, orbiting a $T_{\text{eff}} = 7000$K (top) $T_{\text{eff}} = 5750$K (middle), and $T_{\text{eff}} = 4250$K (bottom) grid star for comparison.

Fig. 2.12 shows planet-to-star contrast ratio for Earth-analog cloud cover of an Earth-like planet from which the photometric precision required can be calculated. The planet-to-star contrast ratio is between 10^{-8} to 10^{-11} in the VIS/NIR and between about

10^{-6} and 10^{-10} in the IR for the grid stars. For the whole wavelength range, the contrast ratio improves for cool grid stars.

2.4.3 The effect of clouds on an Earth-like planet spectra from 0.4 - 20μm

Fig. 2.13 shows Earth-like planet spectra for 100% cloud cover at 1km, 6km and 12km from 0.4 to 20μm for three sample grid stars with $T_{\rm eff}$ = 7000K (top), 5750K (middle), and 4250K (bottom). The clear sky spectrum is shown as dashed line for comparison. Clouds increase the reflectivity of an Earth-like planet in the VIS to NIR substantially and therefore overall increase the equivalent width of all observable features, even though they block access to some of the lower atmosphere. Clouds decrease the overall emitted flux of an Earth-like planet in the IR slightly because they radiate at lower temperatures and therefore overall decrease the equivalent width of all observable absorption features, even though they can increase the relative depth of a spectral feature due to lowering the continuum temperature of the planet.

Fig. 2.14 shows the individual chemical absorption features as discussed in §2.4.1 and §2.4.2 on a relative scale for H_2O, CO_2, O_2, O_3, CH_4, N_2O and CH_3Cl from 0.4μm to 20μm to complement the spectra shown in Figs. 2.8-2.11, that focus on the remote detectability of individual features for future space missions.

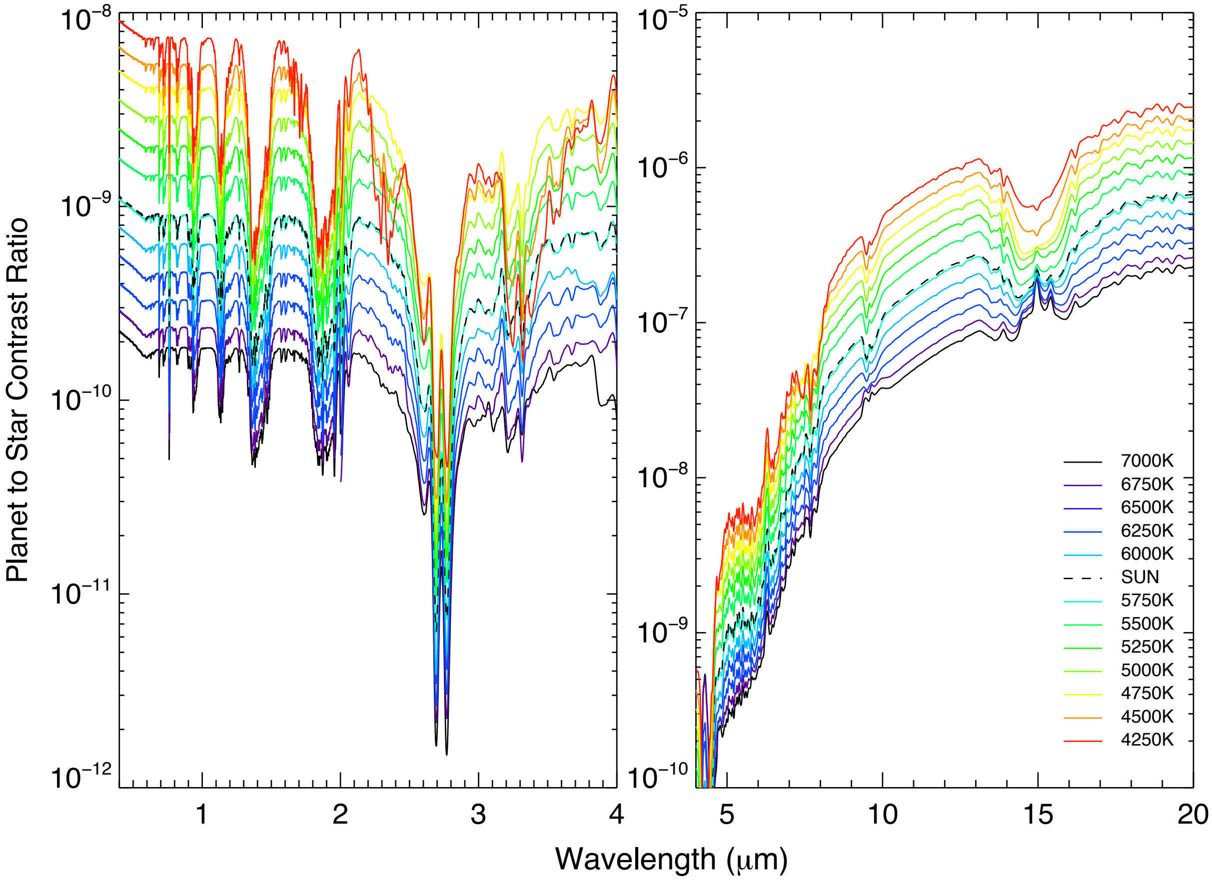

Figure 2.13: Contrast Ratio of Earth-like planets for Earth-analogue cloud coverage.

2.5 Discussion

When choosing IUE stars to for our stellar spectral grid, we avoided stars of unusual variability, but did not exclude stars that had representative variability of its stellar class. Several of our representative K stars are variables of the BY Draconis type which is a common variable in this stellar type. We preferentially choose stars with near solar metallicity when possible; however, the IUE database does not provide candidate stars at each temperature of solar metalliticy. Several stars have lower than solar metallicity. We compared a subsolar stellar metallicity with a solar metallicity spectra model and

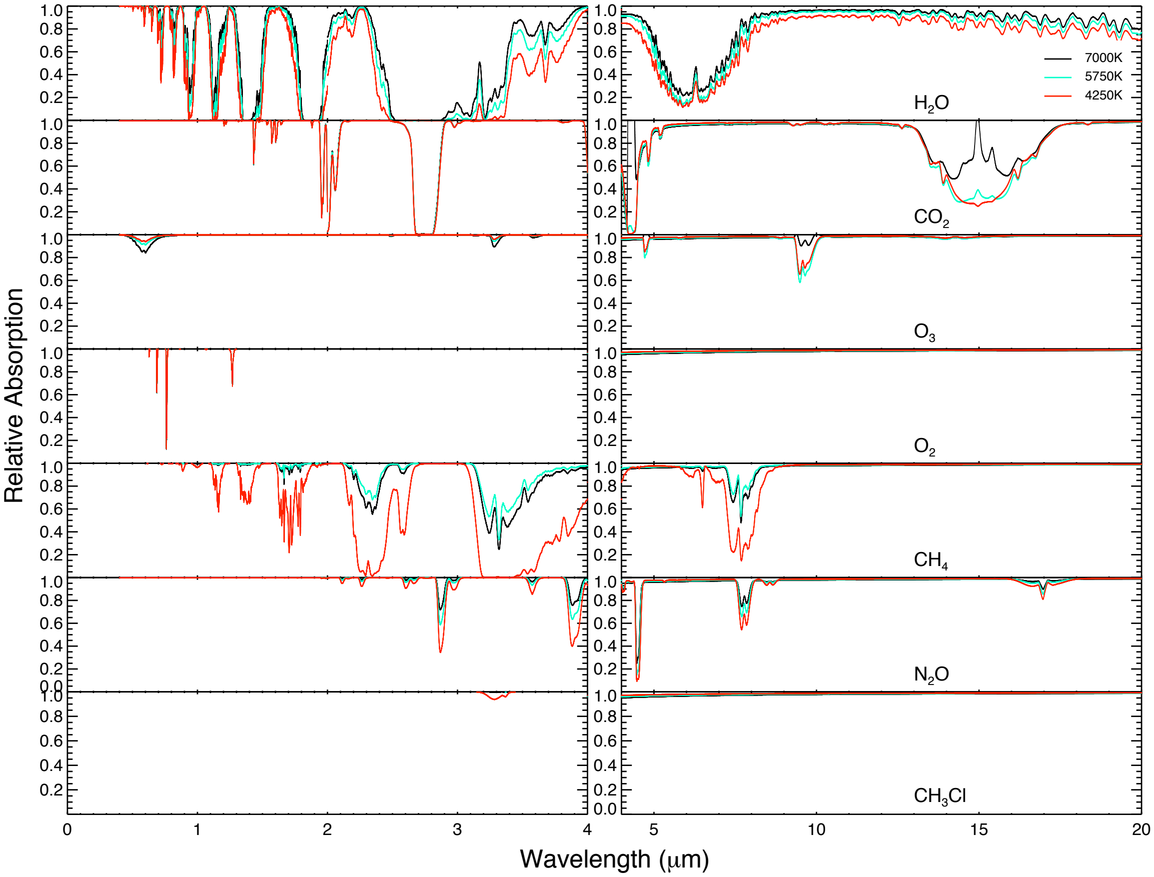

Figure 2.14: Relative absorption of individual chemical species H_2O, CO_2, O_2, O_3, CH_4, N_2O and CH_3Cl for three sample grid stars with $T_{\rm eff}$ = 7000K, 5750K, and 4250K.

found that the difference does not impact our results.

Observability of Biosignatures: Detecting the combination of O_2 or O_3 and CH_4 for emergent spectra and secondary eclipse measurements requires observations in the IR or in the VIS/NIR up to 3μm to include the 2.4μm CH_4 feature in that spectral range. The strength of the absorption features depend on the stellar effective temperature of the host star and vary significantly between stellar types. In the IR, CH_4 at 7.7μm is more detectable at low resolution for cool grid stars than hot grid stars. The 9.6μm O_3 feature is deepest for mid to cool stars and becomes less detectable for hotter stars.

However around our hottest grid stars, the 9.6μm O_3 feature becomes an apparent emission feature for cloudy atmospheres. The narrow O_2 feature in the VIS at 0.72μm is of comparable strength for all grid stars. H_2O has strong features for all grid stars over the whole wavelength range.

N_2O and CH_3Cl have features from the NIR to IR (see Fig. 2.14) but in modern Earth concentrations do not have a strong enough feature to be detected with low resolution. For the clear sky models, the vegetation red edge is detectable due to the order of magnitude increased reflectance from 0.7μm to 0.75μm for all grid stars. Clouds obscure that feature (see Fig. 2.8).

For detecting an oxidizing gas in combination with a reducing gas in Earth-like planet atmosphere models, the coolest grid stars in our sample are the best targets. In this paper we have not modeled planets orbiting stars cooler than 4000K to provide a consistent set of planetary models. As discussed in Segura et al. 2005, cool host stars with low UV flux, provide an environment that leads to run-away CH_4 accumulation in the atmosphere and therefore the model for Earth-like planets around M-dwarfs often use abiotic CH_4 levels, not consistent with Earth-analogue models used in this study. We will explore this effect in a future work.

No noise has been added to these model spectra to provide input models for a wide variety of instrument simulators for both secondary eclipse and direct detection simulations. Different instrument simulators for JWST (see e.g. Deming et al. 2009; Kaltenegger & Traub 2009) explore the capability of JWST's MIRI and NIRspec Instrument to characterize extrasolar planets down to Earth-like planets, with interesting results for planets around close-by as well as luminous host stars. Several new results are forthcoming by several groups that will provide realistic instrument parameters that can be used to determine detectability of these absorption features. Furture ground and space based telescopes are being designed to characterize exoplanets down to Earth-like planets and will provide interesting opportunities to observe atmospheric features, especially for Super-Earths, with radii up to 2 time Earth's radius and therefore 4 times the flux and planet-to-star contrast ratio levels quoted for Earth-size planets shown in Figs. 2.8-2.13.

In addition to the size of the planet, future observations will occur at different positions throughout the planet's orbit. The maximum observable planetary flux in the visible scales with the illuminated fraction of the planet, that is "visible" to the observer. In the IR the maximum flux remains constant throughout the planet's orbit, assuming a similar temperature on the day and night side. In Fig. 2.15 we show the absolute specific flux levels at full phase, gibbous phase, and quadrature scaled with a Lambert phase function (phase angles of 0°, 45°, and 90°, respectively) for 60% cloud coverage Earth-like planets orbiting three grid stars with $T_{\text{eff}} = 7000$K, 5750K and 4250K to show the effect of orbital position (see also Robinson et al., 2011). We scaled our full-phase simulations to other phases using a Lambert phase function. For quadrature, representing an average viewing geometry, the contrast ratios presented in Fig. 2.13 will be a factor of 2 lower in the visible. Assuming the planet has efficient heat transport from the day to night side, the specific flux levels and contrast ratios in the IR will be unchanged.

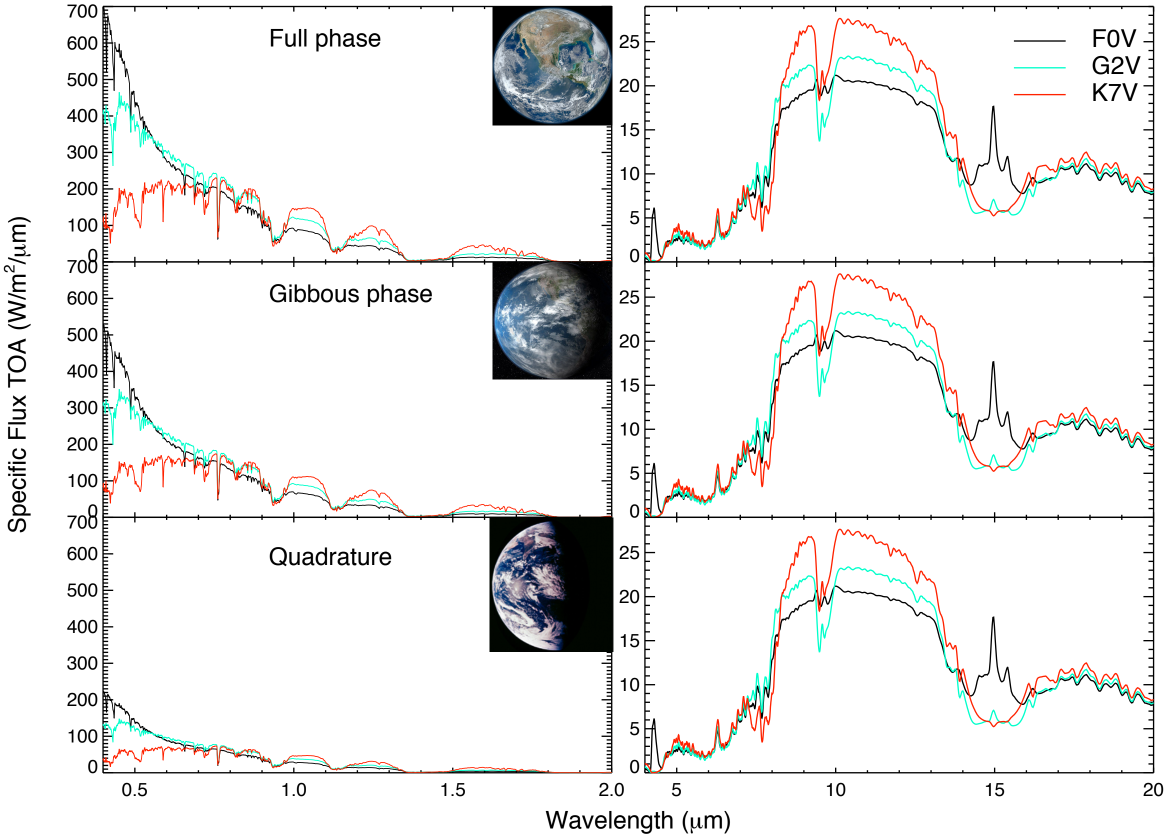

Figure 2.15: Absolute specific flux values for clear-sky Earth-like planets around three different grid stars with $T_{\rm eff}$ = 7000K, 5750K, and 4250K in the visible and IR for 3 phases: full phase, gibbous phase, and quadrature with corresponding phase angles of 0°, 45°, and 90°, respectively.

2.6 Conclusions

We calculated the spectra for terrestrial atmosphere models receiving the same incoming flux as Earth when orbiting a grid of host stars with $T_{\rm eff}$ = 4250K to $T_{\rm eff}$ = 7000K in 250K increments, comprehensively covering the full FGK stellar range. We discuss the spectral features for clear and cloudy atmosphere models and compare the effect of the stars SED and UV flux on both the atmospheric composition as well as the detectable atmospheric features in §2.3 and §2.4.

Increasing UV environments (generally coupled with increasing stellar T_{eff} for main sequence stars) result in: increasing concentration of O_3 from photolysis, increasing stratospheric H_2O from O_3 shielding, increasing OH based on increased O_3 and H_2O concentrations, and decreasing CH_4, CH_3Cl, and N_2O from photolysis and reactions with OH. Increasing stellar temperatures and corresponding decreasing planetary surface temperatures result in: decreasing tropospheric H_2O due to decreased temperatures, decreasing stratospheric H_2O from transport, and decreasing reaction rates of OH with CH_4, N_2O and CH_3Cl. The overall effect as the stellar effective temperature of the main sequence grid stars increases, is an increase in O_3 and OH concentration, a decrease in tropospheric H_2O (but an increase stratospheric H_2O), and a decrease in stratospheric CH_4, N_2O, CH_3Cl.

In the infrared, the temperature contrast between the surface and the continuum layer is strongly impacts the depth of spectral features. While O_3 increases for hotter main sequence stars the strength of the 9.6μm band decreases due to the decrease temperature difference between the continuum and the emitting layer. For hot stars, with $T_{\text{eff}} > 6750$K the O_3 feature appears as emission due to the contrast to the continuum.

Our results provides a grid of atmospheric compositions as well as model spectra from the VIS to the IR for JWST and other future direct detection mission design concepts. The model spectra in this paper are available at www.cfa.harvard.edu/ srugheimer/FGKspectra/.

Acknowledgments

L.K. acknowledge support from DFG funding ENP Ka 3142/1-1 and NAI. This research has made use of the NASA/IPAC/NExScI Star and Exoplanet Database, which is operated by the Jet Propulsion Laboratory, California Institute of Technology, under contract with the National Aeronautics and Space Administration.

The UV data presented in this paper were obtained from the Multimission Archive at the Space Telescope Science Institute (MAST). STScI is operated by the Association of Universities for Research in Astronomy, Inc., under NASA contract NAS5-26555. Support for MAST for non-HST data is provided by the NASA Office of Space Science via grant NAG5-7584 and by other grants and contracts.

Chapter 3

The Effect of UV Radiation on the Spectral Fingerprints of Earth-like Planets orbiting M dwarfs

This thesis chapter has recently been submitted as

S. Rugheimer, L. Kaltenegger, A. Segura, J. Linsky, and S. Mohanty. Submitted to
The Astrophysical Journal on 18 August 2014

Abstract

We model the atmospheres and spectra of Earth-like planets orbiting the entire grid of M dwarfs for active and inactive stellar models with effective temperatures ranging from $T_{\text{eff}} = 2300\text{K}$ to $T_{\text{eff}} = 3800\text{K}$ as well as for six observed MUSCLES M dwarfs with

UV radiation data. We set the Earth-like planets at the 1AU equivalent distance and show spectra from the VIS to IR (0.4μm - 20μm) to compare detectability of features in different wavelength ranges with JWST and other future ground- and spaced-based missions to characterize exo-Earths. We focus on the effect of UV activity levels on detectable atmospheric features that indicate habitability on Earth, namely: H_2O, O_3, CH_4, N_2O and CH_3Cl.

To observe signatures of life - O_2/O_3 in combination with reducing species like CH_4, we find that early and active M dwarfs are the best targets of the M star grid for future telescopes. The O_2 spectral feature at 0.76μm is increasingly difficult to detect in reflected light of later M dwarfs due to low stellar flux in that wavelength region. N_2O, another biosignature detectable in the IR, builds up to observable concentrations in our planetary models around M dwarfs with low UV flux. CH_3Cl could become detectable, depending on the depth of the overlapping N_2O feature.

We present a spectral database of Earth-like planets around cool stars for directly imaged planets as a framework for interpreting future lightcurves, direct imaging, and secondary eclipse measurements of the atmospheres of terrestrial planets in the habitable zone (HZ) to design and assess future telescope capabilities.

3.1 Introduction

About 2000 extrasolar planets have been found to date with thousands more awaiting confirmation from space and ground-based searches. Several of these planets have been found in or near the circumstellar Habitable Zone (see e.g. Quintana et al. 2014; Borucki et al. 2013; Kaltenegger et al. 2013; Batalha et al. 2013; Borucki et al. 2011; Kaltenegger & Sasselov 2011; Udry et al. 2007) with masses and radii consistent with rocky planet models. Future mission concepts to characterize Earth-like planets are designed to take spectra of extrasolar planets with the ultimate goal of remotely detecting atmospheric signatures (e.g. Beichman et al. 1999, 2006; Cash 2006; Traub et al. 2006; Kaltenegger et al. 2006). Several proposed missions are designed to characterize nearby Super-Earth and Earth-like planets using emergent visible and infrared spectra. For transiting terrestrial planets, the James Web Space Telescope (JWST, see Gardner et al. 2006; Deming et al. 2009; Kaltenegger & Traub 2009) as well as future ground and space based telescopes (Snellen et al. 2013; Rodler & López-Morales 2014) will search for biosignatures in a rocky planet's atmosphere. NASA's explorer mission, TESS, is designed to search the whole sky for potentially habitable planets around the closest and brightest stars to Earth (Ricker et al. 2014) for eventual follow-up with JWST and other large ground-based observatories such as the E-ELT or GMT.

In our solar neighborhood, 75% of stars are M dwarfs. The abundance of M dwarfs as well as the contrast ratio and transit probability favor the detection of planets in the Habitable Zone of M dwarfs. Therefore, it is likely that the first habitable planet suitable for follow-up observations will be found orbiting a nearby M dwarf (Dressing & Charbonneau 2013). The M spectral class is very diverse, spanning nearly three orders of magnitude in luminosity and an order of magnitude in mass.

The UV environment of a host star dominates the photochemistry and therefore the resulting atmospheric constituents including biosignatures for terrestrial planets (see e.g. Domagal-Goldman et al. 2014; Tian et al. 2014; Grenfell et al. 2014; Rugheimer et al. 2013; Hu et al. 2012; Segura et al. 2005). To date, few observations exist in the UV region for M dwarfs. Previously, only UV spectra of very active flare stars, such as AD Leo, were available from the IUE satellite, primarily during flares and for a few quiescent phases. The MUSCLES program observed chromospheric emission from six weakly active M dwarfs with HST (France et al. 2013). Note that Ly-α is by far the strongest line in the UV for M dwarfs. Since the core of the intrinsic stellar Ly-α emission is absorbed by neutral hydrogen in the interstellar medium, one must reconstruct the line to compensate for this absorption to get accurate flux levels (see e.g. Wood et al. 2005; Linsky et al. 2013).

Several groups have explored the effect of a different stellar spectral type on the atmospheric composition of Earth-like planets by primarily considering one star, AD Leo, as a template for the diverse range of M dwarfs, and by using the extreme limit of inactivity, photosphere only, PHOENIX models (Grenfell et al. 2014; Kitzmann et al. 2011a,b; Wordsworth et al. 2011; Segura et al. 2005). In this paper we expand on this work by establishing planetary atmosphere models for the full M dwarf main sequence, using a stellar temperature grid from 3800K to 2400K including recent HST observations of 6 M dwarfs to explore the effect of different spectral energy distributions on terrestrial atmosphere models and on detectable atmospheric signatures, including biosignatures. Atmospheric biosignatures are remotely detectable chemical species in the atmosphere that are byproducts of life processes. Recent research shows possible false positives may occur under certain geological settings (Domagal-Goldman et al. 2014; Tian et al. 2014; Wordsworth & Pierrehumbert 2014).

We create a grid of M dwarf input spectra, that can be used to probe the entire range of UV flux levels. To showcase the whole range, we simulate model planets around host stars at the two extreme limits of activity: active and inactive stellar models. We compare these models to the six observed M dwarfs with recent UV observations (France et al. 2013).

We explore the influence of stellar UV flux on the atmospheric structure, chemical abundance, and spectral features for Earth-like planets including the observability of biosignatures in the VIS to IR. We focus our analysis on spectral biosignatures for a temperate rocky planet like Earth: O_3, O_2, CH_4, N_2O and CH_3Cl; and those that indicate habitability: H_2O and CO_2 (Des Marais et al. 2002; Sagan et al. 1993; Lovelock 1975).

In §3.2, we describe our model, and §3.3 presents the influence of stellar types on the abundance of atmospheric chemical species. In §3.4, we examine the remote observability of such spectral features, and in §3.5 and §3.6, we summarize the results and discussing their implications.

3.2 Model Description

3.2.1 Stellar M Dwarf Spectral Grid Model

M dwarfs span nearly three orders of magnitude in luminosity and remain active for much longer timescales than earlier stellar types. As main sequence stars age, their UV flux levels decrease even as their bolometric luminosity increases. Understanding the UV flux incident on a planetary atmosphere is critical to understanding and interpreting future observations of atmospheric constituents, including biosignatures.

Current stellar models are unable to model the UV region from M dwarfs self-consistently due to three main reasons. First, complex magnetic fields responsible for heating the chromosphere are thought to drive much of the UV activity and have thus far been ignored in stellar models. Second, the models are missing opacities in the UV, and third, the models are semi-empirical with no energy conservation to balance magnetic heating with radiative losses. These problems are being addressed by current work and models will be available in the future to test against M dwarf UV observations

We generate stellar input models for the entire M dwarf spectral class (M0 to M9) to explore the boundaries of the UV environment of an exoplanet orbiting a main sequence star. We create two sets of models based on the extreme limits of stellar activity. For the purposes of this paper, "active" stellar models are constructed to represent the most active M dwarf measurements and "inactive" semi-empirical models without chromospheres are constructed to represent the lowest theoretical UV flux field. We compare these limiting-case models to six well-observed M dwarfs which show significant chromospheric flux (see Fig. 3.1) despite being traditionally classified as quiescent stars due to the presence of H_α in absorption (France et al. 2013). A few M dwarfs observed with GALEX in the NUV (1750Å– 2750Å) show near photospheric continuum level fluxes (as computed with PHOENIX models) and can be classified as inactive even though the exact UV flux level has not been measured yet. For example, Gl 445 and Gl 682 have roughly 90% of the observed near ultraviolet (NUV) flux density is predicted by PHOENIX model photospheres (Shkolnik & Barman 2014). More observations are needed to determine the ultimate lower limit of UV flux emitted by old and/or late M dwarfs. To compare our calculations for inactive star models to published work, we use theoretical photosphere PHOENIX models as a lower bound (Allard 2014).

The chromospheric far-ultraviolet (FUV) flux from M, L and T dwarfs (i.e., very low

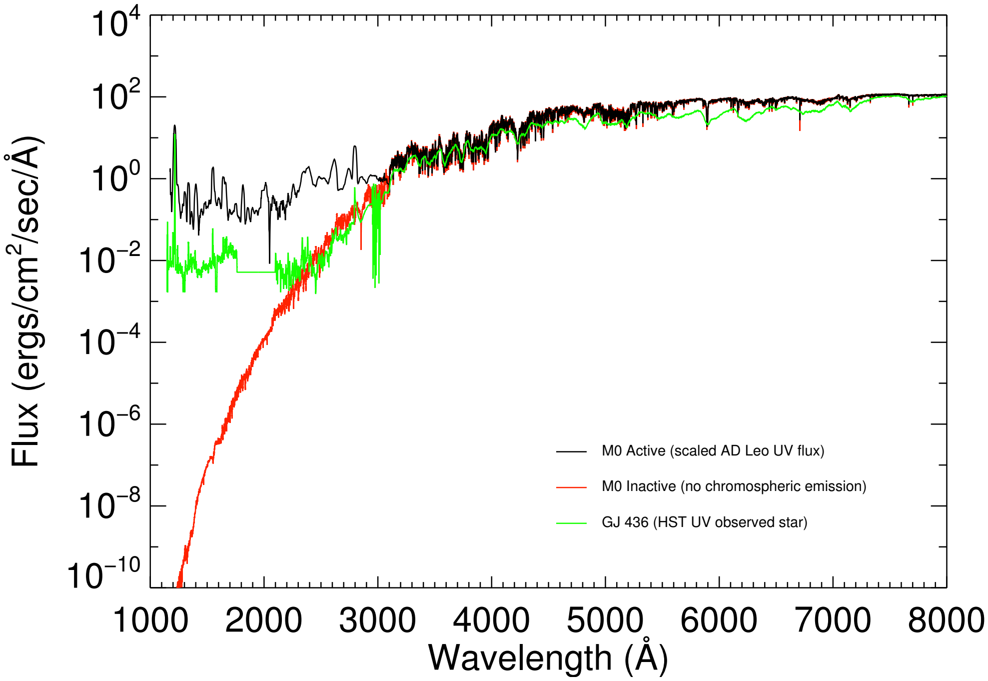

Figure 3.1: Stellar input spectra at the top of the atmosphere (TOA) of Earth-like planet at the 1AU equivalent of an M0 "active" star with UV flux scaled from AD Leo (black), "inactive" PHOENIX model of M0, and HST UV observations plus photosphere model for GJ436 (green).

mass stars and brown dwarfs), while crucial for determining the potential habitability of any planets around them, is very poorly characterized through direct observations. Given their common chromospheric origin, H_α, Ly-α, Ca II H and K, and Mg II H and K emission lines have all been us ed as proxies for FUV activity. However, many of these lines are inaccessible to M dwarfs because they are at shorter wavelengths where these stars are intrinsically less luminous. For M dwarfs, H_α emission in particular has been studied extensively and to date has the most robust dataset for each M dwarf spectral type compared with the other lines considered above (West et al. 2004, 2011). In addition, Jones & West (2014) shows H_α fluxes correlate with NUV fluxes from

GALEX. Therefore, we use H_α to estimate the FUV emission for our active stellar grid by scaling the known FUV and H_α emission from the active M3.5 star AD Leo (see Eq. 3.1 and Fig. 3.2). Very active, early M dwarfs (M0-M5) are known to saturate in the H_α emission around $\log(L_{H_\alpha}/L_{bol}) = -3.75$ (Hawley et al. 1996; Reiners & Basri 2008; West et al. 2004).

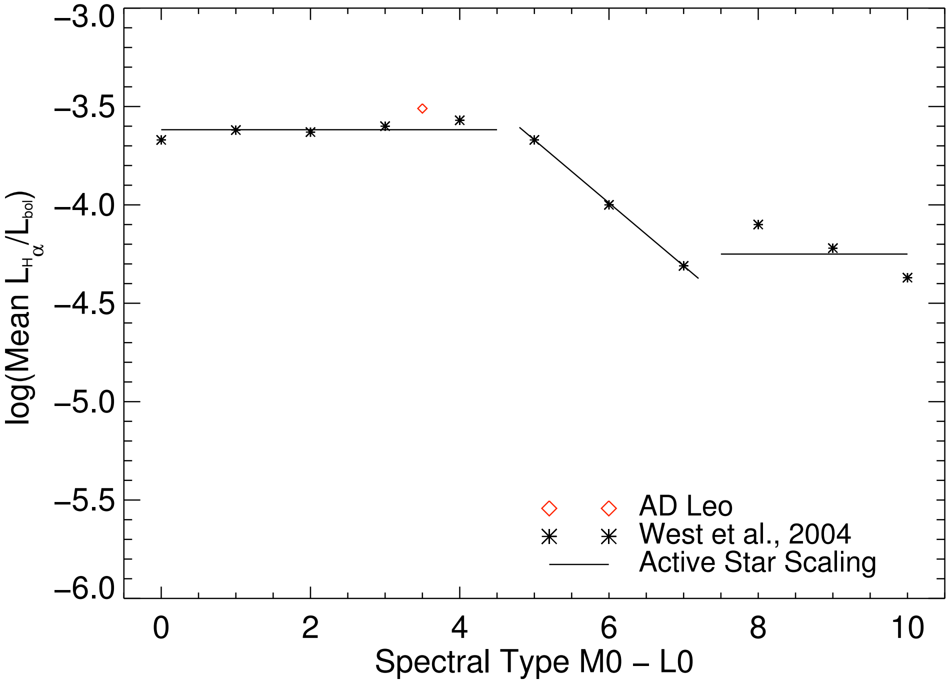

Figure 3.2: Scaling used for active stellar models (black line) over plotted on West et al. (2004) measurements of log(mean L_{H_α}/L_{bol}) (black asterisks).

West et al. (2004) tabulates the log(mean L_{H_α}/L_{bol}) versus spectral type from M0-L0 from observations of 1910 active M dwarfs. We parameterize the data from West et al. (2004) to derive a relationship of UV to mean H_α emission for each spectral sub type in the M dwarf class (See Fig. 3.2 and Eq 3.1).

$$\begin{aligned}\log(L_{H_\alpha *}/L_{bol*}) &= -3.62 \text{ for M0 - M4}\\ \log(L_{H_\alpha *}/L_{bol*}) &= -0.32\times(M)-2.07 \text{ where M} = 5,6,7 \text{ for M5, M6, M7} \qquad (3.1)\\ \log(L_{H_\alpha *}/L_{bol*}) &= -4.25 \text{ for M8 - M9}\end{aligned}$$

We use the H_α/UV scaling of AD Leo, which has both a well characterized UV spectrum and H_α emission measurement as a calibration data point to set the scale. AD Leo, an M3.5eV star, has $\log(L_{H_\alpha}/L_{bol})$ = -3.51 (Walkowicz & Hawley 2009) and has been well observed in the UV (see Segura et al. (2005) for AD Leo IUE spectrum and Linsky et al. (2013) for reconstructed Ly-α flux). The M dwarf active spectrum is then given by:

$$F_{FUV*} = F_{FUV\ AD\ Leo}\times(\frac{T_{\text{eff }*}}{T_{\text{eff AD Leo}}})^4\times\frac{\log(L_{H_\alpha *}/L_{bol*})}{\log(L_{H_\alpha ADLeo}/L_{bolADLeo})} \qquad (3.2)$$

Our stellar temperature grid (Fig. 3.3) covers the full M dwarf spectral range with the stellar parameters for active and inactive models given in Table 3.1. For the active star models, we scale the UV flux in the wavelength range 1000 - 3000Å from AD Leo's observed UV spectrum to the other spectral types according to Eq. 3.2. For each active model star on our grid we concatenated a solar metallicity, unreddened synthetic PHOENIX spectrum, which only considers photospheric emission (Allard 2014), from 3000 - 45,450Å to the scaled observations from the International Ultraviolet Explorer (IUE) archive for AD Leo from 1000 - 3000Å combined with the reconstructed Ly-α from Linsky et al. (2013) for the region 1210 - 1222Å.[1] Note that young active stars are highly variable, especially in the UV. AD Leo is the most active and well characterized M dwarf. Our active models therefore represent the extreme high end of activity for each

---

[1] http://archive.stsci.edu/iue/

stellar type from an active flare star. For comparison, the inactive semi-empirical models include no chromospheric emission. The continuum originating from the photosphere is taken from a PHOENIX model with the same stellar parameters as the corresponding active star from 1000 - 45,450Å. Thus, these models provide only a lower limit to the stellar UV flux. More observations are needed to determine the true lower limit of inactive M dwarfs in the UV.

Table 3.1:: Stellar properties for active and inactive models.

Star	T_{eff} (K)	Mass ($M_\odot$)	Radius ($R_\odot$)
M0	3800	0.60	0.62
M1	3600	0.49	0.49
M2	3400	0.44	0.44
M3	3200	0.36	0.39
M4	3100	0.2	0.36
M5	2800	0.14	0.2
M6	2600	0.10	0.15
M7	2500	0.09	0.12
M8	2400	0.08	0.11
M9	2300	0.075	0.08

The models represent the extreme limits of the UV radiation environment for an exoplanet using a flare star for the upper bound and a photosphere-only model for the lower bound in the UV. Fig. 3.1 shows the UV flux region between those two limits spans over 10 orders of magnitude in the FUV. We use the observations of six M dwarfs from the MUSCLES program to probe the region in between our active and inactive models. The MUSCLES stars have been traditionally classified as “quiescent” because they do not present H_α in emission.

The six M dwarfs were observed by two UV spectrographs (COS and STIS) on HST

(France et al. 2013). We joined these HST measurements[2] with the star's corresponding PHOENIX models at 2800Å after adjusting the HST flux levels to the level a planet would receive at the 1AU equivalent in the Habitable Zone. The input parameters for the PHOENIX models are the observed star's $T_{\rm eff}$, [Fe/H], log g, and the rotation velocity, v sin i, as summarized in Table 3.2 and described for each star based on the most recent observations in the Appendix. When observations of v sin i were not available we used instead the peak of the observed distribution for 56 M dwarfs (Jenkins et al. 2009).

The MUSCLES database interpolates the region between 1760 - 2100 Å because the noise in the observations was large in that region since those wavelengths were covered by the lowest sensitivity part of the STIS G230L bandpass. In order to not bias the results too higher or too low, the MUSCLES team used the average flux in the 2100 - 2200 Å region to interpolate the 1760 - 2100 Å region. Follow up observations to the MUSCLES program with a new HST Treasury program aim to probe the 1760 - 2100 Å region of the spectrum with higher sensitivity. We used the MUSCLES database and interpolation as given. Because this region of the UV is important for O_3 production, uncertainty of this interpolation could influence our atmospheric results.

Input active stellar spectra and MUSCLES spectra are shown in Fig. 3.3 (inactive models are not shown).

---

[2] http://cos.colorado.edu/ kevinf/muscles.html

Table 3.2:: Stellar properties for MUSCLES model stellar spectra.

MUSCLES Stars	$T_{\rm eff}$ (K)	Radius ($R_\odot$)	[Fe/H]	log g	Age (Gyr)	v sin i (km s^{-1})
GJ 832	3620	0.48	-0.12	4.70	-	3^*
GJ 667C	3350	0.348	-0.55	5.00	> 2	3^*
GJ 1214	3250	0.211	+0.05	4.99	6±3	< 1
GJ 436	3416	0.455	+0.04	4.83	6.5-9.9	< 1
GJ 581	3498	0.299	-0.10	4.96	7-11	2.1
GJ 876	3129	0.3761	+0.19	4.89	0.1-5	1.38

Note: for GJ 832 and GJ 667C there is no v sin i measurement. We assumed a v sin $i = 3.0$ corresponding to the peak of the distribution (Jenkins et al. 2009) when generating a PHOENIX model.

See text for references.

3.2.2 Planetary Atmosphere Model

We use EXO-P (Kaltenegger & Sasselov 2010), a coupled 1D radiative-convective atmosphere code developed for rocky exoplanets. The code incorporates a 1D climate (Kasting & Ackerman 1986; Pavlov et al. 2000; Haqq-Misra et al. 2008), 1D photochemistry (Pavlov & Kasting 2002; Segura et al. 2005, 2007), and 1D radiative transfer model (Traub & Stier 1976; Kaltenegger & Traub 2009) to calculate the model spectrum of an Earth-like exoplanet orbiting host M dwarfs in the Habitable Zone.

EXO-P is a model that simulates both the effects of stellar radiation on a planetary environment and the planet's outgoing spectrum. We model an altitude range that extends upwards to 60km with 100 height layers. We use a geometrical model in which the average 1D global atmospheric model profile is generated using a plane-parallel atmosphere, treating the planet as a Lambertian sphere, and setting the stellar zenith angle to 60 degrees to represent the average incoming stellar flux on the dayside of the

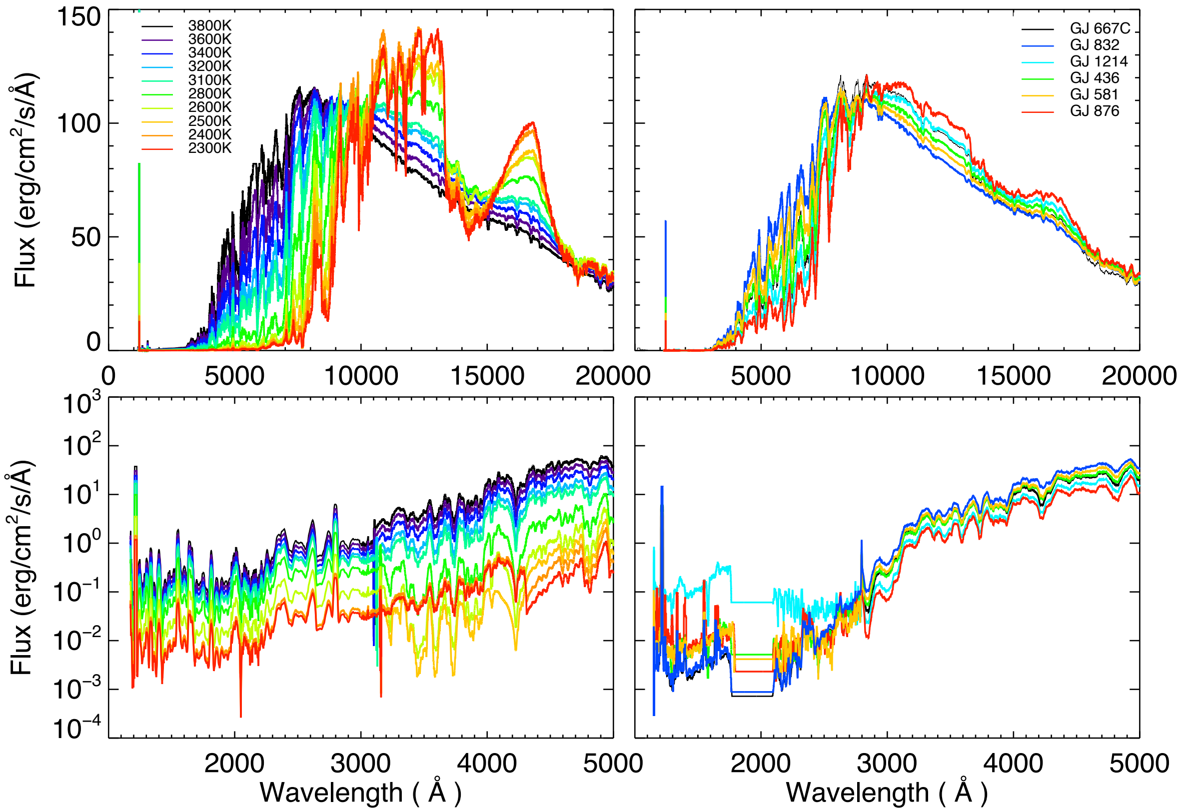

Figure 3.3: Stellar input spectra (top) from 1000 to 20000 Å for the M0-M9 active grid stars with UV scaled by H_α and AD Leo UV flux (left) and MUSCLES stars with HST UV observations (right). UV input stellar fluxes in log scale (bottom).

planet (see also Schindler & Kasting 2000). The temperature in each layer is calculated from the difference between the incoming and outgoing flux and the heat capacity of the atmosphere in each layer. If the lapse rate of a given layer is larger than the adiabatic lapse rate, it is adjusted to the adiabatic rate until the atmosphere reaches equilibrium. We use a two-stream approximation (see Toon et al. 1989), which includes multiple scattering by atmospheric gases, in the visible/near IR to calculate the shortwave fluxes. Four-term, correlated-k coefficients parameterize the absorption by O_3, H_2O, O_2, and CH_4 (Pavlov et al. 2000). In the thermal IR region, a rapid radiative transfer model

(RRTM) calculates the longwave fluxes. Clouds are not explicitly calculated. The effects of clouds on the temperature vs. pressure profile are included by adjusting the surface albedo of the Earth-Sun system to have a surface temperature of 288K (see Kasting et al. 1984; Pavlov et al. 2000; Segura et al. 2003, 2005). The photochemistry code, originally developed by Kasting et al. (1985) solves for 55 chemical species linked by 220 reactions using a reverse-Euler method (see Segura et al. 2010, and references therein). The photochemical model is stationary, and is converged to chemical equilibrium.

The radiative transfer model used to compute planetary spectra is based on a model originally developed for trace gas retrieval in Earth's atmospheric spectra (Traub & Stier 1976) and further developed for exoplanet transmission and emergent spectra (Kaltenegger et al. 2007; Kaltenegger & Traub 2009; Kaltenegger 2010; Kaltenegger & Sasselov 2010; Kaltenegger et al. 2013). In this paper, we model Earth's reflected and thermal emission spectra using 21 of the most spectroscopically significant molecules (H_2O, O_3, O_2, CH_4, CO_2, OH, CH_3Cl, NO_2, N_2O, HNO_3, CO, H_2S, SO_2, H_2O_2, NO, ClO, HOCl, HO_2, H_2CO, N_2O_5, and HCl). We use a Lambert sphere as an approximation for the disk integrated planet in our model. The surface of our model planet corresponds to Earth's current surface of 70% ocean, 2% coast, and 28% land. The land surface consists of 30% grass, 30% trees, 9% granite, 9% basalt, 15% snow, and 7% sand. Surface reflectivities are taken from the USGS Digital Spectral Library[3] and the ASTER Spectral Library[4] (following Kaltenegger et al. 2007).

Clouds have a strong impact on the detectability of atmospheric species. For the

---

[3] http://speclab.cr.usgs.gov/spectral-lib.html

[4] http://speclib.jpl.nasa.gov

spectra shown in Figs. 3.7-3.9, we assume a 60% global cloud cover with cloud layers analogous to Earth (40% water clouds at 1km, 40% water clouds at 6km and 20% ice clouds at 12km following Kaltenegger et al. 2007). In the VIS to NIR, clouds increase the reflectivity of an Earth-like planet substantially and therefore increase the equivalent widths of all observable features, even though clouds block access to some of the lower atmosphere. In the IR, clouds slightly decrease the overall emitted flux of an Earth-like planet because they radiate at lower temperatures and therefore decrease the equivalent widths of all observable absorption features, even though they can increase the relative depth of a spectral feature due to lowering the continuum temperature of the planet. For a comparison of scenarios with Earth-analogue clouds to those of clear sky spectra see Rugheimer et al. (2013).

Using 34 layers, we calculate the spectrum at high spectral resolution with several points per line width. The line shapes and widths are computed using Doppler and pressure broadening on a line-by-line basis for each layer in the model atmosphere. The overall high-resolution spectrum is calculated with 0.1 cm^{-1} wavenumber steps. The figures are shown smoothed to a resolving power of 150 in the IR and 800 in the VIS using a triangular smoothing kernel. The spectra may be binned further for comparison with proposed future spectroscopy missions designs to characterize Earth-like planets. We previously validated EXO-P from the VIS to the IR using data from ground and space (Kaltenegger et al. 2007; Kaltenegger & Traub 2009; Rugheimer et al. 2013).

3.2.3 Simulation Set-Up

To examine the effects of the varying UV flux of M dwarfs on an Earth-like atmosphere and its observable spectral features, we use the temperature grid of stellar models ranging from M9 to M0 (T_{eff} = 3800K to 2300K) for active and inactive models along with the six M dwarfs with well characterized UV fluxes from HST (see §3.2.2). We simulated an Earth-like planet with the same mass as the Earth at the 1AU equivalent orbital distance, defined by the wavelength integrated stellar flux received on top of the planet's atmosphere being equivalent to 1AU in our solar system calculated by $1\ AU_{eq} = AU \times \sqrt{(R/R_{\odot})^2 \times (T_{\mathrm{eff}}/T_{\mathrm{eff}\ \odot})^4}$.

The biogenic (produced by living organisms) fluxes were held fixed in the models in accordance with the fluxes that reproduce the modern mixing ratios in the Earth-Sun case, except for the cooler M dwarfs where CH_4 and N_2O were given a fixed mixing ratio of 1.0×10^{-3} and 1.5×10^{-2}, respectively (following Segura et al. 2003, 2005). The surface fluxes for the long-lived gases H_2, CH_4, N_2O, CO and CH_3Cl were calculated such that the Earth around the Sun yields a T_{surf} = 288K for surface mixing ratios: $cH_2 = 5.5 \times 10^{-7}$, $cCH_4 = 1.6 \times 10^{-6}$, $cCO_2 = 3.5 \times 10^{-4}$, $cN_2O = 3.0 \times 10^{-7}$, $cCO = 9.0 \times 10^{-8}$, and $cCH_3Cl = 5.0 \times 10^{-10}$ (see Rugheimer et al. 2013). The corresponding input surface fluxes to the atmosphere are -1.9×10^{12} g H_2 yr^{-1}, 5.3×10^{14} g CH_4 yr^{-1}, 7.9×10^{12} g N_2O yr^{-1}, 1.8×10^{15} g CO yr^{-1}, and 4.3×10^{12} g CH_3Cl yr^{-1}. The N_2 mixing ratio is set to be a "fill gas" such that the total surface pressure is 1 bar. These boundary conditions were used for M0-M5 active grid stars, M0-M3 inactive grid stars and all MUSCLES stars.

For M6-M9 active grid stars and for M4-M9 inactive grid stars, the boundary condition for CH_4 is changed to a fixed mixing ratio once the UV environment of the host star drops below a certain level because, CO, H_2, and CH_4 do not converge assuming a modern Earth biological flux (see also Segura et al. 2005). In reality, the thermodynamical cost for microbes producing CH_4 would become unprofitable as temperatures would initially rise due the increased greenhouse effect, causing the microbes to operate less efficiently. This type of biological feedback is not included in the models. CH_4 is produced biotically by methanogens and other organisms and abiotically through hydrothermal vent systems. In the modern atmosphere there is a significant anthropogenic source of CH_4 from natural gas, livestock, and rice paddies. Upper limits of abiotic fluxes of methane can be estimated for terrestrial planets following Guzmán-Marmolejo et al. (2014). An estimate of Earth biotic methane is about 30x the abiotic flux (see discussion in Segura et al. 2005), and thus a range of methane fluxes may be maintained on a terrestrial planet via methanogenesis in addition to abiotic methane production.

Therefore, we set the mixing ratio of CH_4 to 1×10^{-3} corresponding to a value of the last stable run with an Earth-like biological CH_4 flux for an active M5 star for planets around host stars that show this run-away behavior. Given these boundary conditions, the methane flux necessary to sustain a 1×10^{-3} mixing ratio of methane is 5.65×10^{14} g yr^{-1} (equal to our present Earth methane flux) for the planet around the hottest M dwarf ($T_{\rm eff} = 3800$ K) either active or inactive, 1.16×10^{14} g yr^{-1} (20.5% of the Earth value) for the planet around the coolest ($T_{\rm eff} = 2300$ K) active star, and 5.87×10^{12} g yr^{-1} (1% of the Earth value) for the coolest inactive M dwarf of our sample.

For the less active stars, we set the deposition velocity (rate at which they are deposited to the surface) for H_2 and CO to 2.4×10^{-4} cm s^{-1} and 1.2×10^{-4} cm s^{-1}, respectively (see also Segura et al. 2005; Kharecha et al. 2005). These deposition velocity values correspond to the maximum air-sea transfer rates estimated using the "piston velocity" approach (Broecker 1982; Kharecha et al. 2005). One study found CH_4 does not build up in quiescent late M dwarfs by increasing the H_2 deposition velocity to 7.7×10^4 cm s^{-1} (see Rauer et al. 2011). However, changes to any of the boundary conditions of the biological gases imply changes in biological activity, and current models are not constructed to manage biological fluxes in a self-consistent way on an exoplanet. Since a larger H_2 deposition velocity implies consumption by bacteria, we use the value in Kharecha et al. (2005).

We followed a similar procedure for constraining the N_2O concentrations for M6-M9 inactive stars. We set the mixing ratio of N_2O to 1.5×10^{-2}, corresponding to values of the last stable run with Earth-like biological fluxes, to prevent unphysical buildup of N_2O. N_2O is emitted primarily by (de)nitrifying bacteria with anthropogenic sources from fertilizers in agriculture, biomass burning, industry, and livestock and is a relatively minor constituent of the modern atmosphere at around 320 parts per billion (ppb), compared to the pre-industrial concentration of 270 ppb (Forster et al. 2007).

We used modern Earth fluxes for all of the MUSCLES stars without any run-away buildup of reduced gases. The CH_4 and N_2O fluxes are given in Table 3.3.

All of our simulations used a fixed mixing ratio of 355ppm for CO_2, 21% O_2, and a fixed upper boundary of 10^{-4} bar ($\sim$ 60km). In the 1D climate model, a surface albedo of 0.2 is fixed for all simulations, corresponding to the surface albedo that reproduces Earth's average temperature of 288K for the Earth/Sun case. The planetary Bond albedo (surface + atmosphere) is calculated by the 1D climate code.

Table 3.3:: CH_4 and N_2O fluxes and mixing ratios and O_3 column depths.

	Surface Mixing Ratio CH_4	Flux (g yr^{-1}) CH_4	% Earth CH_4 flux	Surface Mixing Ratio N_2O	Flux (g yr^{-1}) N_2O	% Earth N_2O flux	O_3 Column Depth (cm^{-2})
Active							
M0 A	330ppm	5.65×10^{14}	100%	0.70ppm	7.99×10^{12}	100%	4.1×10^{18}
M1 A	370ppm	5.65×10^{14}	100%	0.70ppm	7.99×10^{12}	100%	4.0×10^{18}
M2 A	450ppm	5.65×10^{14}	100%	0.76ppm	7.99×10^{12}	100%	3.8×10^{18}
M3 A	570ppm	5.65×10^{14}	100%	0.82ppm	7.99×10^{12}	100%	3.6×10^{18}
M4 A	910ppm	5.65×10^{14}	100%	0.93ppm	7.99×10^{12}	100%	3.5×10^{18}
M5 A	1000 ppm	5.65×10^{14}	100%	0.98 ppm	7.99×10^{12}	100%	2.6×10^{18}
M6 A	1000ppm	2.90×10^{14}	51.8%	1.7ppm	7.99×10^{12}	100%	3.1×10^{18}
M7 A	1000ppm	1.28×10^{14}	22.7%	3.0ppm	7.99×10^{12}	100%	2.4×10^{18}
M8 A	1000ppm	1.36×10^{14}	24.0%	3.1ppm	7.99×10^{12}	100%	2.5×10^{18}
M9 A	1000ppm	1.20×10^{14}	21.2%	3.5ppm	7.99×10^{12}	100%	2.3×10^{18}
Inactive							
M0 I	490 ppm	5.65×10^{14}	100%	34 ppm	7.99×10^{12}	100%	1.7×10^{18}
M1 I	580 ppm	5.65×10^{14}	100%	64 ppm	7.99×10^{12}	100%	1.5×10^{18}
M2 I	650 ppm	5.65×10^{14}	100%	120 ppm	7.99×10^{12}	100%	1.4×10^{18}
M3 I	1000 ppm	5.65×10^{14}	100%	360 ppm	7.99×10^{12}	100%	1.3×10^{18}
M4 I	1000ppm	4.15×10^{14}	73.5%	670ppm	7.99×10^{12}	100%	1.0×10^{18}
M5 I	1000ppm	1.23×10^{14}	21.8%	15000ppm	7.99×10^{12}	100%	4.5×10^{17}
M6 I	1000ppm	2.42×10^{13}	4.3%	15000ppm	4.04×10^{11}	5.1%	1.4×10^{17}
M7 I	1000ppm	1.67×10^{13}	3.0%	15000ppm	4.96×10^{10}	0.6%	6.1×10^{16}
M8 I	1000ppm	1.34×10^{13}	2.4%	15000ppm	5.72×10^{9}	0.07%	2.6×10^{16}
M9 I	1000ppm	5.87×10^{12}	1.0%	15000ppm	3.17×10^{9}	0.04%	1.1×10^{16}

Continued on next page

Table 3.3:: CH_4 and N_2O fluxes and mixing ratios and O_3 column depths. – continued from previous page

	Surface Mixing Ratio CH_4	Flux (g yr^{-1}) CH_4	% Earth CH_4 flux	Surface Mixing Ratio N_2O	Flux (g yr^{-1}) N_2O	% Earth N_2O flux	O_3 Column Depth (cm^{-2})
MUSCLES							
GJ 832	550ppm	5.65×10^{14}	100%	15ppm	7.99×10^{12}	100%	1.6×10^{18}
GJ 667C	330ppm	5.65×10^{14}	100%	0.7ppm	7.99×10^{12}	100%	7.0×10^{18}
GJ 1214	1600ppm	5.65×10^{14}	100%	1.1ppm	7.99×10^{12}	100%	2.3×10^{18}
GJ 436	1600ppm	5.65×10^{14}	100%	4.3ppm	7.99×10^{12}	100%	1.1×10^{18}
GJ 581	1400ppm	5.65×10^{14}	100%	2.9ppm	7.99×10^{12}	100%	1.2×10^{18}
GJ 876	3400ppm	5.65×10^{14}	100%	6.9ppm	7.99×10^{12}	100%	8.8×10^{17}

3.3 Atmospheric Model Results

The amount of UV radiation emitted from the host star influences the abundances of major chemical atmospheric constituents including H_2O, CH_4, and O_3 and, as a result, modified the temperature-pressure profile of a planet. The UV fluxes incident at the top of the atmosphere of an Earth-like planet in the HZ are given in Table 3.4 and shown in Fig. 3.3. An M0 active star model has 6.7 times more total UV flux than an M0 inactive star model. An M9 active star model has 4600 times more total UV flux than an M9 inactive star model. The greatest differences are in the far UV (FUV 1000 - 2000 Å) where an active star model has 6.8×10^4 and 1.3×10^{11} more FUV flux than an inactive M0 and M9 model, respectively. The MUSCLES stars' UV environments fall between the active and inactive star models, consistent with their classification as being weakly active.

The temperature vs altitude profile and the H_2O, O_3, CH_4 and N_2O mixing ratio profiles for all of the simulations are shown in Fig. 3.4, with each row corresponding to active, inactive, and MUSCLES star models, respectively. CH_3Cl profiles are not shown here, but follow the same trends as CH_4. Since both O_2 and CO_2 are well mixed in the atmosphere, their vertical mixing ratio profiles of 0.21 and 355ppm, respectively, are not shown.

Table 3.4:: Integrated UV fluxes at the top of the atmosphere (TOA).

Stellar Type	Ly-α TOA 1210-1222Å ergs cm^{-2} s^{-1}	FUV minus Ly-α TOA 1222-2000Å ergs cm^{-2} s^{-1}	FUV TOA 1000-2000Å ergs cm^{-2} s^{-1}	NUV TOA 2000-3200Å ergs cm^{-2} s^{-1}	Full UV TOA 1000-3200Å ergs cm^{-2} s^{-1}
Active					
M0 A	6.9×10^{2}	2.4×10^{2}	9.4×10^{2}	1.4×10^{3}	2.3×10^{3}
M1 A	5.6×10^{2}	2.0×10^{2}	7.6×10^{2}	1.1×10^{3}	1.9×10^{3}
M2 A	4.4×10^{2}	1.6×10^{2}	6.1×10^{2}	8.5×10^{2}	1.5×10^{3}
M3 A	3.5×10^{2}	1.2×10^{2}	4.7×10^{2}	6.5×10^{2}	1.1×10^{3}
M4 A	3.1×10^{2}	1.1×10^{2}	4.2×10^{2}	5.6×10^{2}	9.8×10^{2}
M5 A	1.8×10^{2}	6.3×10^{1}	2.5×10^{2}	3.3×10^{2}	5.8×10^{2}
M6 A	6.4×10^{1}	2.3×10^{1}	8.8×10^{1}	1.2×10^{2}	2.1×10^{2}
M7 A	2.6×10^{1}	9.2×10^{0}	3.6×10^{1}	4.8×10^{2}	8.4×10^{2}
M8 A	2.6×10^{1}	9.0×10^{0}	3.5×10^{1}	4.7×10^{2}	8.2×10^{2}
M9 A	2.2×10^{1}	7.6×10^{0}	3.0×10^{1}	3.9×10^{2}	6.9×10^{2}
Inactive					
M0 I	2.7×10^{-11}	9.4×10^{-3}	9.5×10^{-3}	3.0×10^{2}	3.0×10^{2}
M1 I	5.8×10^{-12}	2.9×10^{-3}	2.9×10^{-3}	2.6×10^{2}	2.6×10^{2}
M2 I	1.5×10^{-12}	9.1×10^{-4}	9.1×10^{-4}	1.7×10^{2}	1.7×10^{2}
M3 I	3.5×10^{-14}	6.9×10^{-5}	6.9×10^{-5}	8.9×10^{1}	8.9×10^{1}
M4 I	6.1×10^{-15}	2.2×10^{-5}	2.2×10^{-5}	5.9×10^{1}	5.9×10^{1}
M5 I	2.9×10^{-19}	1.5×10^{-8}	1.5×10^{-8}	1.3×10^{1}	1.3×10^{1}
M6 I	4.2×10^{-21}	2.6×10^{-9}	2.6×10^{-9}	3.0×10^{0}	3.0×10^{0}
M7 I	1.1×10^{-21}	2.6×10^{-10}	2.6×10^{-10}	1.3×10^{0}	1.3×10^{0}
M8 I	8.3×10^{-24}	1.7×10^{-10}	1.7×10^{-10}	5.0×10^{-1}	5.0×10^{-1}
M9 I	1.8×10^{-24}	1.6×10^{-10}	1.6×10^{-10}	1.3×10^{-1}	1.3×10^{-1}

Continued on next page

Table 3.4:: Integrated UV fluxes at the top of the atmosphere (TOA). – continued from previous page

Stellar Type	Ly-α TOA 1210-1222Å ergs cm^{-2} s^{-1}	FUV minus Ly-α TOA 1222-2000Å ergs cm^{-2} s^{-1}	FUV TOA 1000-2000Å ergs cm^{-2} s^{-1}	NUV TOA 2000-3200Å ergs cm^{-2} s^{-1}	Full UV TOA 1000-3200Å ergs cm^{-2} s^{-1}
MUSCLES					
GJ 832	1.5×10^2	3.0×10^0	1.5×10^2	3.5×10^2	5.0×10^2
GJ 667C	1.2×10^2	2.4×10^0	1.3×10^2	2.3×10^2	3.6×10^2
GJ 1214	1.4×10^0	9.9×10^1	1.1×10^2	1.8×10^2	2.8×10^2
GJ 436	6.1×10^1	7.1×10^0	6.8×10^1	2.3×10^2	2.9×10^2
GJ 581	4.2×10^1	6.8×10^0	5.0×10^1	2.7×10^2	3.2×10^2
GJ 876	3.4×10^1	1.1×10^1	4.9×10^1	1.1×10^2	1.6×10^2

In the first column of Fig. 3.4, we show the changes in the temperature/altitude profile for Earth-like atmosphere models around M dwarfs for active (top row), inactive (middle row) and the six observed MUSCLES stars (bottom row). All temperature inversions are weaker than for the modern Earth because M dwarfs emit low UV flux in the 2000 - 3000 wavelength region, thereby producing near isothermal stratospheres (see also Segura et al. 2005). Fig. 3.4 shows that temperature inversions are weaker for the higher UV environment stars. This is counter-intuitive since for the modern Earth, O_3 absorption of UV radiation causes stratospheric heating and an inversion. However in these lower UV environments, additional heating is provided by stratospheric CH_4 and H_2O.

H_2O concentrations are lower in the stratosphere for planets around M dwarf models with higher UV fluxes, although higher O_3 concentrations will act as a shield, partially offsetting the effect of higher UV photon fluxes (Fig. 3.4, 2nd column). H_2O can also be formed in the stratosphere from CH_4 and OH ($CH_4 + OH \rightarrow CH_3 + H_2O$) and by increased upwards vertical transport in the nearly isothermal stratospheres of Earth-like planets orbiting M dwarfs (see also Segura et al. 2005). O_3 shields H_2O in the troposphere from UV environments. While photochemically inert in the troposphere, H_2O can be removed by photolysis at wavelengths shortward of 2000Å in the stratosphere (see columns 2 & 3 in Table 3.4) or by reactions with excited oxygen, $O(^1D)$, to produce OH radicals.

In an atmosphere containing O_2, O_3 concentrations are determined primarily by the absorption of UV light shortward of 2400Å in the stratosphere, and we see a corresponding decrease in O_3 concentrations correlated with decreased FUV radiation for cooler M dwarfs as well as inactive versus active stars (Fig. 3.4, 3rd column).

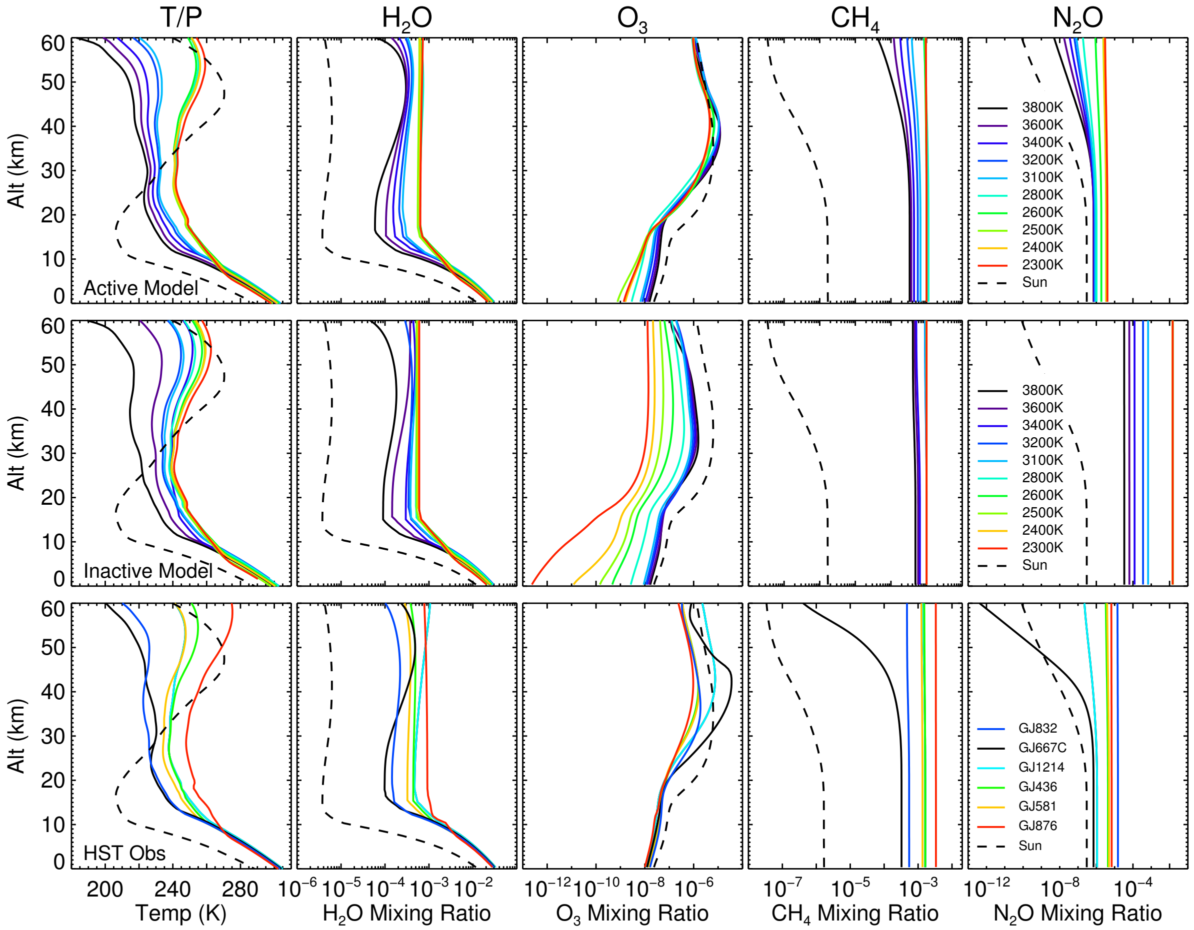

Figure 3.4: Planetary temperature vs. altitude profiles and mixing ratio profiles profiles for H_2O, O_3, CH_4 and N_2O (left to right) for an Earth-like planet orbiting the grid of active stellar models (top), inactive stellar models (middle), and MUSCLES stars (bottom). Earth-Sun profiles are shown for comparison (dashed black lines).

CH_4 mixing ratio profiles are shown in column 4 of Fig. 3.4. As mentioned previously, we set the mixing ratio of methane to be 1000 ppm for the later M dwarf spectral types as described in §3.2.3 and Table 3.3. For Earth-like CH_4 fluxes, CH_4 concentrations decrease with higher UV environments due to reactions with OH to form H_2O and by photolysis by $\lambda < 1500$ Å (Fig. 3.4, 4th column).

N_2O mixing ratios are larger for cooler M dwarfs because cooler stars have smaller UV fluxes at $\lambda < 2200$ Åand thus lower photolysis rates. Around later M dwarfs, we see mixing ratios of N_2O that increase unrealistically for the inactive stellar models M6-M9, similar to CH_4 (Fig. 3.4, 5th column). Since such a run-away effect should not be sustainable by biology, we cap the N_2O to a fixed mixing ratio corresponding to the last stable run for the inactive model M5. N_2O is also an indirect sink for stratospheric O_3, since about 1% is converted to NO. Therefore, increasing N_2O decreases O_3 abundance.

OH concentrations decrease with decreasing UV levels (in cooler and inactive M dwarfs) and OH is a primary sink for many species in the atmosphere including, but not limited to, many biologically interesting species including CH_4, CH_3, HCl, H_2, H_2S and CH_3Cl. CH_3Cl concentrations increase for cooler and inactive M dwarfs due to decreased stellar UV flux.

O_2 and CO_2 concentrations remain constant and well mixed for all stellar types.

The planetary surface temperatures range between 297 - 304K and Bond albedos range between 0.108 - 0.06 for M0 to M9 stars, respectively (see Fig. 3.5). These albedos are lower than Earth's Bond albedo of 0.3 around the Sun because the stellar spectral energy distributions peak at longer wavelengths for cooler stars where Rayleigh scattering is less efficient, assuming the same total insolation.

3.3.1 Effect of Ly-α

Ly-α is the brightest line in the UV spectra for cool stars and accounts for a significant portion of the overall UV flux. However, the intrinsic Ly-α flux must be reconstructed to account for interstellar absorption by neutral hydrogen (see Wood et al. 2005; Linsky

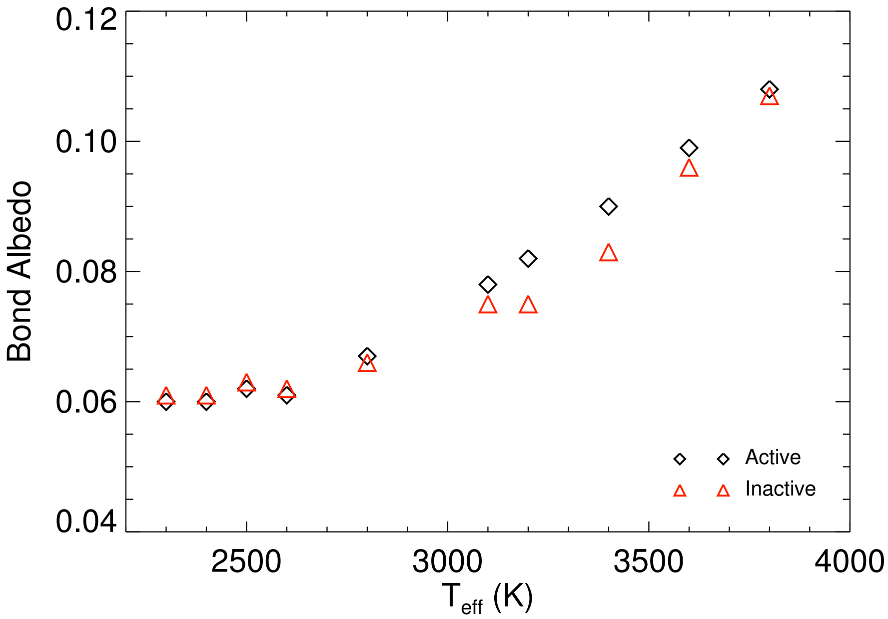

Figure 3.5: Calculated Bond albedos for Earth-like planets orbiting the M0-M9 Active (black diamond) and Inactive (red triangle) stellar models.

et al. 2013). For the observed MUSCLES stars, the Ly-α line flux is 13-33% the total UV flux excluding Ly-α. GJ 1214 has no observed Ly-α and only an upper limit which is 0.5% of the total UV flux (France et al. 2013). In our active models, Ly-α ranges from 2 to 17% of the total UV flux based on observations of AD Leo. In the inactive models (i.e. no chromosphere) Ly-α is negligible compared with total UV flux.

We ran two sensitivity tests of the photochemistry of Earth-like planets to the amount of Ly-α flux from their host star. First we increased the Ly-α by a factor of 10^3, 10^6, 10^9, 10^{12} and 10^{15} above M0 inactive model corresponding to flux levels of 2.7×10^{-8}, 2.7×10^{-5}, 2.7×10^{-2}, 2.7×10^{1}, 2.7×10^{4} ergs cm^{-2} s^{-1} respectively. The highest Ly-α value considered is 84x higher than that of the M0 active model and 180x higher than the highest observed Ly-α flux in the MUSCLES stellar sample. As seen in Fig. 3.6 (top), increasing the Ly-α flux has only a small effect on the photochemistry

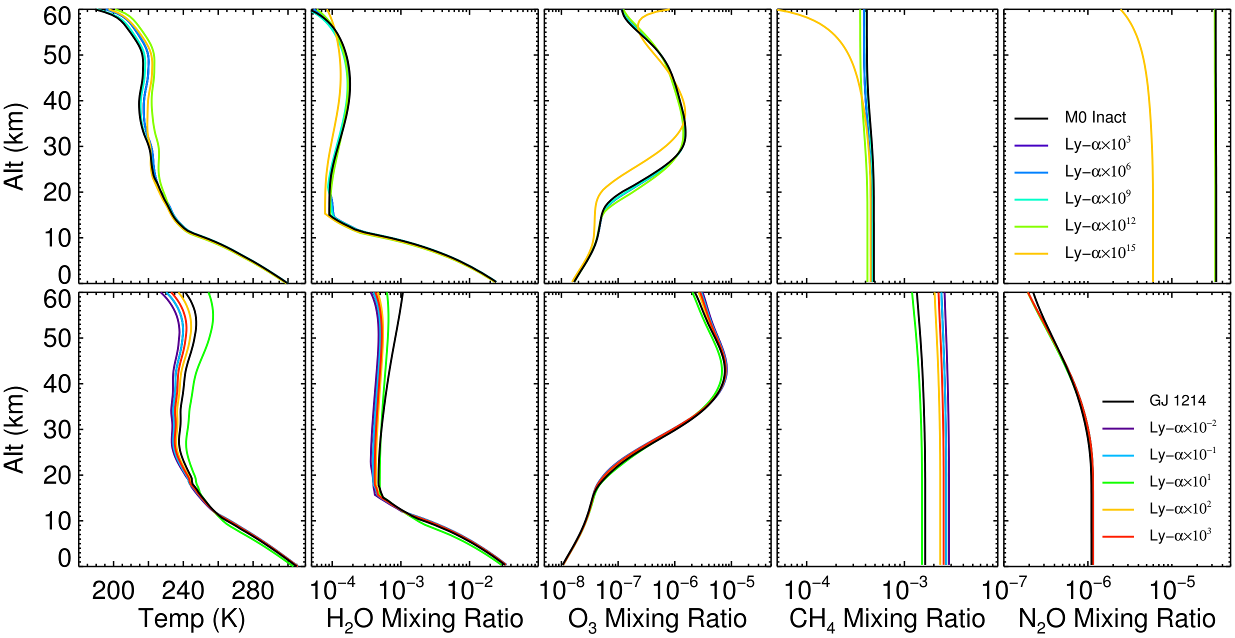

Figure 3.6: Temperature, H_2O, O_3, CH_4, and N_2O mixing ratio profiles where the Ly-α has been increased by a factor of 10^3, 10^6, 10^9, 10^{12} and 10^{15} above the inactive M0 model star corresponding to flux levels of 2.7×10^{-8}, 2.7×10^{-5}, 2.7×10^{-2}, 2.7×10^{1}, 2.7×10^{4} ergs cm^{-2} s^{-1}, respectively (top) and for GJ 1214 where the Ly-α upper limit (2.4×10^{-15} ergs cm^{-2} s^{-1}) has been multiplied by a factor of 10^{-2}, 10^{-1}, 10^{1}, 10^{2} and 10^{3} (bottom)

until the most extreme case considered where it primarily photolyzes N_2O and CH_4. We run our models to around 60km corresponding to a pressure of 1×10^{-4} bar. The effect of Ly-α will be more pronounced at pressures lower than this as Miguel et al. (2015) has shown for mini-neptune atmospheres.

GJ 1214 is the only MUSCLES star to not have a directly detected Ly-α flux. An upper limit was placed at 2.4×10^{-15} ergs cm^{-2} s^{-1}. We artificially set the Ly-α flux to be 10^{-2}, 10^{-1}, 10^{1}, 10^{2}, and 10^{3} times this upper limit. We tested values both above and below the upper limit to see how sensitive an Earth-like planet atmosphere is to changes in Ly-α flux when the rest of the NUV radiation field is still much higher than the inactive model in the previous sensitivity test. As shown in Fig. 3.6 (bottom), the largest changes are seen in the CH_4 and to a smaller extent in stratospheric H_2O concentrations. O_3 and N_2O remain relatively constant through the 5 orders of magnitude change in Ly-α flux.

Figures 3.4 and 3.6 show it is important to characterize the entire UV spectrum including the near UV and the base level flux between emission lines, to understand future observations of extrasolar planet atmospheres. Ly-α is one of the most important lines to characterize.

3.4 Results: Spectra of Earth-like Planets Orbiting M Dwarfs

Spectra of Earth-like planets orbiting M dwarfs with varying UV activity levels show measureable differences in spectral feature depths. In the VIS, the depth of absorption features is primarily sensitive to the abundance of the species, while in the IR, both the abundance and the temperature difference between the emitting/absorbing layer and the continuum influence the depth of features.

We assume full phase (secondary eclipse) for all spectra presented to show the maximum flux that can be observed. Figs 3.7-3.12 show an Earth-size planet to determine the specific flux and planet-to-star contrast ratio. A Super-Earth with up to twice Earth's radius will provide 4 times more flux and a better contrast ratio. No noise has been added to these model planetary spectra to provide inputs for a wide variety of instrument simulators for both secondary eclipse and direct detection missions.

3.4.1 Earth-like Visible/Near-infrared Spectra (0.4μm - 4μm)

Fig. 3.7 shows the reflected visible and near-infrared spectra from 0.4 to 2μm of Earth-like planets around the M dwarf grid of active, inactive, and MUSCLES stars, using the SED of the host star. We assume Earth-analogue cloud cover. The high-resolution spectra calculated with 0.1 cm^{-1} steps have been smoothed to a resolving power of 800 using a triangular smoothing kernel to show the individual features more clearly. The Earth-Sun spectrum is shown for comparison as a dashed black line.

Due to the increased stellar flux at shorter wavelengths for a G-type star, Rayleigh scattering is much more pronounced for FGK stars, which greatly increases the flux from 0.4 to 0.8μm for an Earth-like planet around a hotter star. Since M dwarfs have stronger NIR emission, and the 1-2μm flux is larger around Earth-like planets orbiting M dwarfs than for the Earth-Sun equivalent. The most notable features in the VIS/NIR spectra are O_3 at 0.6μm (the Chappuis band), O_2 at 0.76μm, H_2O at 0.95μm, and CH_4 at 0.6, 0.7, 0.8, 0.9, 1.0 and 1.7μm. Note that shallow spectral features like the visible O_3 feature would require a very high signal-to-noise ratio (SNR) to be detected.

Fig. 3.8 shows details for one of the most notable feature in the VIS, the O_2 A band at 0.76μm in both the relative flux as planet-to-star contrast ratio (left), and the reflected emergent flux for a 60% cloud cover model for M0-M9 model stars (top middle), and for the six MUSCLES stars (top right). Note that the detectability of the O_2 feature in reflected light is similar for active and inactive models since the stellar flux at 0.76μm is activity independent. The relative flux shows an equivalently deep feature for each case due to a constant mixing ratio of 21%. However, the oxygen feature in absolute flux (Fig. 8, upper middle panel) becomes increasingly difficult to detect for the later stellar types.

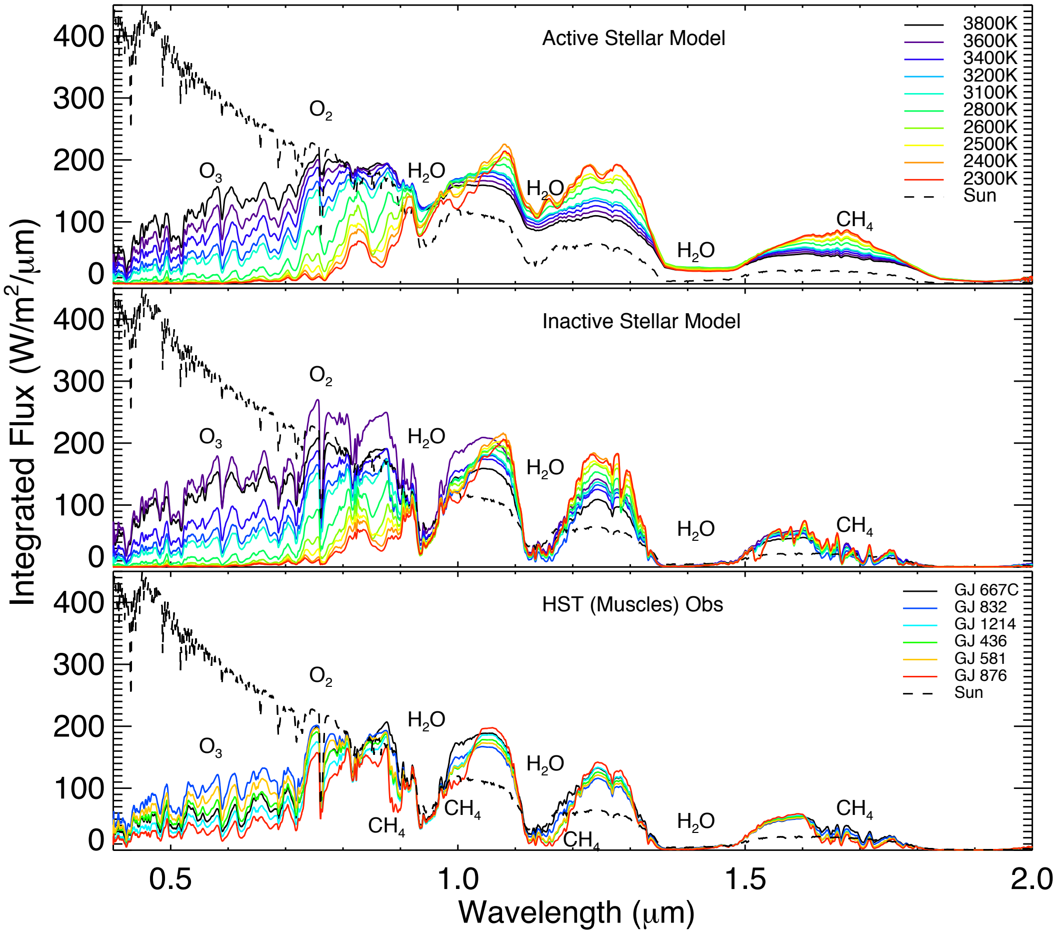

Figure 3.7: Smoothed, disk-integrated VIS/NIR spectra at the TOA for an Earth-like planet for the grid of active stellar models (top), inactive stellar models (middle), and MUSCLES stars (bottom) assuming 60% Earth-analogue cloud coverage model (region 2-4μm has low integrated flux levels and therefore is not shown here). The Earth-Sun spectrum is shown for comparison as a dashed black line.

For the latest M stellar types modeled here, the detection of the O_2 feature requires a very high SNR to detect even if the planet has an active photosynthetic biosphere like the Earth (see Fig. 3.7). If one assumes a blackbody radiation Planck function, rather than a realistic stellar model, when calculating the shape of the reflected light curve, the reduction in the feature's depth is less pronounced (see Fig. 3.8 bottom row). The O_2

feature is pronounced for all MUSCLES stars since none of those stars have a low enough T_{eff} for the O_2 feature to be diminished by the spectral energy distribution (SED). GJ 876 is the coolest MUSCLES star with T_{eff}=3129K and in our models the O_2 feature becomes most obscured for stars with T_{eff} = 2300K - 2600K.

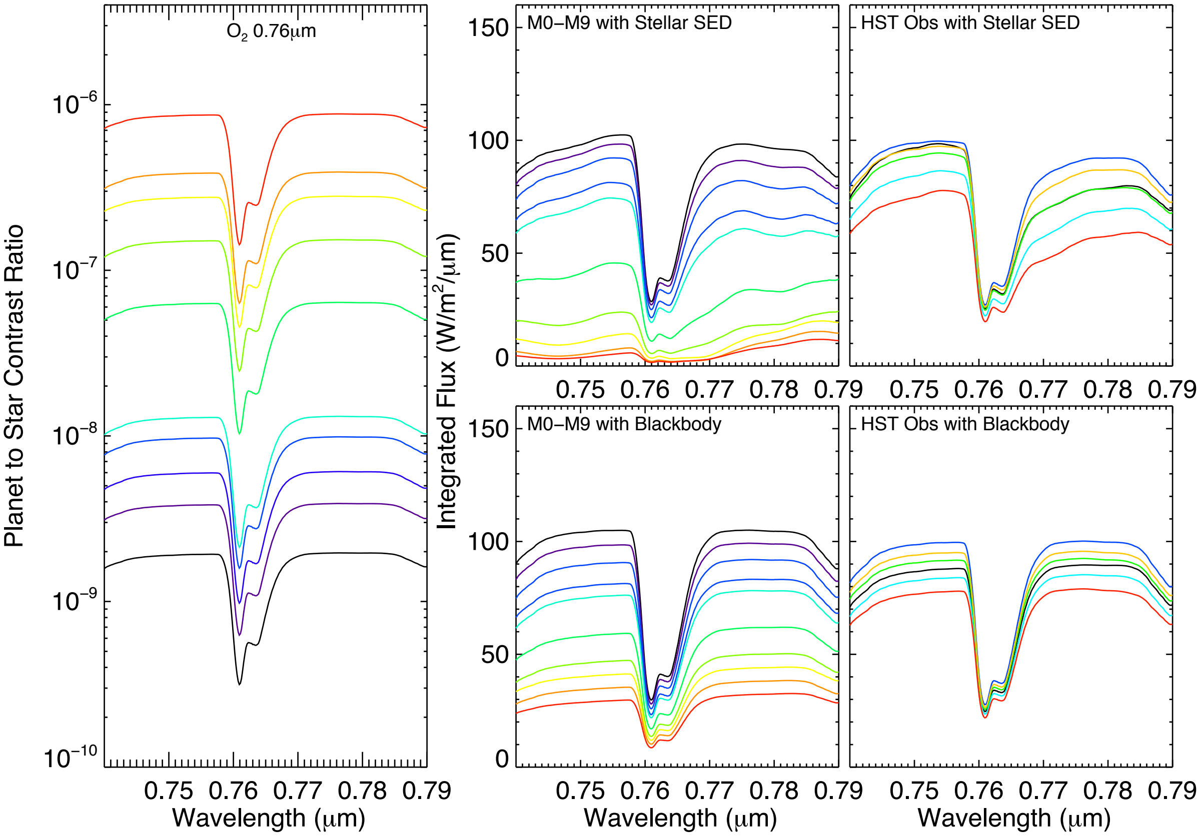

Figure 3.8: O_2 feature at 0.76μm relative flux as planet-to-star contrast ratio (left), and the reflected emergent flux for a 60% cloud cover model for M0-M9 model stars (top middle), and for MUSCLES stars (top right). Bottom row shows the same but with a blackbody used to calculate the absolute flux. The observable O_2 feature becomes increasingly difficult to detect for later stellar types due to the decreasing stellar flux in this wavelength region. Coloring is same as in Fig. 3.7.

CH_4 also has several features of interest in the VIS/NIR range at 0.6, 0.7, 0.8, 0.9, 1.0 and 1.7μm (see Fig. 3.9). The CH_4 feature is deeper for less active and cooler M dwarfs. In particular, the CH_4 features at 0.8, 0.9 and 1.0μm become much more pronounced for the cooler M dwarfs and for some of the MUSCLES stars such as GJ 876.

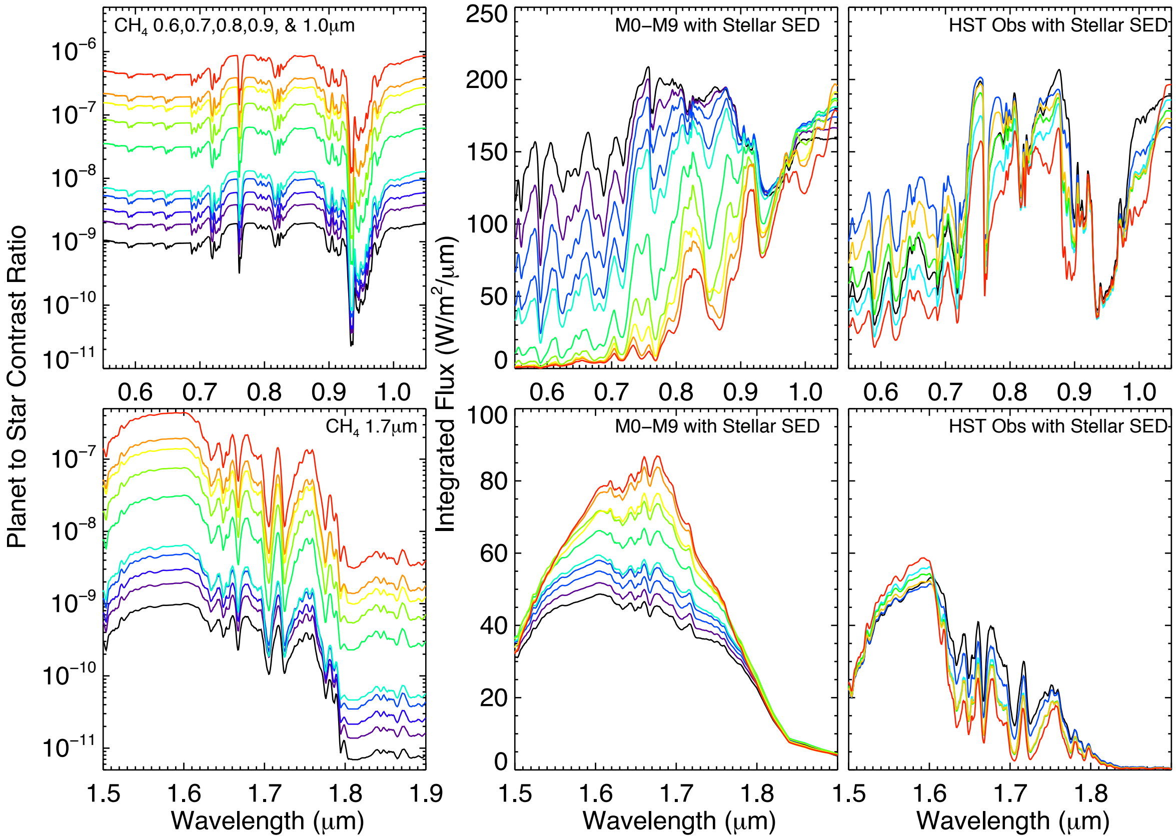

Figure 3.9: CH_4 features at 0.6, 0.7, 0.8, 0.9, and 1.0μm (top row) and the CH_4 feature at 1.7μm (bottom row) for the relative flux as planet-to-star contrast ratio (left), and the reflected emergent flux for a 60% cloud cover model for M0-M9 model stars (middle), and for MUSCLES stars (right). The observable CH_4 feature becomes deeper for planets orbiting cooler and less active star models. Coloring is same as in Fig. 3.7.

H_2O several features in the VIS/NIR at 0.95, 1.14 ,1.41 and 1.86μm and are deeper for cooler and less active stars (see Fig. 3.7).

Clouds increase reflectivity but can also decrease the depth of all observable features compared to the clear sky case. It will be difficult, therefore, to remotely determine the absolute abundance of a molecule without a well-characterized temperature vs. pressure distribution as well as cloud profile.

3.4.2 Earth-like Infrared Spectra, IR (4μm - 20μm)

Fig. 3.10 shows the thermal emission spectra from 4 to 20μm of Earth-like planets with Earth-analogue cloud cover around the M dwarf grid of active, inactive, and MUSCLES stars using the stellar SED. The high-resolution spectra have been smoothed to a resolving power of 150 using a triangular smoothing kernel to show the resolution expected by JWST. The Earth-Sun IR spectrum is shown for comparison as a dashed black line. Fig. 3.11 shows the individual component gas contributions of the dominate gases (H_2O, CH_4, CO_2, CH_3Cl, O_3, and N_2O) to the final IR planetary spectrum for an M9 active and inactive stellar model.

The depth of the O_3 feature at 9.6μm decreases for planets orbiting cooler and less active M dwarfs, as expected due to lower O_3 abundances for lower UV incident flux and also due to the decreased temperature difference between the O_3 emitting layer (around 40km) and the surface temperature, which is larger for the earlier M dwarfs as seen in Fig. 3.4.

The CH_4 feature at 7.7μm, decreases in depth for planets orbiting cooler M dwarfs despite increasing CH_4 abundances making it difficult to remotely determine the CH_4 abundance without a well-characterized temperature vs. pressure profile. Note that the 7.7μm feature is partially obscured by the wings of the H_2O feature at 5-8μm.

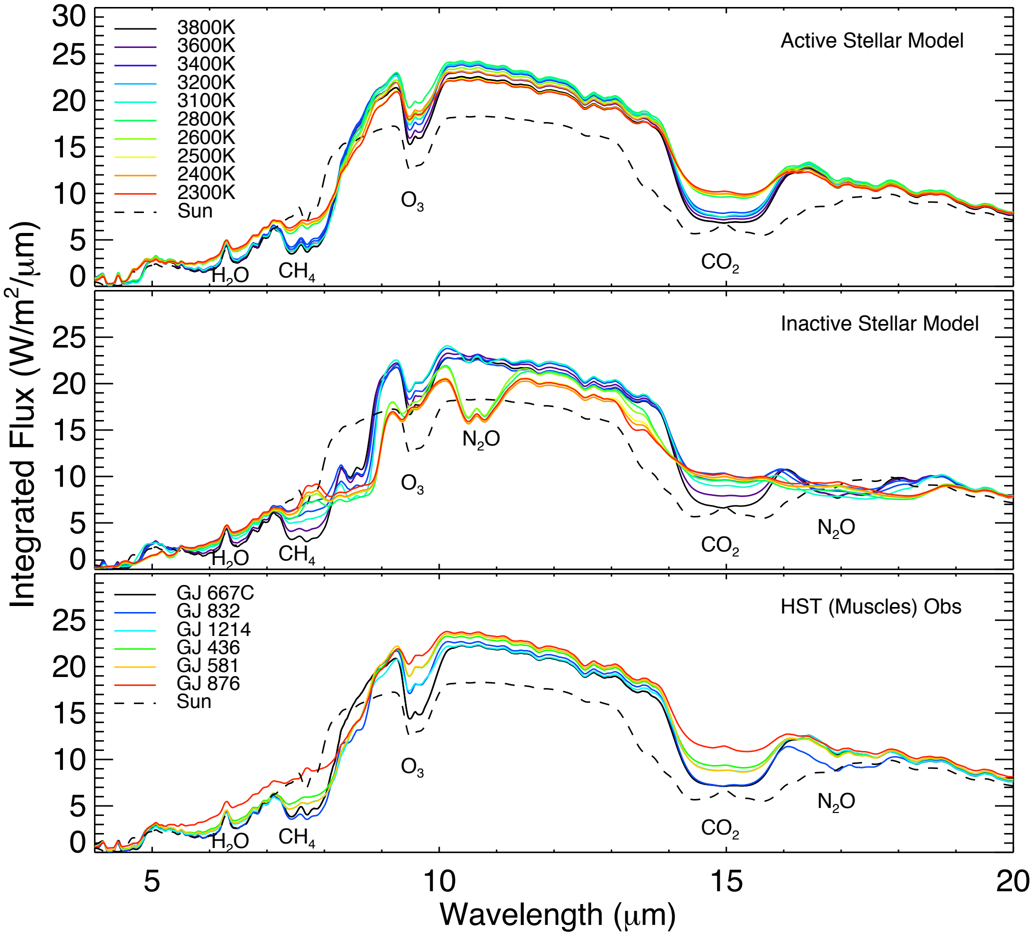

Figure 3.10: Smoothed, disk-integrated IR spectra at the TOA emitted by an Earth-like planet orbiting the grid of active stellar models (top), inactive stellar models (middle), and MUSCLES stars (bottom) assuming 60% Earth-analogue cloud coverage model. The Earth-Sun spectrum is shown for comparison as a dashed black line.

The N_2O features are the most striking addition in the inactive models with low UV flux. N_2O has features at 7.75μm (overlapping with the CH_4 feature), 8.5μm, 10.65μm and 16.9μm (see Fig. 3.11) that become deeper with decreasing UV flux. In the active M0-M9 stellar models we do not see any strong N_2O features, although it does contribute to the depth of the 7.7 CH_4 feature. For the inactive M5-M9 models we see

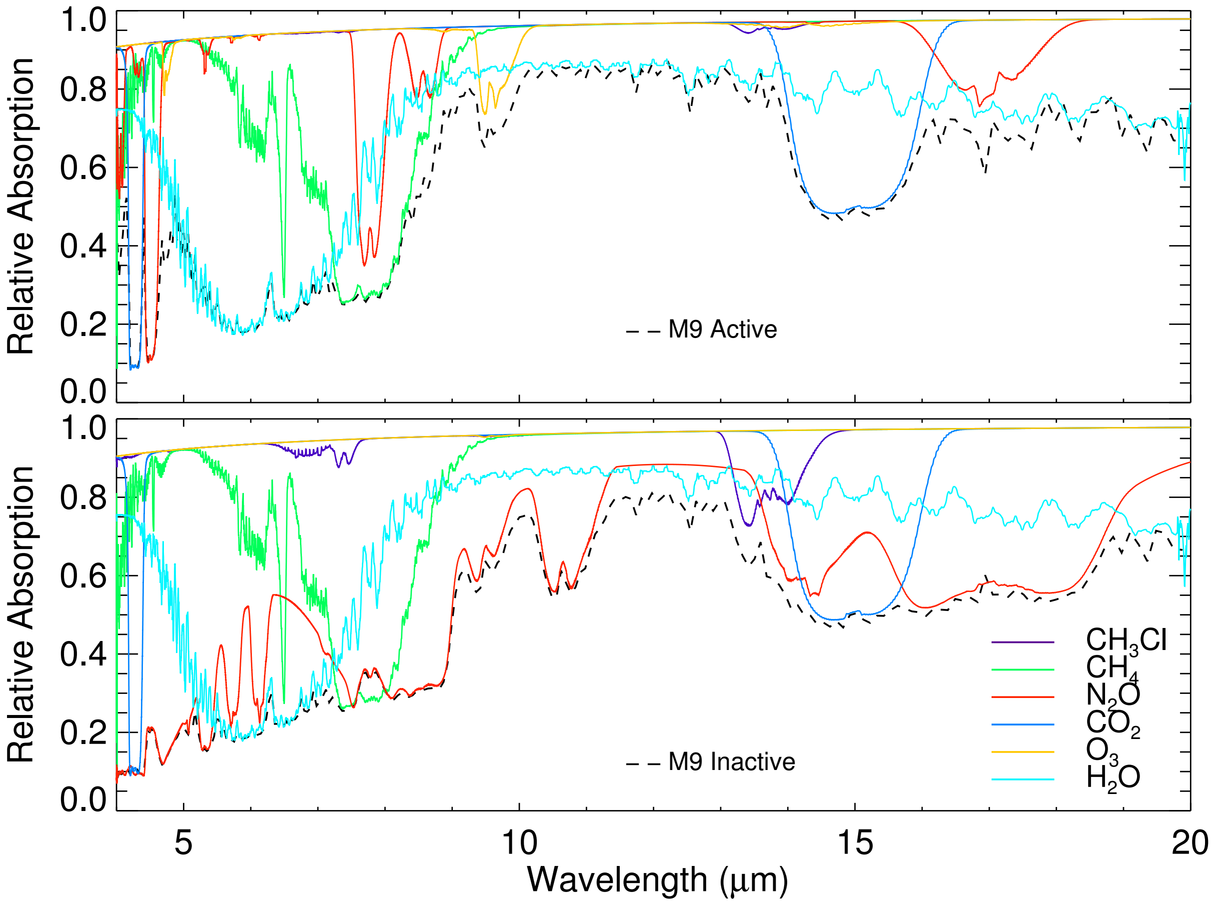

Figure 3.11: Individual spectral components for H_2O, CH_4, CO_2, CH_3Cl, O_3, and N_2O comprising the full IR spectra (shown by a dashed black line) for an Earth-like planet orbiting a M9 active stellar model (top) and M9 inactive stellar model (bottom).

a strong N_2O feature at 10.65μm and wide absorption from 14-19μm due to the strong build-up of N_2O in low UV environments assuming an Earth-like biological surface flux of 7.99×10^{12} g yr^{-1} (see §3.2 and §3.3). However, even for modest mixing ratios of 15ppm to 34ppm in GJ 832 and the M0 inactive models, respectively, we see a strong N_2O feature at 16.9μm. These concentrations are not much higher than the model mixing ratios calculated for the other MUSCLES stars and the later active M dwarf models. N_2O has been considered to be a strong biosignature (see e.g. Segura et al. 2005; Seager et al. 2012) and will be easier to detect around M dwarfs - especially inactive ones - than around FGK stars.

The CO_2 absorption feature at 15μm does not have a central emission peak, usually seen in F and G stars, due to the more isothermal stratospheres of planets around all M dwarfs.

The depth of the H_2O feature at 5-8μm decreases for later M dwarfs despite increasing stratospheric H_2O concentrations.

Clouds reduce the continuum level and the depth of all of the observable features compared to the clear sky case. Therefore, it will be difficult to remotely determine absolute abundances without a well-characterized temperature vs. pressure distribution as well as cloud profile.

Observability of Biosignatures: Detecting the combination of O_2 or O_3 and a reducing gas like CH_4 in emergent spectra and in secondary eclipse measurements requires observations either in the IR between 7 and 10μm that includes the 7.7μm CH_4 and 9.6μm O_3 features, or observations in the VIS to NIR between 0.7 to 3μm that includes the 0.76μm O_2 and 2.4μm CH_4 features in the observed spectral range. The strengths of absorption features (see Fig. 3.7 and 3.11 for VIS/NIR and IR, respectively) depend on the effective temperature of the host star as well as its UV flux and vary significantly between stellar types (see Fig. 3.7-3.11).

In the IR, CH_4 at 7.7μm is more easily detected at low resolution for earlier grid stars (M0-M4) than for later grid stars (M5-M9) in the active models.

The 9.6μm O_3 feature is deepest in earlier and/or more active M dwarfs where there are more UV photons. For M5-M9 inactive models, O_3 is not detectable in low resolution at 9.6μm due to the extremely low UV flux for these models. The narrow O_2 feature in the VIS at 0.72μm becomes weaker for cooler M dwarfs even though the mixing ratio of O_2 remains fixed in our simulations at 21%. This is a consequence of the faint spectral energy distributions at shorter wavelengths for both active and inactive late M stellar models.

For the modern Earth, N_2O and CH_3Cl do not contribute substantially to the spectrum due to their low mixing ratios and will likely be undetectable by the first low-resolution and photon-limited exoplanet atmosphere characterization missions (Selsis 2000; Kaltenegger et al. 2007). However, both N_2O and CH_3Cl reach detectable levels in the IR spectra for our models of cooler and less active stars due to low photolysis rates even though N_2O has many absorption features in the IR (see Fig. 3.11).

N_2O is considered a strong biosignature because there are no significant abiotic sources (Des Marais et al. 2002). One MUSCLES star, GJ 832, has a noticeable N_2O feature at 17μm with 15ppm for a modern Earth-like flux. This case is interesting because GJ 832 has the highest total FUV flux at wavelengths where N_2O is photolyzed (1000-2400Å). We find that the high Ly-α flux of GJ 832 promotes the destruction of O_3, producing more $O(^1D)$ which then reacts with N_2 to form N_2O.

For planets orbiting inactive M5-M9 star models we observe a sharp increase in N_2O concentrations as a consequence of few available UV photons. N_2O features dominate the spectrum for these late, inactive M dwarfs and can be detected in the IR at 4-5μm, 8-11μm, and 16-19μm (see Fig. 3.11). In an atmosphere dominated by N_2O, such strong absorption throughout the IR could obscure the 7.7μm CH_4 feature. It is unknown whether a strong build-up of biotic N_2O would be physically possible around stars with little or no chromospheric flux. Given the existence of a few GALEX stars with little excess chromospheric NUV flux (Shkolnik & Barman 2014) and only an upper limit established for the Ly-α flux from GJ 1214, a small fraction of M dwarfs could exhibit low UV fluxes. However, the MUSCLES data set shows that all six observed M dwarfs have sufficient UV flux to photolyze N_2O and to prevent run-away N_2O build-up.

CH_3Cl contributes to our IR spectrum from 13-14μm in the short wavelength wing of the CO_2 and N_2O features and could also be detectable, depending on the CO_2 and N_2O concentrations present (see Fig. 3.11).

For clear sky models, the vegetation red edge (VRE) surface feature is detectable in low resolution spectra due to the order of magnitude increased VRE reflectance between 0.7μm and 0.75μm for all M grid stars assuming that the exoplanets of these host stars have similar plant life (see Rugheimer et al. 2013, for FGK stars). Clouds partly obscure this feature compared to the clear sky case, although the increase in flux can be seen at 0.7μm in Fig. 3.7 which include Earth-like clouds. Due to the shift in available photons to longer wavelengths for M dwarfs, a different photosynthesis biochemistry could have evolved, resulting in a different but potentially observable vegetation signature (Kiang et al. 2007).

Observability of Spectral Features Note that we have not added noise to these model spectra in order to be useful as input models for a wide variety of instrument simulators for both secondary eclipse and direct detection simulations. Different instrument simulators for JWST (see e.g. Deming et al. 2009; Kaltenegger & Traub 2009) explore the capability of JWST's MIRI and NIRspec instruments to characterize extrasolar

Earth-like planets for near-by as well as luminous host stars. Several groups are providing realistic instrument simulators that can be used to determine the detectability of these absorption features. Future ground and space based telescopes are being designed to characterize exoplanets as small as Earth-like planets and will provide opportunities to observe atmospheric features, especially for Super-Earths with radii up to twice Earth's radius and therefore four times the flux and planet-to-star contrast ratio levels for Earth-size planets as shown in Fig. 3.12.

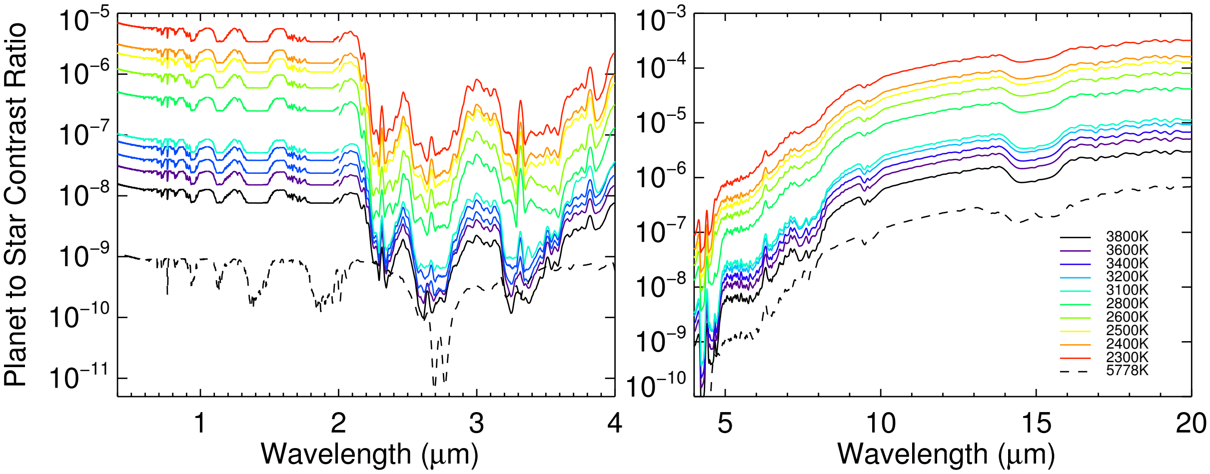

Figure 3.12: Contrast ratios for Earth-like planets orbiting M0-M9 stars in full illumination. Active model contrast ratios are shown here. The contrast ratios of spectral features of planets orbiting inactive M dwarfs have similar levels as active M dwarfs in our models. The black dotted lines show contrast ratios for the Earth orbiting the Sun.

In addition to measuring the size of the planet, future observations will occur at different phases throughout the planet's orbit. The maximum observable planetary flux in the visible spectrum scales with the illuminated fraction of the planet that is visible to the observer. At quadrature, representing an average viewing geometry, the contrast ratios presented in Fig. 3.12 will be a factor of ~ 2 lower in the visible. In the IR, the maximum flux remains constant throughout the planet's orbit, assuming a similar temperature on the planet's day and night side.

3.5 Discussion

Our active and inactive stellar models represent the extreme ends of stellar activity for M dwarfs. AD Leo, our active star proxy with H_α in emission, was chosen to represent a young, active star. Our inactive stellar models assume no chromospheric activity, which is the lowest level possible of UV flux. More observations are needed to determine the lowest possible level of UV flux around an M dwarf, which still might be significantly higher than the photosphere only models. Many M dwarfs exhibit a wide range of activity. Therefore, we use the MUSCLES star database to represent observed M dwarfs with a range of activity between the two extremes. The simulated planets orbiting the MUSCLES stars share more similarities with the planets orbiting the active stellar models particularly in terms of O_3, CH_4, and N_2O concentrations, which is to be expected since they have UV fluxes detectable with HST.

Ly-α is an important line to characterize because it is the strongest line in the FUV part of an M dwarf spectrum. We note that in addition to properly reconstructing the Ly-α line, determining the base level of flux and other emission lines in the FUV and NUV are also important. This is because Ly-α by itself does not significantly impact the photochemistry of an Earth-like planet atmosphere below about 60km unless the Ly-α flux exceeds the highest observed levels observed for the MUSCLES stars (see §3.3 and Fig. 3.6).

Our models are stationary and assume photochemical equilibrium. Young M dwarfs exhibit strong flares which may impact the atmosphere on timescales relevant to the photochemistry. Future work will consider activity induced variability in an exoplanet's atmosphere. See Segura et al. (2010) for models on time-dependent behavior of biosignatures for flaring M dwarfs.

3.6 Conclusions

We show spectral features for terrestrial atmosphere models of Earth-like planets from the VIS to the IR for planets orbiting a grid of M0 to M9 host stars (T_{eff} = 2300K to 3800K) using active stellar models, inactive stellar models, and the sample of M dwarfs with observed UV fluxes. Our grid comprehensively covers the full M stellar range and activity from a proxy of an active flare star, AD Leo, to the lower limit of activity with no chromospheric contribution to the UV.

We discuss the atmospheric model results in §3.3 and the detectable spectral features with a focus on how the UV flux environment affects the emergent spectra in §3.4. Increased UV flux environments in M dwarfs is primarily a property of younger and earlier type stars. Higher UV environments produce: increased concentration of O_3 from photolysis, increased OH from reactions with O_3, decreased stratospheric H_2O, and decreased CH_4, CH_3Cl, and N_2O from photolysis and reactions with OH (see Fig. 3.4). Very inactive M dwarfs may have extremely low UV flux levels as suggested by GALEX observations in the NUV. More observations are needed to determine the lower limit of fluxes in the FUV, in particular the Ly-α emission. Such low levels of UV flux could lead to a build-up molecules such as CH_4 and N_2O in the atmosphere of an Earth-like planet, with N_2O being a strong biosignature due to a lack of photochemical sources.

Terrestrial planets orbiting early M spectral type stars are the best targets for observing biosignatures, such as O_2 or O_3 in combination with a reducing species like CH_4. Note that the O_2 line becomes increasingly difficult to detect for late M dwarfs (see Fig. 3.8). While not observable for an exoplanet around an FGK star, N_2O may be observable at 10.7μm or at 17μm at Earth-level emissions for planets orbiting M dwarfs (see inactive models and model for GJ 832).

Our results provide a grid of atmospheric compositions as well as model spectra from the VIS to the IR for JWST and other future space and ground-based direct imaging and secondary eclipse missions in terms of instrument design and will help to optimize their observation strategy. The model spectra in this paper are available at www.cfa.harvard.edu/∼srugheimer/Mspectra/.

Acknowledgements

We especially thank Andrew West and Evgenya L. Shkolnik for useful conversations about M dwarfs. We also would like to thank Kevin France for discussions concerning the MUSCLES database. This work has made use of the MUSCLES M dwarf UV radiation field database. We would also like to acknowledge support from DFG funding ENP KA 3142/1-1 and the Simons Foundation (290357, Kaltenegger).

The UV radiation field for AD Leo was obtained from the Multimission Archive at the Space Telescope Science Institute (MAST). STScI is operated by the Association of Universities for Research in Astronomy, Inc., under NASA contract NAS5-26555.

Support for MAST for non-HST data is provided by the NASA Office of Space Science via grant NAG5-7584 and by other grants and contracts.

Appendix

GJ 667C: GJ 667C is an M3-4 dwarf at 6.8 pc (van Leeuwen 2007) with an age estimate greater than 2 Gyr (Anglada-Escudé et al. 2013b). GJ 667C has a $T_{\rm eff}$ = 3350K, [Fe/H] = -0.55, and M = $0.330 M_\odot \pm 0.019$ (Anglada-Escudé et al. 2013b). Previous estimates had the effective temperature 350K higher and the spectral designation to be M1.5 due to assuming a higher metallicity (see Geballe et al. 2002; Anglada-Escudé et al. 2013b). We use a radius of R = $0.35 R_\odot$ consistent with the luminosity, L = 0.01370 $L_\odot$ (Anglada-Escudé & Tuomi 2012). We merged a PHOENIX BT-Settl spectrum for $T_{\rm eff}$ = 3350K, [Fe/H] = -0.55, log(g) = 5, and $v \sin i = 3$ km s^{-1} with the MUSCLES UV spectrum at 2800 Å. GJ 667C has less wavelength coverage than the other MUSCLES stars. We approximated the rest of UV radiation field from the FUV and NUV spectral energy distribution of GJ 832, which has a similar spectral type (France et al. 2013), scaled to the distance and Ly-α and Mg II emission line strength of GJ 667C.

GJ 832: GJ 832 is an M dwarf at 4.95 pc (van Leeuwen 2007) with no age estimate and is the least well characterized star in the MUSCLES program sample. It has a $T_{\rm eff}$ = 3620K (NStED value interpolated as described in Bessell 1995), R = $0.48 R_\odot$ (Johnson & Wright 1983), [Fe/H] = -0.12 (Johnson & Apps 2009), and log $g = 4.7$ (Bailey et al. 2008). We merged a PHOENIX BT-Settl spectrum with $T_{\rm eff}$ = 3620K, [Fe/H] = -0.12, log $g = 4.7$, and a $v \sin i = 3$ km s^{-1} with the HST UV spectra from the MUSLES program at 2800 Å.

GJ 1214: GJ 1214 is an M6 dwarf at 14.55± 0.13pc (Anglada-Escudé et al. 2013a) with an age estimate of 6±3 Gyr (Charbonneau et al. 2009). A more accurate parallax measurement increased the previous distance estimate by 10% and thus the luminosity and mass has been shifted from previous values as well (Anglada-Escudé et al. 2013a). With the new parallax and luminosity, GJ 1214 has a radius of 0.211 $R_{\odot}$, T_{eff} = 3250K, M = 0.176 $M_{\odot}$ (Anglada-Escudé et al. 2013a), and [Fe/H] = +0.05 (Anglada-Escudé et al. 2013a; Neves et al. 2012). We used an upper limit of v sin i = 1 km s^{-1} (Browning et al. 2010; Delfosse et al. 1998; Reiners & Basri 2008; West & Basri 2009) and log g = 4.991 (Charbonneau et al. 2009). We merged a PHOENIX BT-Settl spectrum with T_{eff} = 3250K, [Fe/H] = +0.05, log g = 4.991, and v sin i = 1 km s^{-1} with the MUSCLES UV spectrum at 2800 Å. GJ 1214 is the only MUSCLES star to have a non-detection of Ly-α, and thus an upper limit is used and discussed in depth in France et al. (2013).

GJ 436: GJ 436 is an M3 dwarf at 10.1 pc (van Leeuwen 2007) with an age estimate of 6.5-9.9 Gyr (Saffe et al. 2005). GJ 436 has a T_{eff} = 3416K, R = 0.455± 0.018 $R_{\odot}$, and M = 0.507 (+0.071/-0.062) $M_{\odot}$ (von Braun et al. 2012). GJ 436 has solar metallicity, [Fe/H]=0 (Rojas-Ayala et al. 2010), log g = 5.0 (Maness et al. 2007) and a v sin $i < 1$ km s^{-1} (Marcy & Chen 1992). We merged a PHOENIX BT-Settl spectrum with T_{eff} = 3416K, [Fe/H] = 0, log g = 5 and a v sin i = 1 km s^{-1} with the HST UV spectra from the MUSCLES program at 2800 Å.

Gl 581: GJ 581 is a M3 dwarf at 6.2± 0.1pc (van Leeuwen 2007) with age estimate of 7-11 Gyr (Selsis et al. 2007). GJ 581 has a T_{eff} = 3498.0K± 56.0K, R = 0.299 ± 0.010 $R_{\odot}$, and log g = 4.96±0.08 (von Braun et al. 2011). GJ 581 has a metallicity slightly subsolar, [Fe/H] = -0.02 (Rojas-Ayala et al. 2010) and an upper limit on v sin $i \leq 2.1$ km s^{-1} (Delfosse et al. 1998). We merged a PHOENIX BT-Settl spectrum with T_{eff} =

3498K, [Fe/H] = -0.02, log g = 4.96, and v sin i = 2.1 km s^{-1} (Correia et al. 2010) with the MUSCLES UV spectrum at 2800 Å.

GJ 876: GJ 876 is an M dwarf at 4.69pc (van Leeuwen 2007) with an age 0.1-5Gyr (Correia et al. 2010). GJ 876 has T_{eff} = 3129±19K and R = 0.3761 ± 0.0059 $R_{\odot}$ (von Braun et al. 2014). We merged a PHOENIX BT-Settl spectrum with T_{eff} = 3129K, [Fe/H] = +0.19 (Rojas-Ayala et al. 2012), log g = 4.89 (Bean et al. 2006), and v sin i = 1.38 km s^{-1} (Correia et al. 2010) with the MUSCLES UV spectrum at 2800 Å.

Chapter 4

UV Surface Environment of Earth-like Planets Orbiting FGKM Stars Through Geological Evolution

This thesis chapter is in press at ApJ as

S. Rugheimer, A. Segura, L. Kaltenegger, and D. Sasselov.
Accepted to
The Astrophysical Journal on 1 May 2015

Abstract

The UV environment of a host star affects the photochemistry in the atmosphere, and ultimately the surface UV environment for terrestrial planets and therefore the conditions for the origin and evolution of life. We model the surface UV radiation

environment for Earth-sized planets orbiting FGKM stars at the 1AU equivalent distance for Earth through its geological evolution. We explore four different types of atmospheres corresponding to an early Earth atmosphere at 3.9 Gyr ago and three atmospheres covering the rise of oxygen to present day levels at 2.0 Gyr ago, 0.8 Gyr ago and modern Earth (following Kaltenegger et al. 2007). In addition to calculating the UV flux on the surface of the planet, we model the biologically effective irradiance, using DNA damage as a proxy for biological damage. We find that a pre-biotic Earth (3.9 Gyr ago) orbiting an F0V star receives 6 times the biologically effective radiation as around the early Sun and 3520 times the modern Earth-Sun levels. A pre-biotic Earth orbiting GJ 581 (M3.5V) receives 300 times less biologically effective radiation, about 2 times modern Earth-Sun levels. The UV fluxes calculated here provide a grid of model UV environments during the evolution of an Earth-like planet orbiting a range of stars. These models can be used as inputs into photo-biological experiments and for pre-biotic chemistry and early life evolution experiments.

4.1 Introduction

Thousands of extrasolar planets have been found to date with thousands more awaiting confirmation from space and ground-based searches. Several of these planets have been found in or near the circumstellar Habitable Zone (see e.g. Quintana et al. 2014; Borucki et al. 2013; Kaltenegger et al. 2013; Batalha et al. 2013; Borucki et al. 2011; Kaltenegger & Sasselov 2011; Udry et al. 2007) with masses and radii consistent with rocky planet models. The quest for finding habitable planets focuses on main sequence stars with lifetimes conducive for the origin and evolution of life, namely the FGKM spectral types with stellar main sequence lifetimes at least 2 Gyr or more. The UV environment of a host star will affect the atmosphere, and ultimately the surface UV environment for terrestrial planets. (see e.g. Sato et al. 2014; Rugheimer et al. 2015a, 2013; Segura et al. 2003).

Future mission concepts to characterize Earth-like planets are designed to take spectra of extrasolar planets with the ultimate goal of remotely detecting atmospheric signatures that can indicate habitability and life (e.g. Beichman et al. 1999, 2006; Cash 2006; Traub et al. 2006; Kaltenegger et al. 2006; Seager & Bains 2015).The UV surface environment for planets is an important component in providing boundary conditions for biological models exploring the origin of life on Earth as well as planets orbiting other types of stars.

Depending on the intensity, UV radiation can be both useful and harmful to life as we know it. UV radiation from 180 - 300 nm can inhibit photosynthesis and cause damage to DNA and other macromolecule damage (Kerwin & Remmele 2007; Tevini 1993; Matsunaga et al. 1991; Voet et al. 1963). However, these same wavelengths also drive several reactions thought necessary for the origin of life (e.g. Senanayake & Idriss 2006; Barks et al. 2010; Ritson & Sutherland 2012; Patel et al. 2015). In this paper we model the UV surface radiation environments for both pre-biotic and post-biotic planets orbiting other stars at the 1AU equivalent distance based on Earth's evolution.

Previous studies used an analytic atmospheric attenuation model to model UV environment for Archean Earth (Cnossen et al. 2007; Cockell 2000, 1999, 1998) as well as F stars (Sato et al. 2014). An earlier study (Segura et al. 2003) examined the amount of UV radiation reaching the surface of an Earth-like planet with varying oxygen atmospheric concentration orbiting an F2V, G2V (the Sun), and K2V host star. Our paper expands the grid of host stars as well as models of the UV surface environments for atmospheres that correspond to geological epochs throughout Earth's evolution (following Kaltenegger et al. 2007). We focus on four geological epochs corresponding to a 3.9 Ga[1] (assumed prebiotic), 2.0 Ga, 0.8 Ga and the modern Earth atmosphere for a grid of FGKM host stars.

In §4.2, we describe our model, §4.3 presents the calculated UV fluxes at the surface and top of the atmosphere of an Earth-like planet for 12 stellar types and the 4 different atmosphere models through geological time. In §4.4 we conclude by summarizing the results and discussing their implications.

4.2 Model Description

4.2.1 Stellar and Planetary Model

We use a grid of host stars from F0V to M8V (T_{eff} = 7000K to 2400K) (see Rugheimer et al. 2013, 2015a). All stellar models use observations in the UV by the IUE[2] except for 3 M dwarfs with HST data and reconstructed Ly-α fluxes (France et al. 2013) up to 3000 Å combined with PHOENIX (Allard 2014; Allard et al. 2000) or ATLAS (Kurucz 1979) stellar models[3] for larger wavelengths (F0V, F7V, the Sun (G2V), G8V, K2V, K7V,

---

[1] Ga - billion years ago

[2] http://archive.stsci.edu/iue

[3] BT-Settl PHOENIX models are used for the M stars and ATLAS models are used for the FGK stars

M1V, M3V, M8V[4]) The three M dwarfs with updated UV data are, GJ 581 (M3V, $T_{\rm eff}$ = 3498K), GJ 832 (M1.5V, $T_{\rm eff}$ = 3620K), and GJ 1214 (M4.5V, $T_{\rm eff}$ = 3250K) (France et al. 2013).

To model the planetary atmospheres, we use a coupled 1D radiative-convective atmosphere code developed for rocky exoplanets. It iterates between a 1D climate (Kasting & Ackerman 1986; Pavlov et al. 2000; Haqq-Misra et al. 2008) and a 1D photochemistry code (Pavlov & Kasting 2002; Segura et al. 2005, 2007) to calculate the atmosphere transmission of UV fluxes to the ground of Earth-sized planets.

We simulate the effects of stellar radiation on a planetary environment with an altitude range that extends upwards to 60km, corresponding to a pressure of 1mbar, with 100 height layers. A two-stream approximation (see Toon et al. 1989), which includes multiple scattering by atmospheric gases, is used in the visible/near IR to calculate the shortwave fluxes. Four-term, correlated-k coefficients parameterize the absorption by O_3, H_2O, O_2, and CH_4 (Pavlov et al. 2000). Clouds are not explicitly calculated. Clouds can either reduce or enhance UV radiation reaching the surface of an Earth-like planet Grant & Heisler (1997); Parisi & Downs (2004). The climatic effects of clouds on the temperature vs. pressure profile are included by adjusting the planet's surface albedo to the value that for the modern Earth-Sun system yields a surface temperature of 288K (following Kasting et al. 1984; Pavlov et al. 2000; Segura et al. 2003, 2005). The photochemistry code, originally developed by Kasting et al. (1985) solves for 55 chemical species linked by 220 reactions using a reverse-Euler method (see Segura et al. 2010, and references therein).

---

[4] The M1V, M3V and M8V are the active stellar models defined in Rugheimer et al. (2015a).

For the geological epoch at 3.9 Ga, we use a 1D photochemical model for high-CO_2/high-CH_4 terrestrial atmospheres (see Pavlov et al. 2001; Kharecha et al. 2005; Segura et al. 2007, and references therein). This model simulates an anoxic atmosphere composed of 0.9 bar of N_2 and fixed amounts of CO_2 and CH_4. We run the radiative-convective model to convergence and then use the resulting temperature profile to run the photochemical model that contains 73 chemical species involved in 359 reactions. The model spans the region from the planetary surface up to 64 km in 1-km steps. All of the simulated planets at 3.9 Ga are assumed to be devoid of life; hence, none of the compounds in the atmosphere are considered to have a biological source.

4.2.2 Simulation Set-Up

We focus on four geological epochs from Earth's history to model the UV environment on the surface of an Earth-like planet at the 1 AU equivalent distance from its host star. The geological evidence from 2.8 - 3.5 Ga is consistent with an atmosphere with similar atmospheric pressure as modern Earth (Som et al. 2012; Marty et al. 2013). Therefore, we use one bar for the surface pressure for all epochs.

Currently no model can predict the rate of the evolution of life on planets around different stars which themselves have a different main sequence lifetimes. For the Earth-Sun case, we use a solar evolution model for each epoch (Claire et al. 2012). We reduce the stellar flux of all other host stars by the same factor as a first order approximation of how much stellar flux would be received at a corresponding epoch for the other host stars. This procedure is not meant to capture the nuances of stellar evolution. Rather, it is intended to compare across different stellar hosts for planets that receive the same bolometric flux with different atmospheric compositions modeled after Earth's evolution. This translates into different evolutionary stages of the star-planet system as well as into different distances from the the host stars corresponding to 1.15 AU - 1 AU (75-100% current insolation). Especially for M stars, which evolve much more slowly on the main sequence, reducing the stellar flux by the same amount as Earth is equivalent to increasing its distance from the host star. We model each of the four atmospheres for planets orbiting stars with spectral types of F0V, F7V, the Sun (G2V), G8V, K2V, K7V, M1V, M3V, and M8V to sample the FGKM spectral range along with three observed MUSCLES stars, GJ 581, GJ 832, and GJ 1214 with well characterized UV observations from HST.

The first epoch corresponds to a pre-biotic world, similar to early Earth at 3.9 Ga with a CO_2 dominated atmosphere. We model the atmosphere with a fixed surface mixing ratio of $CO_2 = 0.1$ and $CH_4 = 1.65 \times 10^{-6}$ and no biological gas fluxes. We assume a stellar flux of 74.6% of the present day Earth-Sun system.

The next three epochs represent planets with an active biosphere with oxygenic photosynthesis. To model atmospheres corresponding to a similar stage of biological evolution as Earth's, we use calculated biological surface fluxes from the Earth-Sun model as inputs for the same epoch for all other stellar types as detailed in the following three paragraphs.

The second epoch corresponds to 2.0 Ga, when oxygen starts to build up in Earth's atmosphere. We model the atmosphere with a fixed surface mixing ratio of $CO_2 = 0.01$ and $O_2 = 2.1 \times 10^{-3}$ (1% PAL = Present Atmospheric Level) and a stellar flux of 87%. For the Earth-Sun case we fix the mixing ratios of the other biological gases to $CH_4 =$

7.07×10^{-3} (4300x PAL), $N_2O = 8.37 \times 10^{-9}$, $CH_3Cl = 5.0 \times 10^{-10}$ (see Kaltenegger et al. 2007). The corresponding biological surface fluxes required to sustain those mixing ratios are $CH_4 = 1.01 \times 10^{17}$ g yr^{-1}, $N_2O = 3.14 \times 10^{13}$ g yr^{-1}, and $CH_3Cl = 9.06 \times 10^{11}$ g yr^{-1}. All other stellar types except the Sun use these surface fluxes as the boundary conditions for those gases. For H_2 and CO we used fixed deposition velocities of 2.4×10^{-4} and 1.2×10^{-4} cm s^{-1}, respectively, corresponding to the maximum rate of transfer into an ocean (Domagal-Goldman et al. 2014). For the later stellar types, K7V, M1V, M3V and the three observed MUSCLES stars, the CH_4 boundary condition was changed to a fixed mixing ratio (see also Segura et al. 2005; Rugheimer et al. 2015a). For those stellar types, we used a mixing ratio of CH_4 corresponding to the last stable value, calculated for the K2V case, of 4.5×10^{-3}. For the M8V model, we needed to further reduce the CH_4 mixing ratio to 4.0×10^{-3} for a stable atmosphere.

The third epoch corresponds to Earth as oxygen continues to rise at 0.8 Ga and the start of the proliferation of multicellular life. We model the atmosphere with a fixed mixing ratio of $CO_2 = 0.01$ and $O_2 = 2.1 \times 10^{-2}$ (10% PAL) and a stellar flux of 94.8%. For the Earth-Sun case we fix the mixing ratios of the other biological gases to $CH_4 = 1.65 \times 10^{-3}$ (1000x PAL), $N_2O = 9.15 \times 10^{-8}$, $CH_3Cl = 5.0 \times 10^{-10}$ (see Kaltenegger et al. (2007)). The corresponding fluxes used for other stellar types are $CH_4 = 2.75 \times 10^{16}$ g yr^{-1}, $N_2O = 2.08 \times 10^{13}$ g yr^{-1}, and $CH_3Cl = 7.76 \times 10^{11}$ g yr^{-1}. For H_2 and CO we used fixed deposition velocities as above. For the later stellar types, M3V, M8V and the three observed MUSCLES stars, the CH_4 boundary condition was changed to a fixed mixing ratio. We used a mixing ratio of CH_4 corresponding to the last stable value, calculated for the M1V case, of 1.1×10^{-2}.

The fourth epoch corresponds to modern Earth. The model atmosphere has a fixed mixing ratio of CO_2 = 355ppm and O_2 = 0.21. The biogenic fluxes were held fixed in the models in accordance with the fluxes that reproduce the modern mixing ratios in the Earth-Sun case. The surface fluxes for long-lived gases H_2, CH_4, N_2O, CO and CH_3Cl were calculated such that the Earth around the Sun yields a $T_{\mathrm{surf}} = 288$K for surface mixing ratios: $cH_2 = 5.5 \times 10^{-7}$, $cCH_4 = 1.6 \times 10^{-6}$, $cCO_2 = 3.5 \times 10^{-4}$, $cN_2O = 3.0 \times 10^{-7}$, $cCO = 9.0 \times 10^{-8}$, and $cCH_3Cl = 5.0 \times 10^{-10}$ (see Rugheimer et al. 2013). The corresponding surface fluxes are -1.9×10^{12} g H_2 yr^{-1}, 5.3×10^{14} g CH_4 yr^{-1}, 7.9×10^{12} g N_2O yr^{-1}, 1.8×10^{15} g CO yr^{-1}, and 4.3×10^{12} g CH_3Cl yr^{-1}. For the M8V, CH_4 and N_2O were given a fixed mixing ratio of 1.0×10^{-3} and 1.5×10^{-2} respectively (following Rugheimer et al. 2015a).

4.3 Results: UV Fluxes for Planets Orbiting FGKM Stars

For each model atmosphere and star type we calculate the UV flux reaching the surface of an Earth-like planet and compare that to the UV flux incident on the top-of-atmosphere (TOA). In Fig. 4.1 we show the flux of the host star (black lines), the flux at the TOA (gray lines), and the flux reaching the ground for each epoch (colored lines) as seen from an observer at 10 pc. The flux from the host star relative to what is incident on the top of the atmosphere at 500nm ranges from 10^3 to 10^{10} for the M8V to F0V, respectively.

Fig 4.2 compares the incident (dashed) and surface (solid) flux at the planet at each of the four geological epochs for an F0V (T_{eff}=7000K), the Sun (T_{eff}=5778K), a K7V (T_{eff}=4250K), and an M8V star (T_{eff}=2300K) as a representation of the twelve stars

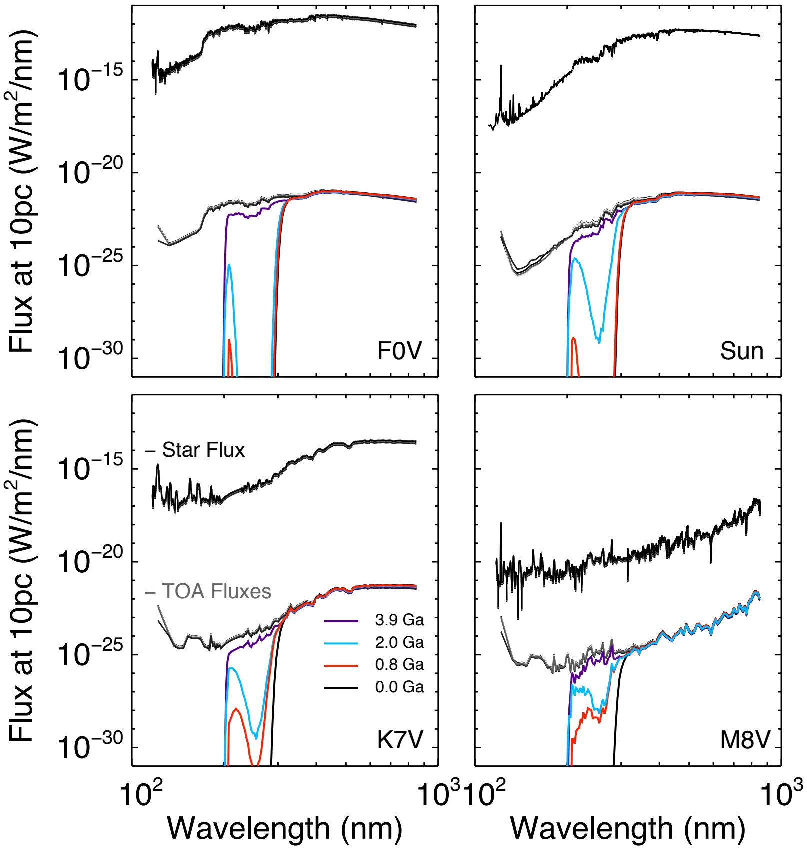

Figure 4.1: The stellar flux (black lines), TOA fluxes (gray lines) and surface UV fluxes (colored lines) for each of the four geological epochs for an F0V (top left), the Sun (top right), a K7V (bottom left) and M8V (bottom right) host star.

modeled. For a pre-biotic atmosphere, the UV surface environment on planets orbiting any of the grid stars follow a similar trend with TOA flux levels being similar to surface flux levels for $\lambda > 200$nm (see top left panel Fig. 4.2). At 200nm there is a sharp absorption in the atmosphere by CO_2 and H_2O and no UV flux at wavelengths below 200nm reaches the surface of the planet for any star type considered. With the rise of oxygen at 2.0 Ga to 1% PAL we see absorption of UV photons around 250nm due to ozone (Fig. 4.2, upper right). This is pronounced for F stars which have ozone column depths an order of magnitude higher at 2.0 Ga than G, K and M stars due to higher incident UV flux and photolysis of O_2 producing O_3 (see Table 4.1 for O_3 column depths for all stars and epochs). As oxygen continues to rise at 0.8 Ga to 10% PAL and then to current levels for the modern Earth, absorption increases for $\lambda < 280$nm due to ozone, effectively blocking UVC radiation from reaching the surface (see also Table A4.3 in the appendix).

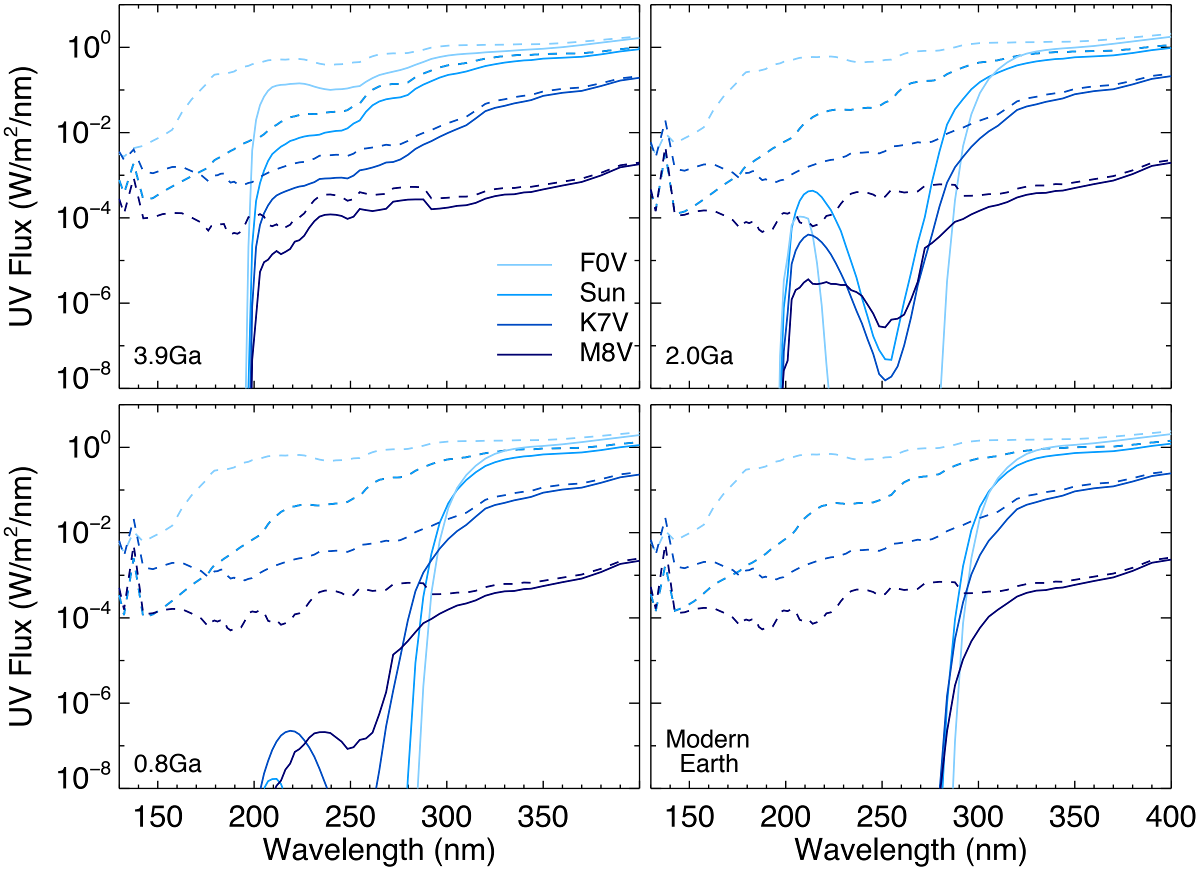

Figure 4.2: The incident stellar UV flux (dashed lines) and the surface UV flux (solid lines) at four geological epochs for a sample of four stellar types spanning the stellar effective temperature range for FGKM stars.

Table 4.2 lists the top-of-atmosphere (TOA) and surface UV fluxes for each stellar

Table 4.1:: Ozone Column Depths for the Grid of Host Stars (F0V to M8V)

	O_3 Column Depth			
Star	3.9 Ga	2.0 Ga	0.8 Ga	Modern Earth
F0V	1.76×10^{16}	5.13×10^{18}	9.07×10^{18}	1.15×10^{19}
F7V	3.93×10^{15}	2.20×10^{18}	6.17×10^{18}	8.62×10^{18}
Sun	1.84×10^{15}	6.01×10^{17}	4.23×10^{18}	5.29×10^{18}
G8V	4.21×10^{14}	1.73×10^{17}	1.62×10^{18}	5.56×10^{18}
K2V	7.32×10^{14}	1.23×10^{17}	1.08×10^{18}	3.62×10^{18}
K7V	1.10×10^{16}	5.31×10^{17}	7.38×10^{17}	3.46×10^{18}
M1V	1.01×10^{16}	5.37×10^{17}	7.37×10^{17}	4.03×10^{18}
M3V	9.88×10^{15}	3.97×10^{17}	5.66×10^{17}	3.59×10^{18}
M8V	1.43×10^{15}	2.63×10^{17}	3.15×10^{17}	2.47×10^{18}
GJ 581	6.76×10^{15}	3.55×10^{17}	4.75×10^{17}	1.18×10^{18}
GJ 832	2.49×10^{15}	3.46×10^{17}	6.25×10^{17}	1.59×10^{18}
GJ 1214	1.91×10^{16}	6.29×10^{17}	9.00×10^{17}	2.31×10^{18}

type and geological era for planets orbiting at the 1AU equivalent distance for their host star. In the appendix tables A1 to A3 show the TOA and surface UV fluxes subdivided into UVA (315-400nm), UVB (280-315nm), and UVC (121.6-280nm). Note that all fluxes have been diurnally averaged and calculated for a zenith angle of 60 degrees, representing a global average. We discuss the F0V-M8V results below and, comparable information for the three MUSCLES stars can be found in the tables.

At 3.9 Ga, 54% - 77% of the total incoming stellar UV flux (121.6nm to 400nm) reaches the surface for a pre-biotic atmosphere orbiting different host stars. The lowest percentage of UV radiation reaches the ground for a pre-biotic Earth orbiting our M8V model star, and the highest percentage of UV radiation reaches the ground a K7V star (this trend holds for all epochs). Note that this does not correspond to the min and max of the absolute transmitted flux. The minimum UV flux that reaches the ground is 0.035 W m^{-2} for an M8V host star and the maximum is 61 W m^{-2} for an F0V host star in this epoch. However, the fraction of UVA, UVB, and UVC fluxes reaching the surface is different. In the UVA region, between 80% (G2V) - 82% (M8V) of the incident flux and between 0.026 W m^{-2} (M8V) and 45 W m^{-2} (F0V) reaches the surface. In the UVB region, between 57% (F0V) and 59 % (K2V) of the incident flux and between 0.0030 W m^{-2} (M8V) and 10 W m^{-2} (F0V) reaches the surface. In the UVC region between 15% (M1V) and 43% (G8V) of the incident flux and between 4.2×10^{-3} W m^{-2} (M8V) and 5.9 W m^{-2} (F0V) reaches the surface. The percentage and absolute flux reaching the ground depends on the interplay between the intensity of incoming UV radiation and the amount of ozone shielding.

At 2.0 Ga, 25% (M8V) - 69% (K7V) of the total incoming stellar UV flux reaches the surface. In absolute flux, the minimum UV flux that reaches the surface is 0.032 W m^{-2} (M8V) and the maximum is 48 W m^{-2} (F0V). In the UVA region, between 73% (Sun) - 78% (K7V) of the incident flux and between 0.029 W m^{-2} (M8V) and 47 W m^{-2} (F0V) reaches the surface for a planet. In the UVB region, between 7.8% (F0V) and 48% (K2V) of the incident flux and between 2.2×10^{-3} W m^{-2} (M8V) and 2.5 W m^{-2} (G8V) reaches the surface. In the UVC region between 2.1×10^{-3} % (F0V) and 2.5% (G8V) of the incident flux and between 1.7×10^{-4} W m^{-2} (M8V) and 5.8×10^{-4} W m^{-2} (F0V) reaches the surface for a planet.

At 0.8 Ga, 26% (M8V) - 69% (K7V) of the total incoming stellar UV flux reaches the surface. In absolute flux, the minimum UV flux that reaches the surface is 0.035 W m^{-2} (M8V) and the maximum is 51 W m^{-2} (F0V). In the UVA region, between 72% (F0V) - 79% (M8V) of the incident flux and between 0.032 W m^{-2} (M8V) and 50 W m^{-2} (F0V) reaches the surface for a planet. In the UVB region, between 4.0% (F0V) and 36% (M8V) of the incident flux and between 2.3×10^{-3} W m^{-2} (M8V) and 1.0 W m^{-2}

(F7V) reaches the surface. In the UVC region between $1.3 \times 10^{-9}\%$ (F0V) and 0.097% (M8V) of the incident flux and between 4.1×10^{-8} W m^{-2} (F0V) and 1.4×10^{-4} W m^{-2} (M3V) reaches the surface for a planet.

For the modern Earth-like atmosphere, 25% (M8V) - 69% (K7V) of the total incoming stellar UV flux reaches the surface. In absolute flux, the minimum UV flux that reaches the surface is 0.034 W m^{-2} (M8V) and the maximum is 53 W m^{-2} (F0V). In the UVA region, between 72% (F0V) - 79% (M8V) of the incident flux and between 0.034 W m^{-2} (M8V) and 53 W m^{-2} (F0V) reaches the surface for a planet. In the UVB region, between 2.7% (F0V) and 17% (K7V) of the incident flux and between 9.9×10^{-4} W m^{-2} (M8V) and 0.80 W m^{-2} (Sun) reaches the surface. In the UVC region between $7.7 \times 10^{-29}\%$ (F0V) and $4.6 \times 10^{-9}\%$ (M8V) of the incident flux and between 2.5×10^{-29} W m^{-2} (F0V) and 4.3×10^{-12} W m^{-2} (M8V) reaches the surface for a planet.

To estimate the biologically relevant UV fluxes, it is useful to consider the damage to DNA and other biomolecules. An action spectrum is a parameter which gives the relative biological response effectiveness at different wavelengths. Multiplying the surface flux by the action spectrum gives the biologically effective irradiance. Integrated for a wavelength interval gives the biochemical effectiveness in that region, E_{eff}:

$$E_{\text{eff}} = \int_{\lambda_1}^{\lambda_2} F_{\text{surf}}(\lambda) S_{\lambda}(\lambda) d\lambda \tag{4.1}$$

where $F_{\text{surf}}(\lambda)$ is the surface flux (W m^{-2} nm^{-1}) and $S_{\lambda}(\lambda)$ is the action spectrum of the biomolecule of interest in relative units. Action spectra are typically normalized at 260 nm or 300 nm and are given in relative units. The damage of such molecules as the thymine dimers and (6-4)photoproducts correspond to DNA damage and have similar action spectra (see Fig. 4.3 and Matsunaga et al. 1991). We use a DNA action spectrum

Table 4.2:: Top-of-Atmosphere (TOA) and Surface UV fluxes for FGKM Stars

	UV fluxes 121.6 to 400 nm (W m^{-2})							
Star	3.9 Ga		2.0 Ga		0.8 Ga		Modern Earth	
Type	TOA	Surface	TOA	Surface	TOA	Surface	TOA	Surface
F0V	98.6	60.8	113.	48.1	123.	51.1	130.	53.3
F7V	62.6	44.2	71.7	39.1	78.1	40.8	82.4	42.5
Sun	37.9	28.1	43.6	27.8	51.4	30.4	55.0	32.3
G8V	31.3	23.4	35.8	23.8	39.0	24.4	41.2	25.0
K2V	16.5	12.6	19.0	13.1	20.7	13.8	21.8	14.2
K7V	4.79	3.71	5.68	3.94	6.19	4.29	6.53	4.50
M1V	2.00	1.22	3.39	1.19	3.69	1.30	3.89	1.36
M3V	0.934	0.510	1.75	0.465	1.91	0.503	2.01	0.533
M8V	0.0646	0.0347	0.125	0.0316	0.136	0.0349	0.144	0.0353
GJ 581	1.57	1.25	2.04	1.35	2.04	1.47	2.15	1.57
GJ 832	2.06	1.61	2.64	1.74	2.87	1.90	3.03	2.02
GJ 1214	0.943	0.722	1.19	0.778	1.19	0.847	1.25	0.902

Note: All fluxes have been diurnally averaged

for 182 nm $< \lambda < 370$ nm based on Cnossen et al. (2007) for $\lambda < 260$ nm and Setlow (1974)[5] for $\lambda > 265$ nm. For comparison to other shortwave action spectra ($\lambda < 300$) we plot the response curves for DNA photoproducts formation (Matsunaga et al. 1991; Yamada & Hieda 1992), DNA plasmid inactivation, mutation and strand-breaks (Wehner & Horneck 1995), and the inactivation of bacterial spores (Munakata et al. 1991) (see Fig. 4.3). The action spectra agree to within an order of magnitude and is shown to 360nm in Fig. 4.3.

We normalized our DNA action spectrum at 260 nm and reference to modern Earth-Sun when quoting the biologically effective irradiance as given in Equation 4.2 to

---

[5] From: www.esrl.noaa.gov/gmd/grad/antuv/docs/version2/descVersion2Database3.html

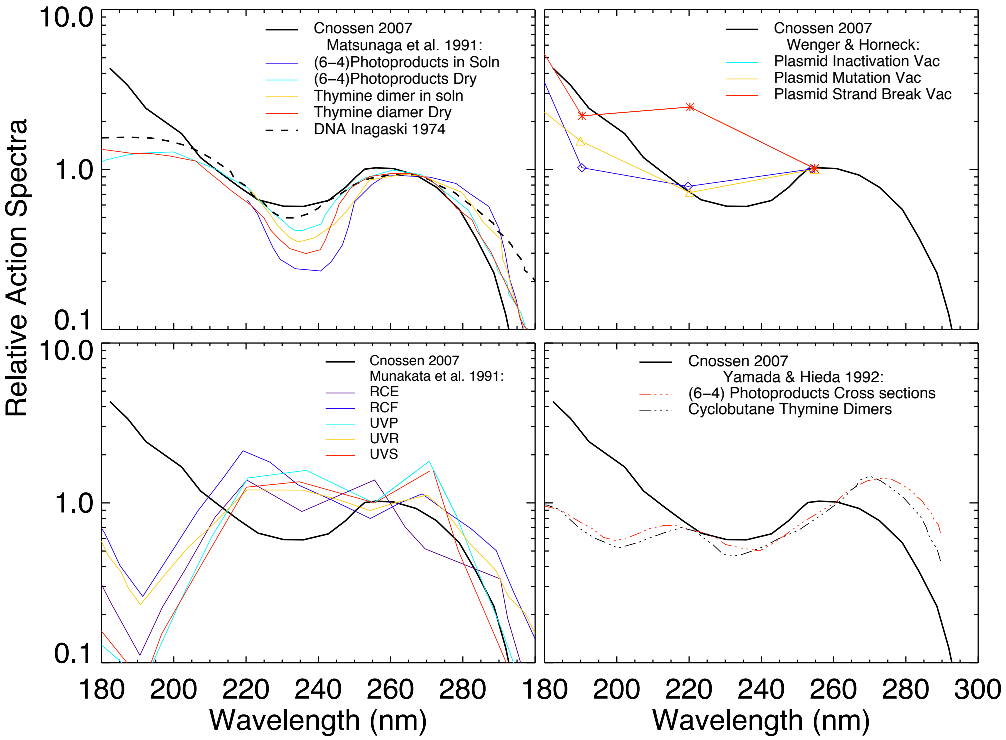

Figure 4.3: Action Spectra for photoproduct formation (top - left, bottom - right), DNA plasmid inactivation, mutation, and strand-breaks (top - right), and the inactivation of bacterial spores (bottom - left).

estimate the damage through geological time.

$$E_{\text{eff}} = \frac{\int_{182\ nm}^{370\ nm} F_{\text{surf}}(\lambda) S_{\lambda\ DNA}(\lambda) d\lambda}{\int_{182\ nm}^{370\ nm} F_{\text{surf modern}\ \oplus}(\lambda) S_{\lambda\ DNA}(\lambda) d\lambda} \tag{4.2}$$

Table 4.3 gives the biologically effective irradiance and the absolute UV flux ratio compared to the modern Earth-Sun model for each geological epoch and stellar type.

Because biological damage is heavily focused in the UVC and UVB regions (shown in Fig. 4.4, the E_{eff} values are much higher for the early Earth case than is intuitive from the absolute fluxes, especially around F-type host stars. For an F0V prebiotic atmosphere, we calculate $E_{\text{eff}} = 3520$, three orders of magnitude larger than for modern

Table 4.3:: Biologically effective irradiance E_{eff}, relative to modern Earth levels

	Fluxes integrated from 182nm to 370nm							
Star	3.9 Ga		2.0 Ga		0.8 Ga		Modern Earth	
Type	E_{eff}	UV Ratio	E_{eff}	UV Ratio	E_{eff}	UV Ratio	E_{eff}	UV Ratio
F0V	3520	2.19	2.75	1.42	0.655	1.47	0.367	1.51
F7V	1680	1.57	10.8	1.23	1.13	1.23	0.524	1.27
Sun	611	0.969	41.3	0.906	1.53	0.942	1.00	1.00
G8V	482	0.806	107	0.797	7.71	0.781	0.678	0.773
K2V	181	0.416	56.5	0.425	5.93	0.433	0.671	0.436
K7V	26.2	0.102	1.95	0.105	1.28	0.114	0.105	0.117
M1V	44.5	0.0345	1.13	0.0301	0.662	0.0327	0.0317	0.0330
M3V	27.8	0.0150	1.26	0.0118	0.644	0.0126	0.0245	0.0126
M8V	2.33	0.00104	0.182	0.000807	0.132	0.000881	0.00393	0.000839
GJ 581	2.02	0.0312	0.432	0.0335	0.345	0.0364	0.120	0.0385
GJ 832	3.37	0.0403	0.616	0.0431	0.353	0.0468	0.105	0.0493
GJ 1214	2.67	0.0176	0.153	0.0186	0.0693	0.0202	0.0180	0.0213

Earth and 6 times larger than the early Earth-Sun model. This E_{eff} value is 1600 times larger than the ratio of UV fluxes at the surface for a prebiotic world orbiting an F0V host star, which highlights the importance of including the action spectrum when considering biological effects. For the anoxic atmosphere at 3.9 Ga, all stars have E_{eff} larger than one, the modern Earth-Sun value. We find the smallest E_{eff} values are about 2 times the modern Earth-Sun value in our model for the surface of a prebiotic planet orbiting GJ 581. It has 31 times less total UV ground radiation and 300 times less biologically effective radiation as the prebiotic Earth-Sun model.

At the rise of oxygen at 2.0 Ga (1% PAL O_2), we see a substantial reduction in E_{eff} values. The surface of planets orbiting F, G, and K grid stars still receive UV radiation corresponding to E_{eff} values higher than modern Earth-Sun, but planets orbiting M stars receive biologically effective irradiances near or less than modern Earth. At 0.8 Ga

(10% PAL O_2), we see further reduction in $E_{\rm eff}$ values. For modern Earth's atmosphere composition, the surface of planets orbiting all other host stars receive UV fluxes that correspond to $E_{\rm eff}$ values less than one. For the F stars, this is due to increased shielding from higher abundances of ozone. For the cooler K and M stars, this is due to a lower abundance of stellar UV photons incident on the atmosphere.

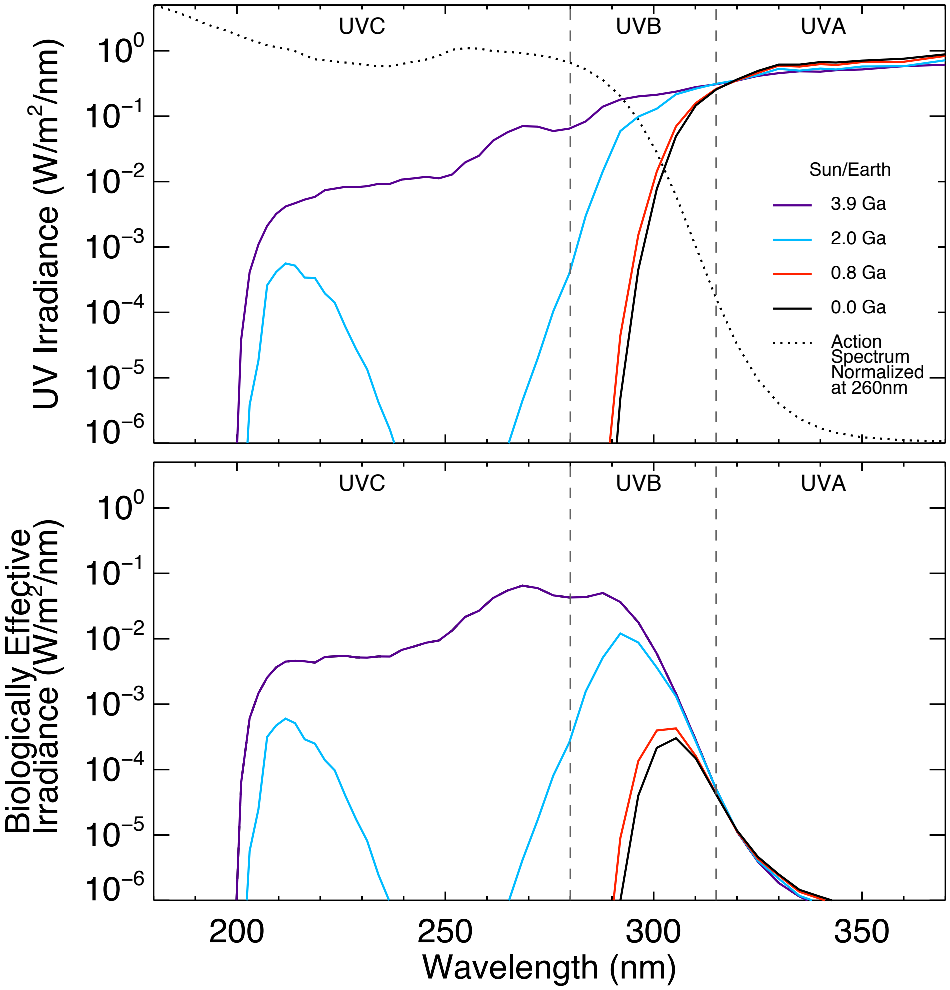

Figure 4.4: UV fluxes at the surface for the Earth-Sun case through time with the dashed line as the DNA Damage Action Spectrum (top). The relative biological effectiveness of UV damage is the convolution of the flux and action spectrum over wavelength (bottom).

In Fig. 4.4 we show the action spectrum (normalized at 260 nm, dashed line) with the Earth-Sun UV surface fluxes through the four geological epochs. Note the strong overlap for the pre-biotic atmosphere. Already at 2.0 Ga most of the UV flux has been attenuated by O_3 in the atmosphere, causing a sharp decrease in the E_{eff} values for the later epochs. The bottom panel of Fig. 4.4 shows the surface UV flux weighted by the DNA action spectrum, highlighting which wavelengths and epochs have the most damaging irradiation for molecules with similar responses as the DNA action curve.

Despite harsh UVB and UVC radiation conditions present on a planet without an ozone shield, certainly prebiotic chemistry and the origin of life flourished on the early Earth. Being under a layer of water or rock would mitigate the problems induced by high UV fluxes. Microbial mats scatter light such that the lower levels have only 1% of incident light at 0.5mm depth, and subsurface community hosting layers of sandstone reduce light levels to 0.005% of incidence (Cockell 1999; Garcia-Pichel et al. 1994; Nienow & Friedmann 1993; Nienow et al. 1988). As well, prebiotic organic polymers and dissolved inorganic ions may provide sufficient protection from UV degradation in as little as 2mm of ocean water (Cleaves & Miller 1998).

Fig. 4.5 shows the smoothed lines for the surface UV flux for an Earth-sized planet at the four geological epochs with the action spectrum curve overlaid for all grid stars modeled.

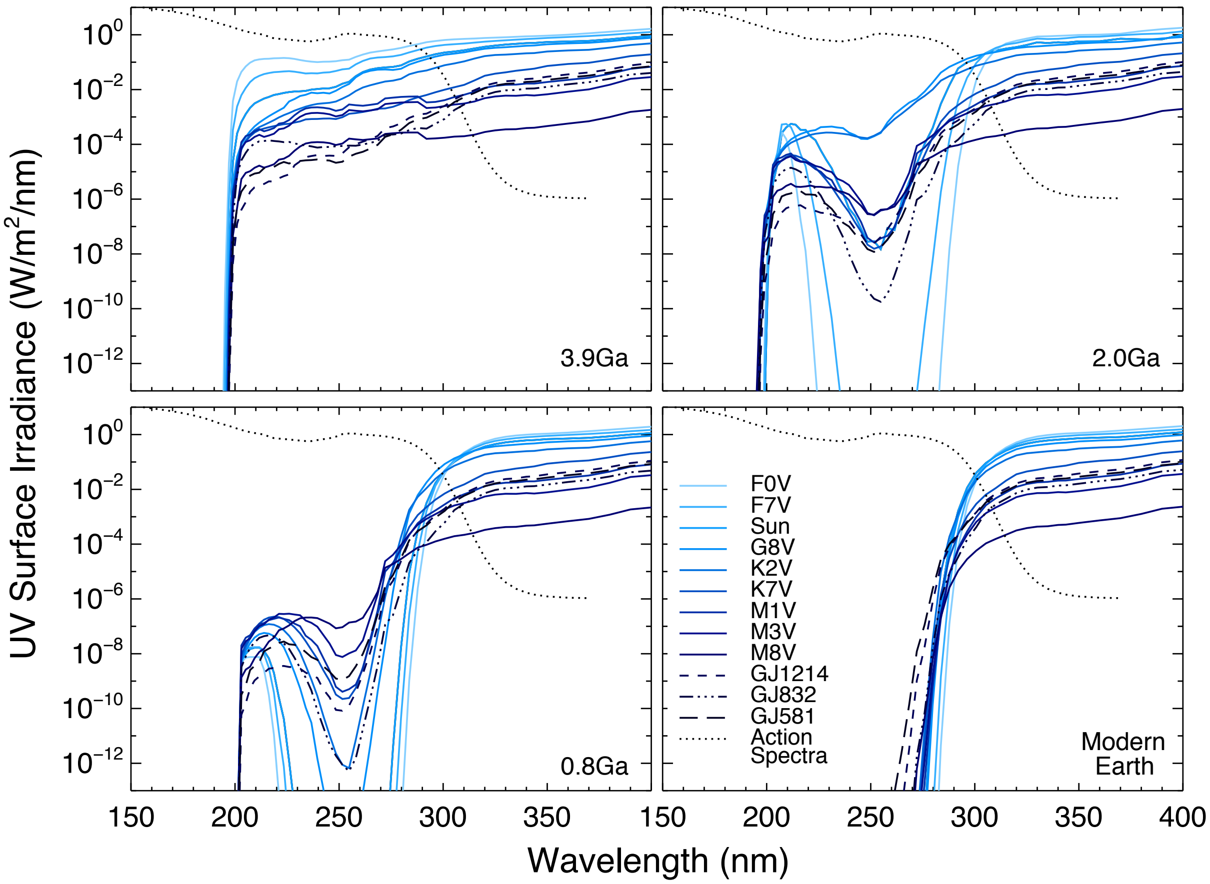

Figure 4.5: Surface UV flux levels (W m^{-2} nm^{-1}) for an Earth-sized planet at four geological epochs orbiting F0V to M8V host stars. Lines have been smoothed for clarity. DNA action spectrum is shown as a dotted line.

4.4 Discussion & Conclusions

In this study, we investigated the exoplanet surface UV fluxes for Earth-like planets orbiting a grid of FGKM stars at four possible biogeological epochs in the evolution of life. We use the input flux from 12 different stellar types, nine model stars in the FGKM range with $T_{\text{eff}} = 4250$K to $T_{\text{eff}} = 7000$K, and three M stars (GJ 581, GJ 832, and GJ 1214) with HST observed UV fluxes for our calculations. The atmospheres selected correspond to a pre-biotic Earth model at 3.9 Ga, a model atmosphere for the early rise of oxygen at 2.0 Ga and 0.8 Ga, and modern Earth biology. In terms of total UV flux at the surface, an F star receives 1-2 times more flux than the Sun, where as an M star receives 20-900 times less flux than the Sun depending on the sub-spectral class.

We also consider the amount of UVA, UVB and UVC fluxes, with the latter two showing the greatest changes among stellar types and geological epochs. For a pre-biotic atmosphere, a significant portion of incident UVC flux reaches the surface. Whereas in the modern atmosphere for planets orbiting any grid star, all UVC photons are effectively shielded by ozone. For all epochs, the smallest percentage of total UV flux compared to incident flux reaching the ground is for an M8V star and the highest fraction is for a K7V star due to the balance of available near- and far-UV photons and the amounts of ozone produced. However in terms of absolute flux, the smallest amount reaches the surface is for an M8V host star and the largest amount for an F0V star.

To analyze the potential biological consequences of the UV surface environment for the origin and evolution of life, we convolve the UV surface fluxes with the DNA action spectrum as a proxy for biological damage. While it is uncertain whether DNA will arise as the primary information carrier on another planet, current biosignature searches are focused on finding carbon-based chemistry. Since the action spectra for other carbon based biomolecules follow similar trends in their actions spectra, we use DNA as a proxy for biochemical effectiveness of UV radiation damage. The surface of pre-biotic worlds have significantly higher E_{eff} values than around the early Sun. *Deinococcus radiodurans* is one of the most radiation tolerant organism known, withstanding 1000x the lethal human radiation dose. UV tolerance experiments show *D. radiodurans* can survive 400 J m^{-2} of 254nm radiation without significant loss of viability with appreciable loss of viability occurring around 500-600 J m^{-2} (Gascón et al. 1995).

We find that a pre-biotic Earth (3.9 Gyr ago) orbiting an F0V star receives 6 times the biologically effective radiation as around the early Sun and 3500 times the modern Earth-Sun levels. A pre-biotic Earth orbiting an M8V star around receives 300 times less biologically effective radiation and 2 times modern Earth-Sun levels.

For the second geological epoch with 1% PAL O_2, a planet orbiting an F0V and M8V star receives 15 and 230 times less biologically effective radiation as the Earth-Sun model at that geological epoch, respectively. For the third geological epoch with 10% PAL O_2, a planet orbiting an F0V and M8V star receives 2 and 12 times less biologically effective radiation as the Earth-Sun model at that geological epoch, respectively. For the fourth geological epoch, corresponding to modern Earth concentrations of O_2, a planet orbiting an F0V and M8V star receives 3 and 250 times less biologically effective radiation as the modern Earth-Sun, respectively. Note that for all epochs after oxygen begins to rise in the atmosphere, both the hottest stars and coolest stars have less biologically effective radiation. For the hottest stars, this is due to increased ozone shielding from higher UV environments, and for the coolest stars this is due to less absolute UV flux.

A layer of water or soil might be needed to shield life for hot stars. Even for a planet orbiting the least UV active star in our grid, the biologically effective irradiance on the surface of a pre-biotic world is several times the value for modern Earth. With higher ozone concentration in the atmosphere, that value decreases for planets orbiting all star types.

We model clear sky atmospheres for all planets at all epochs which on average will represent an upper limit to the UV radiation environment at the surface since clouds most frequently block up to 80% of incoming UV radiation Grant & Heisler (1997); Parisi & Downs (2004). However clouds also can focus more UV radiation to the ground depending on cloud cover and type, increasing the amount of UV radiation reaching the surface. Earth measurements of UVA and UVB radiation on cloudy versus cloud-free days show clouds can enhance UV radiation by a factor of 1.08 and 1.4 for UVA and UVB radiation, respectively (Parisi & Downs 2004).

Note that higher CO_2 and CH_4 concentrations in the atmosphere as well as hazes could further protect the surface from UV radiation (Cnossen et al. 2007; Cockell 1999). In addition, UV photons may also positively contribute to pre-biotic reactions leading to the origin of life (Senanayake & Idriss 2006; Barks et al. 2010; Ritson & Sutherland 2012; Patel et al. 2015).

Our models provide boundary conditions for the UV environment on the surface of Earth-like planets orbiting a grid of FGKM stars from pre-biotic to modern Earth atmosphere. Our results inform photo biological assessments, pre-biotic chemistry, and early life evolution experiments.

Acknowledgements

We would like to thank Kevin France for discussions concerning the MUSCLES database and Sukrit Ranjan for discussions concerning DNA action spectra. This work has made use of the MUSCLES M dwarf UV radiation field database. We would also like to acknowledge support from DFG funding ENP KA 3142/1-1 and the Simons Foundation (290357, Kaltenegger and 290360, Sasselov).

ABBREVIATIONS

Ga - Gyr ago or Billion years ago, TOA - Top of Atmosphere, PAL - Present Atmospheric Level

Appendix

Table A4.1:: Top-of-Atmosphere (TOA) and Surface UVA fluxes for FGKM Stars

	UVA fluxes 315 to 400 nm (W m^{-2})							
Star	3.9 Ga		2.0 Ga		0.8 Ga		Modern Earth	
Type	TOA	Surface	TOA	Surface	TOA	Surface	TOA	Surface
F0V	56.0	44.7	64.1	46.5	69.8	50.2	73.6	52.7
F7V	43.8	34.9	50.2	37.0	54.7	39.8	57.7	41.8
Sun	29.9	23.8	34.4	25.6	40.2	29.5	43.1	31.5
G8V	25.0	19.9	28.6	21.3	31.1	23.0	32.8	24.4
K2V	13.9	11.1	15.9	12.0	17.4	13.0	18.3	13.8
K7V	4.31	3.51	4.94	3.83	5.38	4.18	5.68	4.45
M1V	1.30	1.06	1.49	1.14	1.62	1.25	1.71	1.34
M3V	0.505	0.412	0.578	0.435	0.630	0.475	0.664	0.521
M8V	0.0331	0.0260	0.0379	0.0292	0.0412	0.0324	0.0435	0.0343
GJ 581	1.48	1.21	1.70	1.32	1.85	1.44	1.95	1.54
GJ 832	1.91	1.56	2.19	1.70	2.38	1.86	2.51	1.98
GJ 1214	0.858	0.700	0.983	0.764	1.07	0.832	1.13	0.890

Note: All fluxes have been diurnally averaged

Table A4.2:: Top-of-Atmosphere (TOA) and Surface UVB fluxes for FGKM Stars

	UVB fluxes 280 to 315 nm (W m^{-2})							
Star	3.9 Ga		2.0 Ga		0.8 Ga		Modern Earth	
Type	TOA	Surface	TOA	Surface	TOA	Surface	TOA	Surface
F0V	18.0	10.3	20.6	1.60	22.5	0.905	23.7	0.644
F7V	11.4	6.67	13.1	2.13	14.2	0.998	15.0	0.692
Sun	5.77	3.41	6.76	2.19	8.04	0.902	8.63	0.798
G8V	4.71	2.79	5.39	2.45	5.87	1.31	6.19	0.583
K2V	2.00	1.19	2.29	1.10	2.49	0.714	2.63	0.404
K7V	0.261	0.153	0.145	0.110	0.325	0.108	0.343	0.0566
M1V	0.126	0.0730	0.0844	0.0466	0.158	0.0461	0.266	0.0219
M3V	0.0737	0.0422	0.00590	0.0281	0.0920	0.0275	0.0970	0.0120
M8V	0.00516	0.00298	0.0863	0.00219	0.00643	0.00230	0.00678	0.000986
GJ 581	0.0578	0.0350	0.0721	0.0310	0.0721	0.0321	0.0760	0.0280
GJ 832	0.0754	0.0457	0.0863	0.0399	0.0941	0.0389	0.0992	0.0322
GJ 1214	0.0279	0.0169	0.0319	0.0141	0.0348	0.0143	0.0367	0.0116

Note: All fluxes have been diurnally averaged

Table A4.3:: Top-of-Atmosphere (TOA) and Surface UVC fluxes for FGKM Stars

	UVC fluxes 121.6 to 280 nm (W m^{-2})							
Star	3.9 Ga		2.0 Ga		0.8 Ga		Modern Earth	
Type	TOA	Surface	TOA	Surface	TOA	Surface	TOA	Surface
F0V	24.7	5.89×10^{0}	28.4	5.83×10^{-4}	30.9	4.08×10^{-8}	32.6	2.50×10^{-29}
F7V	7.46	2.64×10^{0}	8.57	2.00×10^{-3}	9.34	9.42×10^{-8}	9.86	1.63×10^{-23}
Sun	2.20	8.71×10^{-1}	2.63	4.03×10^{-3}	3.20	9.31×10^{-8}	3.38	2.30×10^{-16}
G8V	1.59	6.86×10^{-1}	1.84	4.58×10^{-2}	2.01	5.58×10^{-7}	2.12	3.96×10^{-17}
K2V	0.589	2.46×10^{-1}	0.709	3.48×10^{-2}	0.773	7.79×10^{-6}	0.814	4.17×10^{-13}
K7V	0.209	3.99×10^{-2}	0.441	3.88×10^{-4}	0.480	1.39×10^{-5}	0.506	1.14×10^{-13}
M1V	0.549	7.97×10^{-2}	1.73	6.14×10^{-4}	1.88	5.79×10^{-5}	1.99	4.57×10^{-15}
M3V	0.342	4.98×10^{-2}	1.07	8.55×10^{-4}	1.17	1.39×10^{-4}	1.23	3.38×10^{-14}
M8V	0.0254	4.22×10^{-3}	0.0802	1.72×10^{-4}	0.0874	8.49×10^{-5}	0.0921	4.27×10^{-12}
GJ 581	0.0253	2.03×10^{-3}	0.110	6.25×10^{-5}	0.119	1.75×10^{-5}	0.126	6.87×10^{-8}
GJ 832	0.0706	3.77×10^{-3}	0.360	9.99×10^{-5}	0.392	1.01×10^{-5}	0.414	6.08×10^{-9}
GJ 1214	0.0559	4.63×10^{-3}	0.0742	1.00×10^{-4}	0.0808	1.00×10^{-6}	0.0853	1.15×10^{-11}

Note: All fluxes have been diurnally averaged

Chapter 5

Spectra of Earth-like Planets Orbiting Sun-like Stars Through Geological Evolution

This thesis chapter is in preparation for submission to The Astrophysical Journal

S. Rugheimer and L. Kaltenegger

Abstract

Observations of terrestrial exoplanet atmospheres will occur for planets at different stages of geological evolution. We expect to observe a wide variety of atmospheres and planets with alternative evolutionary paths, with some planets resembling Earth at different epochs. For an Earth-like atmospheric time trajectory, we simulate planets from

pre-biotic to current atmosphere based on geological data. We use a grid of host stars from F0V to M8V ($T_{\text{eff}} = 7000$K to 2400K) to model four geological epochs of Earth's history corresponding to a pre-biotic world (3.9 Ga), the rise of oxygen at 2.0 Ga and 0.8 Ga, and the modern Earth. We show the VIS - IR spectral features, with a focus on biosignatures observable through geological time for FGKM stars.

We find that the strongest combination of biosignature gases, O_2/O_3 in combination with a reducing species like CH_4, can be observed together for F stars at 2.0 Ga type atmospheres and for all stars at 0.8 Ga and the modern atmosphere. Our results are a grid of model spectra for atmospheres representative of Earth's geological history to inform future observations and instrument design.

5.1 Introduction

Thousands of extrasolar planets have been found to date, with the radii and masses of dozens of these consistent with rocky planets in or near the circumstellar Habitable Zone (see e.g. Torres et al. 2015; Quintana et al. 2014; Borucki et al. 2013; Kaltenegger et al. 2013; Batalha et al. 2013; Borucki et al. 2011; Kaltenegger & Sasselov 2011; Udry et al. 2007). The occurrence rate for habitable Earth-like planets around M dwarfs is around 18-27% (Dressing & Charbonneau 2015) and around 5-22% around FGK stars (full dataset to determine occurrence for FGK stars is not yet available) (Petigura et al. 2013; Foreman-Mackey et al. 2014), indicating we will likely find a potentially habitable planet within 10 pc around a FGK star, and 3 pc around an M star[1]. TESS, NASA's explorer

---

[1] Based on the RECONS list of nearby stars within 10 pc from www.recons.org

mission scheduled for launch in 2017, is designed to search the whole sky for exoplanets, including potentially habitable planets, around the closest and brightest stars to Earth (Ricker et al. 2014).

Future mission concepts to characterize Earth-like planets are designed to take spectra of extrasolar planets with the ultimate goal of remotely detecting atmospheric signatures (e.g. Beichman et al. 1999, 2006; Cash 2006; Traub et al. 2006; Kaltenegger et al. 2006). For transiting terrestrial planets, the James Web Space Telescope (JWST, see Gardner et al. 2006; Deming et al. 2009; Kaltenegger & Traub 2009) as well as future ground- and space-based telescopes (Snellen et al. 2013; Rodler & López-Morales 2014) will search for biosignatures in rocky planet's atmospheres. Since only a fraction of planets transit, direct imaging will maximize our chances of finding life with technology development currently underway for the Starsade (Exo-S) and the Coronograph (Exo-C) mission concepts (Lawson et al. 2014; Seager 2014), to characterize a planet through emergent visible and infrared spectra.

Undoubtedly, we will encounter a diversity of terrestrial exoplanet atmospheres. Earth's own atmosphere has undergone significant evolution since formation. Previous work from one of the authors examined Earth's spectral features through geological time (Kaltenegger et al. 2007). Here we expand on this work by modeling these planets around an extensive grid of Sun-like stars (F0V - M8V) using a self-consistent climate and photochemistry model and a Solar evolution model (Claire et al. 2012). We focus on four geological epochs corresponding to a 3.9 Ga[2] (prebiotic), 2.0 Ga, 0.8 Ga (the rise of oxygen in Earth's atmosphere), and the modern Earth atmosphere for stars with

---

[2] Ga - billion years ago

main sequence lifetimes longer than 2 billion years, used here as an estimate of the time needed for life to originate and evolve to a complexity that produces oxygen. Note this number is based on our own planet's history and the evolutionary timescales on other planets could differ.

We create a grid of model spectra for atmospheres representative of Earth's geological history to interpret future observations and to inform instrument design. Determining planetary conditions where biosignatures are clear versus ambiguous for different stellar types is a vital step in exoplanet forward modeling.

In §5.2, we describe our model, and §5.3 presents the climate and atmosphere models of an Earth-like planet for 12 stellar types and the 4 different atmosphere models through geological time. In §5.4, we examine the remote observability of spectral features, including biosignatures, and in §5.5 and §5.6, we conclude by summarizing the results and discussing their implications.

5.2 Model Description

5.2.1 Stellar and Planetary Models

We use a grid of host stars from F0V to M8V (T_{eff} = 7000K to 2400K) (see Rugheimer et al. 2013, 2015a). All stellar models use observations up to 3000Å in the UV by IUE[3] except for 3 M dwarfs with new HST data (France et al. 2013) combined with PHOENIX (Allard 2014; Allard et al. 2000) or ATLAS (Kurucz 1979) stellar models for longer

---

[3] http://archive.stsci.edu/iue

wavelengths (F0V, F7V, Sun (G2V), G8V, K2V, K7V, M1V, M3V, and M8V[4]). The three M dwarfs with updated UV data and reconstructed Ly-α are GJ 581 (M3V, $T_{\text{eff}} = 3498\text{K}$), GJ 832 (M1.5V, $T_{\text{eff}} = 3620\text{K}$), and GJ 1214 (M4.5V, $T_{\text{eff}} = 3250\text{K}$) (France et al. 2013).

We use EXO-P (Kaltenegger & Sasselov 2010), a coupled 1D radiative-convective atmosphere code, developed for rocky exoplanets based on a 1D climate code (Kasting & Ackerman 1986; Pavlov et al. 2000; Haqq-Misra et al. 2008), a 1D photochemistry code (Pavlov & Kasting 2002; Segura et al. 2005, 2007), and a 1D radiative transfer model (Traub & Stier 1976; Kaltenegger & Traub 2009) to calculate the model spectrum of an Earth-like exoplanet through geological time orbiting a grid of FGKM host stars.

For the oxygenated epochs at 2.0 Ga, 0.8 Ga and 0.0 Ga (modern Earth), we use a high O_2 photochemical model. Our radiative-convective model simulates both the effects of stellar radiation on a planetary environment and the planet's outgoing spectrum. The dominate contributions to emission spectra from Earth-like planet atmospheres come from the atmosphere below 60km, and so we model our atmospheres to approximately 60km (10^{-4} bar) with 100 layers. The radiative forcing of clouds is included by adjusting the surface albedo of the modern Earth-Sun system (following Kasting et al. 1984; Segura et al. 2003). The photochemistry code solves for 55 chemical species linked by 220 reactions using a reverse-Euler method (see Segura et al. 2010, and references therein).

For the non-oxygenated geological epoch at 3.9 Ga, we use a 1D climate and photochemical model for high-CO_2/high-CH_4 terrestrial atmospheres (see Pavlov et al. 2001; Kharecha et al. 2005; Segura et al. 2007, and references therein). This model

---

[4] The M1V, M3V and M8V are the active stellar models defined in Rugheimer et al. (2015a).

simulates an atmosphere composed of N_2, CO_2, and CH_4. We run the radiative-convective model to convergence and then input the temperature and pressure profiles into a photochemical model with 73 chemical species involved in 359 reactions.

Both the high and low O_2 photochemical models are stationary, and run to chemical equilibrium.

The radiative transfer model used to compute the remotely detectable spectra was developed for exoplanet transmission and direct detection spectra (Kaltenegger et al. 2007; Kaltenegger & Traub 2009; Kaltenegger 2010; Kaltenegger & Sasselov 2010; Kaltenegger et al. 2013). We calculate the spectrum at high spectral resolution with 0.1 cm^{-1} wavenumber steps. The figures are shown smoothed to a resolving power of 150 in the IR (according to JWST mission design) and 800 in the VIS using a triangular smoothing kernel. We previously validated EXO-P from the VIS to the IR using observations of Earth as an exoplanet from EPOXI, Mars Global Surveyor, Shuttle data, and multiple earthshine observations, (Kaltenegger et al. 2007; Kaltenegger & Traub 2009; Rugheimer et al. 2013).

The geophysical community is divided on the rate and formation of continental crust (Arndt 2013). In absence of clear data, for all epochs we assume 70% ocean, 2% coast, and 28% land, the present value for Earth. Before widespread vegetation (all epochs except modern Earth in our model), we adopt land surface compositions of 35% basalt, 40% granite, 15% snow, and 10% sand. For modern Earth we adopt 30% grass, 30% trees, 9% granite, 9% basalt, 15% snow, and 7% sand which includes the vegetation red edge (VRE) (following Kaltenegger et al. 2007). Surface reflectivities are taken from the USGS Digital Spectral Library[5] and the ASTER Spectral Library.[6]

Clouds have a strong impact on the detectability of atmospheric species. In the VIS to NIR, clouds increase the reflectivity of an Earth-like planet, thereby increasing the equivalent width of spectral features, but restrict access to the lower atmosphere. In the IR, clouds slightly decrease the overall emitted flux of an Earth-like planet because they radiate at lower temperatures and can decrease or increase the absorption features. For a comparison of scenarios with Earth-analogue clouds to those of clear sky spectra and their effect on detectability of features see e.g. Rugheimer et al. (2013). We model here Earth-analogue clouds for all epochs comprising a 60% global cloud cover divided between three layers: 40% water clouds at 1km, 40% water clouds at 6km, and 20% ice clouds at 12km (following Kaltenegger et al. 2007) consistent with an averaged Earth profile.

We have not added noise to these model spectra to provide them as input models to a wide variety of instrument simulators for both secondary eclipse and direct detection simulations for JWST's MIRI and NIRspec Instrument, and future missions, to characterize terrestrial extrasolar planets for close-by, luminous host stars.

5.2.2 Simulation Set-Up

We focus on four geological epochs from Earth's history with atmosphere models defined in Rugheimer et al. (2015b) (following Kaltenegger et al. 2007). We use a 1

---

[5] http://speclab.cr.usgs.gov/spectral-lib.html

[6] http://speclib.jpl.nasa.gov

bar atmosphere for all geological epochs modeled since geological evidence is consistent with paleo-pressures near modern values (Som et al. 2012; Marty et al. 2013). For the Earth-Sun case, we use a solar evolution model for each epoch (Claire et al. 2012). We reduce the flux of all stellar types by the same decrease in luminosity Earth received at each geological time in the absence of a self-consistent exobiology evolution model. This procedure is not meant to represent consistent stellar evolution across FGKM stars. Rather, we compare across different stellar hosts for planets that receive the same bolometric flux with different atmospheric compositions modeled after Earth's evolution. Especially for M stars, which evolve much more slowly on the main sequence, reducing the stellar flux by the same amount as in Earth's history is equivalent to increasing the planet's distance from its host star.

Table 5.1:: Surface Mixing Ratios over Geological Time for Earth-Sun

	Initial Mixing Ratios				
Age (Ga)	CO_2	CH_4	O_2	O_3	N_2O
3.9 Ga	1.00E-01	1.65E-06	1.00E-13	2.55E-19	0
2.0 Ga	1.00E-02	1.65E-03	2.10E-03	7.38E-09	8.37E-09
0.8 Ga	1.00E-02	4.15E-04	2.10E-02	2.02E-08	9.15E-08
0.0 Ga	3.55E-04	1.60E-06	2.10E-01	2.41E-08	3.00E-07

The first epoch corresponds to a prebiotic world, similar to early Earth at 3.9 Ga with a CO_2 dominated atmosphere. This atmosphere model has a fixed mixing ratio of $CO_2 = 0.1$ and $CH_4 = 1.65 \times 10^{-6}$. We use an early Sun model at 3.9 Ga from Claire et al. (2012) for the Earth-Sun case and reduce all other stars by a flux factor of 0.746, following the early Sun model.

For the next three oxygenated epochs, we use the biological fluxes from Rugheimer et al. (2015b, 2013) calculated from the Earth-Sun mixing ratios in Table 5.1. Mixing ratios for CH_4 and N_2O are given in Table 5.2 for each epoch for the grid of host stars from F0V to M8V.

The second epoch corresponds to 2.0 Ga, when oxygen started to build up in Earth's atmosphere. We use fixed surface mixing ratios of $CO_2 = 0.01$ and $O_2 = 2.1 \times 10^{-3}$ (1% PAL, present atmospheric level). The biological fluxes for CH_4, N_2O and CH_3Cl are calculated for the Sun-Earth system at 2.0 Ga and then used as input for all other stellar types. For H_2 and CO, we used a fixed deposition velocity of 1.2 x 10^{-4} cm s^{-1} and 2.4 x 10^{-4} cm s^{-1} respectively (following Domagal-Goldman et al. 2014).

The third epoch corresponds to the proliferation of multicellular life on Earth at 0.8 Ga when oxygen had risen to 10% PAL. We use fixed surface mixing ratios of $CO_2 = 0.01$ and $O_2 = 2.1 \times 10^{-2}$. The biological fluxes for CH_4, N_2O and CH_3Cl are calculated for the Sun-Earth system at 0.8 Ga and then used as input for all other stellar types. H_2 and CO were set as in 2.0 Ga.

The fourth geological epoch corresponds to modern Earth (simulations defined in Rugheimer et al. 2013). The model atmosphere has a fixed mixing ratio of CO_2 = 355ppm and $O_2 = 0.21$.

Table 5.2:: Surface Mixing Ratios for CH_4 and N_2O

	Mixing Ratios							
Star	3.9 Ga		2.0 Ga		0.8 Ga		Modern Earth	
Type	CH_4	N_2O	CH_4	N_2O	CH_4	N_2O	CH_4	N_2O
F0V	1.65E-06	-	1.50E-03	5.26E-09	5.65E-04	1.10E-07	3.58E-06	1.63E-07
F7V	1.65E-06	-	1.39E-03	4.54E-09	5.68E-04	1.01E-07	2.46E-06	2.98E-07
Sun	1.65E-06	-	1.83E-03	7.83E-09	4.15E-04	9.15E-08	1.73E-06	3.03E-07
G8V	1.65E-06	-	1.89E-03	2.24E-08	4.60E-04	6.64E-08	4.20E-04	3.08E-07
K2V	1.65E-06	-	4.52E-03	3.29E-08	1.14E-03	8.58E-08	4.53E-04	3.10E-07
K7V	1.65E-06	-	4.50E-03	5.09E-08	1.16E-02	1.60E-07	1.25E-04	8.40E-07
M1V	1.65E-06	-	4.50E-03	4.02E-08	1.13E-02	1.31E-07	3.71E-04	7.04E-07
M3V	1.65E-06	-	4.50E-03	5.84E-08	1.10E-02	1.14E-07	1.45E-04	8.18E-07
M8V	1.65E-06	-	4.00E-03	3.20E-07	1.10E-02	8.46E-07	1.00E-03	3.09E-06
GJ 581	1.65E-06	-	4.50E-03	7.65E-07	1.10E-02	1.81E-06	1.35E-03	4.92E-06
GJ 832	1.65E-06	-	4.50E-03	2.86E-06	1.10E-02	7.18E-06	5.46E-04	1.52E-05
GJ 1214	1.65E-06	-	4.50E-03	1.15E-07	1.10E-02	2.57E-07	1.63E-03	1.10E-06

5.3 Atmospheric Model Results

The temperature vs altitude atmospheric profile and the H_2O, O_3, CH_4 and N_2O mixing ratio profiles for all epochs are shown in the columns of Fig. 5.1. Each row corresponds to one of the four atmospheres modeled: 3.9 Ga, 2.0 Ga, 0.8 Ga and the modern atmosphere (0.0 Ga), respectively, and each color corresponds to one grid star. CH_3Cl profiles are not shown here, but follow the same trends as CH_4. Since both O_2 and CO_2 are well mixed in the atmosphere, their vertical mixing ratio profiles are not shown, but are given in Table 5.1.

In the first column of Fig. 5.1, we show the changes in the temperature/altitude profile for Earth-like atmosphere models around FGKM dwarfs for each of the four epochs. The temperature inversions for the earlier atmospheres are weaker than for modern Earth due to the lower ozone concentrations and thus less heating in the stratosphere. Within each atmosphere, the increased UV flux for hotter stars photolyzes more H_2O and CH_4, causing those stratospheres to be cooler due to less heating from those gases. This trend is reversed in the modern atmosphere where stratospheric heating by O_3 dominates.

H_2O concentrations (Fig. 5.1, 2nd column) in the troposphere are determined by the surface temperature (see Fig. 5.2). H_2O is predominantly formed in the stratosphere by CH_4 (CH_4+OH $\rightarrow$ CH_3+ H_2O), which is present in higher concentrations around cooler stars and by vertical transport from the troposphere in stars where there is little or no temperature inversion. H_2O increases for the middle epochs which have a higher greenhouse gas concentration and a less reduced stellar flux than for the prebiotic model. H_2O in the stratosphere is removed by photolysis or reactions with $O(^1D)$ (reactions

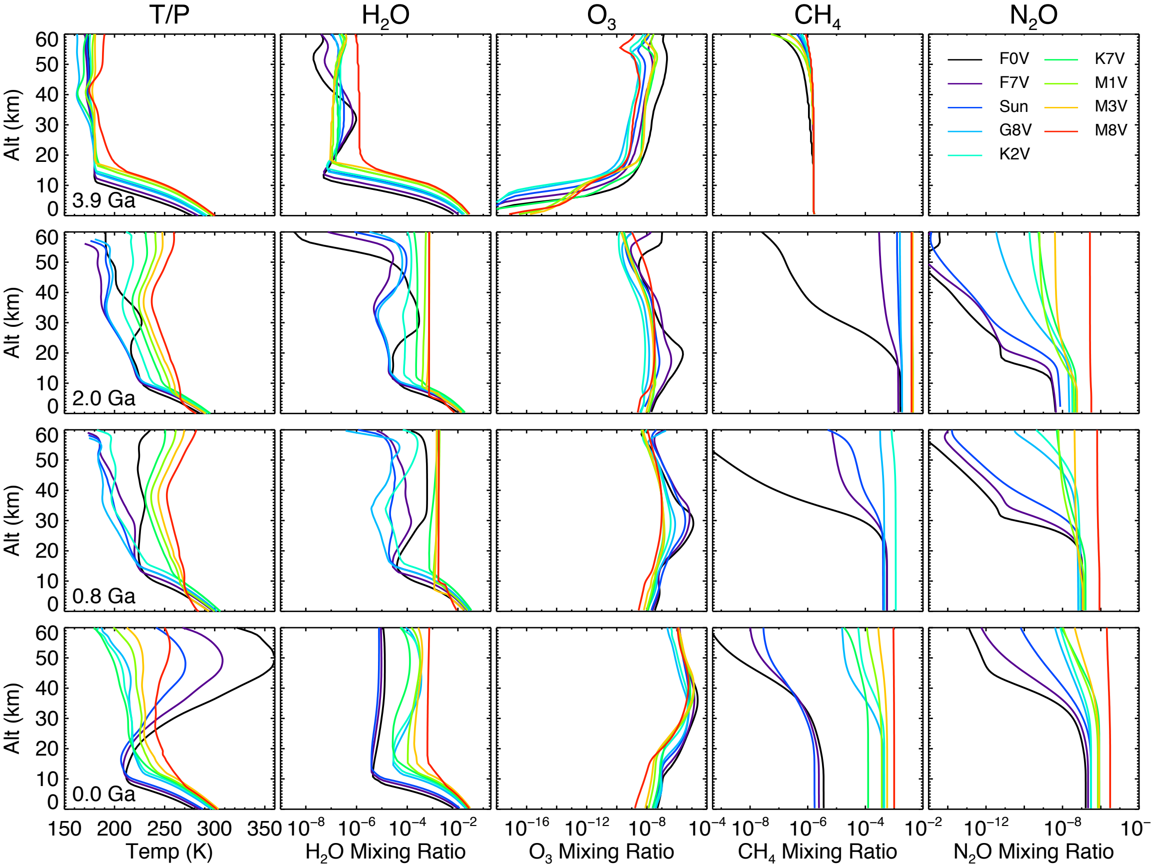

Figure 5.1: Planetary temperature/altitude profiles and mixing ratio profiles profiles for H_2O, O_3, CH_4 and N_2O (left to right) for a planet orbiting the grid of FGKM stellar models with a prebiotic atmosphere corresponding to 3.9 Ga (1st row), the early rise of oxygen at 2.0 Ga (2nd row), the start of multicellular life on Earth at 0.8 Ga (3rd row), and the modern atmosphere (4th row).

R1-R2).

$$H_2O + h\nu \rightarrow H + OH \tag{R1}$$

$$H_2O + O(^1D) \rightarrow OH + OH \tag{R2}$$

Both reactions produce OH and therefore lead to a higher OH concentration in all epochs for hotter stars and an increase with each Epoch as the atmospheres become more oxygenated. Photolysis of H_2O occurs for $\lambda < 2000$Å. For the prebiotic atmosphere there is much more flux at those wavelengths penetrating the atmosphere (see Rugheimer et al. 2015b) and a corresponding decrease in stratospheric H_2O for that epoch.

Ozone is produced primarily by photolysis of O_2 for $\lambda < 2400$Å via the Chapman reactions (reactions R3-R6) (Chapman 1930). Due to photolysis of other species such as CO_2 and H_2O in the prebiotic atmosphere at 3.9 Ga, there is enough free oxygen to form substantial O_3 in the stratosphere, although surface concentrations are up to 10 orders of magnitude lower. Already by 2.0 Ga there is sufficient O_3 for the F stars to create the characteristic ozone bulge in the mixing ratio profile which then increases further for the atmospheres at 0.8 Ga and modern Earth (Fig. 5.1, 3rd column).

$$\mathrm{O_2} + h\nu \rightarrow \mathrm{O} + \mathrm{O}\ (\lambda < 240\ \mathrm{nm}) \tag{R3}$$

$$\mathrm{O} + \mathrm{O_2} + \mathrm{M} \rightarrow \mathrm{O_3} + \mathrm{M} \tag{R4}$$

$$\mathrm{O_3} + h\nu \rightarrow \mathrm{O_2} + \mathrm{O}\ (\lambda < 320\ \mathrm{nm}) \tag{R5}$$

$$\mathrm{O_3} + \mathrm{O} \rightarrow 2\ \mathrm{O_2} \tag{R6}$$

Because O_3 is primarily produced by $\lambda < 2400$Å but destroyed by $\lambda < 3200$ Å, the balance of UV incident flux shortwards and longwards of 2400Å sets the amount of O_3 in the atmosphere (see also Segura et al. 2005; Domagal-Goldman et al. 2011). Hotter stars tend to have more UV continuum flux, which for F, G, and early K stars dominates the shorter wavelengths, $\lambda < 2400$ Å. But for the later K and all M spectral types, relatively little of the overall UV flux is contributed by the continuum (with most in the Ly-α line at 1216 Å). Therefore, the higher UV flux at shorter versus longer wavelengths for K and

M stars creates ozone, as seen in the increase in ozone column densities for the cooler stars.

CH_4 mixing ratio profiles are shown in column 4 of Fig. 5.1. The largest sink for CH_4 in the troposphere and stratosphere is OH. OH concentrations increase as the atmosphere is oxidized. For the prebiotic atmosphere, the high levels of CO_2 and H_2O effectively shield the destruction of CH_4. The biotic surface CH_4 flux in our model is greatest at 2.0 Ga and correspondingly shows the highest CH_4 atmospheric concentrations for the F and G stars. This is due to a larger UV flux ($\lambda < 1500$Å), corresponding to increased CH_4 production from methanogens on Earth at that time and a longer atmospheric lifetime due to lower OH concentrations. For the K and M stars, however, the highest CH_4 concentrations are found for the epoch with the second largest surface CH_4 flux at 0.8 Ga (see also Table 5.2) due to higher stratospheric H_2O abundances from increased stellar luminosity and therefore slightly higher CH_4 concentrations.

N_2O concentrations increase in our models for each oxygenated epoch due to increasing biological flux like on Earth. The destruction of N_2O is driven by photolysis by $\lambda < 2200$ Å and therefore tracks the UV environment of the host star with lower N_2O concentrations around hotter stars. Note that we model no N_2O flux for our prebiotic atmosphere at 3.9 Ga.

The calculated planetary Bond albedo (surface + atmosphere) and surface temperature for each stellar type and geological epoch are shown in Fig. 5.2. The Bond albedo increases for hotter stars due to increased Rayleigh scattering at shorter wavelengths. The surface temperature is affected by a combination of factors. The higher albedos of planets orbiting hotter stars decrease the surface temperature. But also more efficient cooling in the stratosphere lowers the surface temperature.

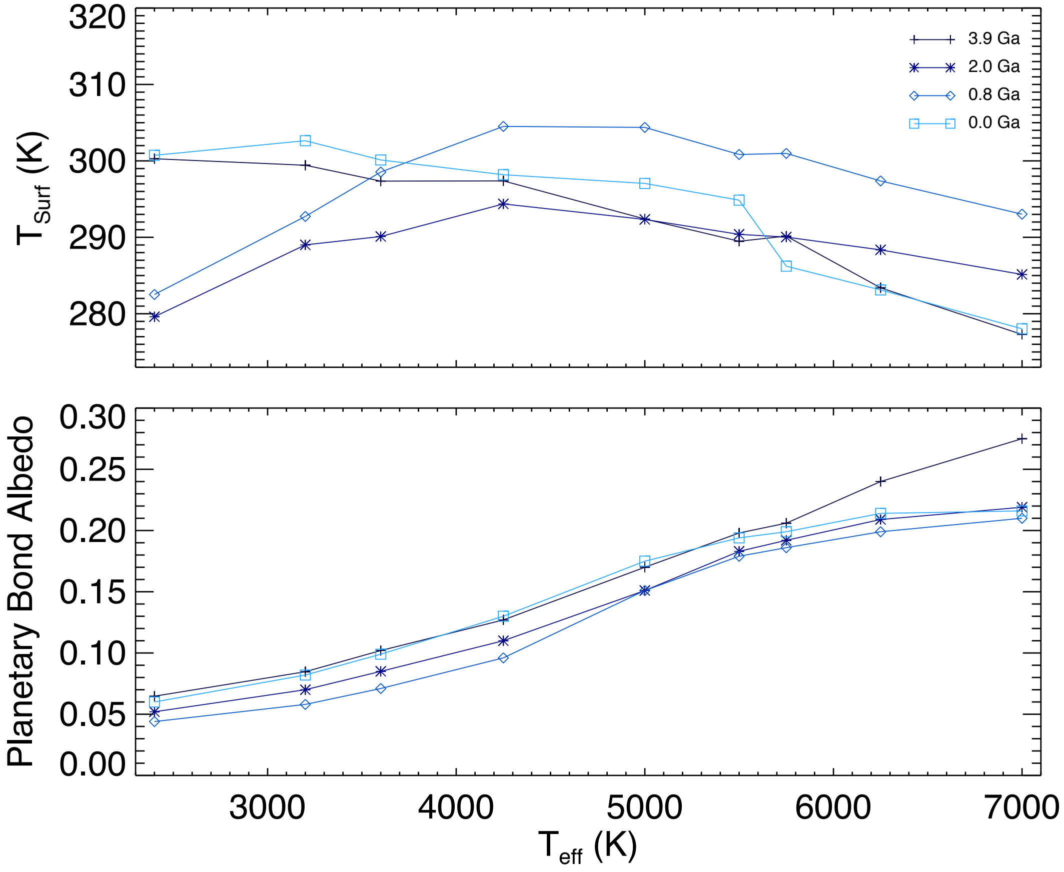

Figure 5.2: Calculated surface temperatures (top) and planetary bond albedos (bottom) for each geological epoch and stellar type.

5.4 Results: Spectra of Earth-Sized Planets Through Geological Time Orbiting FGKM Stars

Spectra of Earth-sized planets orbiting FGKM stars through geological time show measurable differences in spectral feature depths (see also Kaltenegger et al. 2007). We assume full phase for all spectra presented to show the maximum flux that can be observed. No noise has been added to these model spectra to provide input models for a wide variety of instrument simulators for both secondary eclipse and direct detection simulations.

5.4.1 Earth-like Visible/Near-infrared Spectra (0.4μm - 2μm)

Fig. 5.3 shows the reflected visible/near-infrared spectra from 0.4 to 2μm of Earth-like planets orbiting the FGKM grid stars through geological time modeled after Earth's evolution for four epochs. In the VIS, the abundance of the species determines the depth of the absorption features. We present both clear sky and Earth-analogue 60% cloud cover for comparison. Note that no planets with a substantial atmosphere in our Solar System have a cloud free atmosphere. Therefore, cloud-free conditions are used here as optimistic extreme. The high-resolution spectra calculated at 0.1 cm^{-1} steps have been smoothed to a resolving power of 800 to show the individual features clearer.

Fig. 5.3 shows that the host star has a strong influence on the exoplanet's spectrum and detectable features for several reasons: First, due to the increased stellar flux at shorter wavelengths for a G-type star, Rayleigh scattering is much more pronounced for FGK stars than for M stars and therefore greatly increases the flux from 0.4 to 0.8μm for

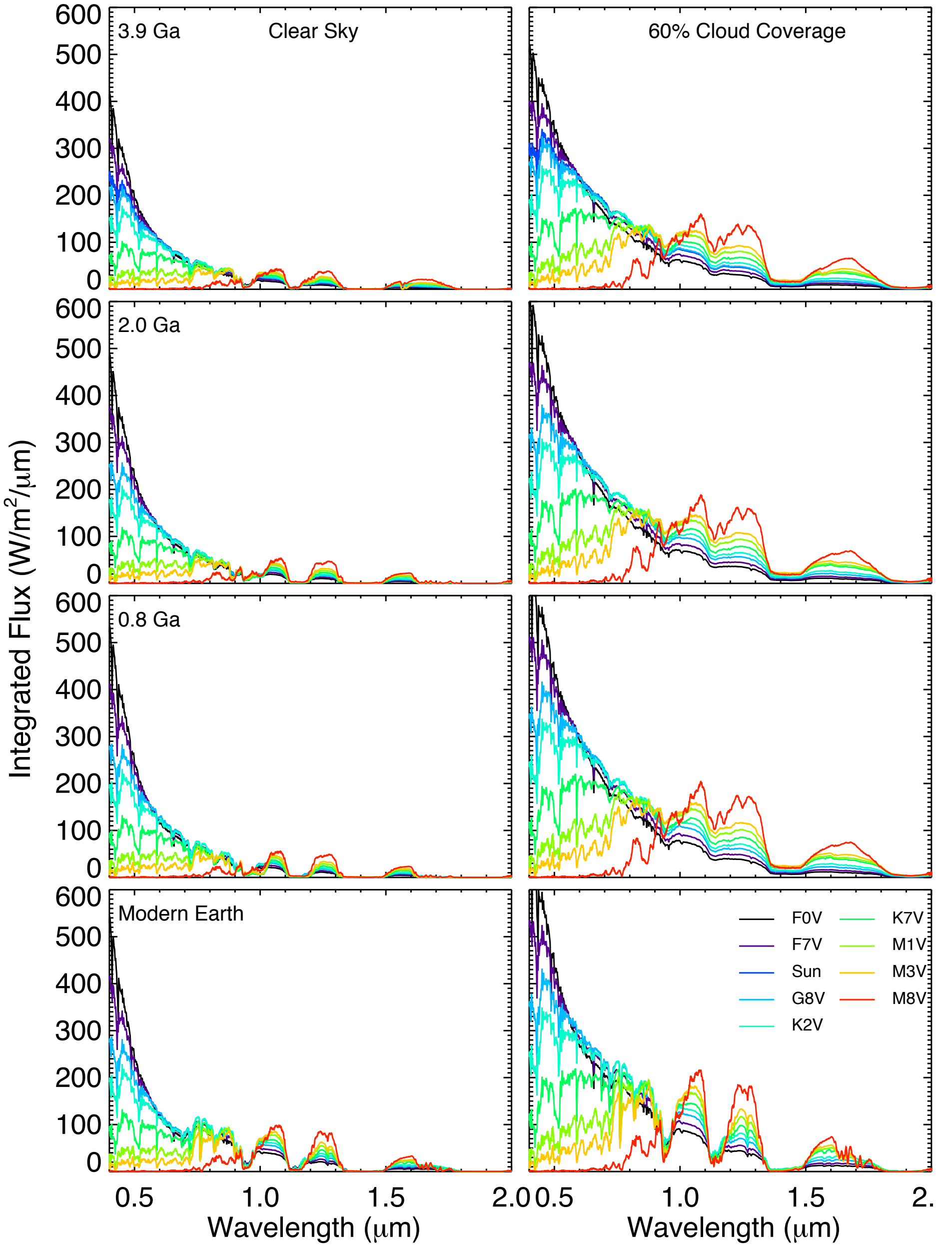

Figure 5.3: Disk-integrated VIS/NIR spectra at a resolution of 800 at the TOA for an Earth-like planet for the grid of stellar and geological epoch models for clear sky (left) and 60% Earth-analogue cloud coverage (right). The region 2-4μm has low integrated flux levels and therefore is not shown here.

an Earth-like planet around a hotter star. Second, late K and M dwarfs have stronger NIR emission and thus the flux from 1-2μm is higher around Earths orbiting M dwarfs than the Earth-Sun equivalent. Note that we scale the stellar luminosity to be the luminosity equivalent the Sun at that geological epoch (as explained in §5.2.2). Thus the earlier epochs have less absolute reflected light flux than the later epochs.

The most notable features in the VIS/NIR spectra (shown in Fig. 5.3) are the broad triangular O_3 feature from 0.45-0.74μm (the Chappuis band), O_2 at 0.76μm, H_2O at 0.95μm, and CH_4 at 0.6, 0.7, 0.8, 0.9, 1.0 and 1.7μm that together can be used as a biosignature (Lederberg 1965; Lovelock 1975; Sagan et al. 1993). Note that any shallow spectral features like the O_3 feature from 0.45-0.74μm would require a very high signal-to-noise ratio (SNR) to be detected in low resolution.

Fig. 5.4 shows details for one of the most notable feature in the VIS, the O_2 band at 0.76μm in both relative absorption (left) and in reflected emergent flux for a 60% cloud cover model stars (right). In the prebiotic atmosphere, no oxygen is present in either the emergent flux or in relative absorption. As oxygen increases, the relative absorption depth similarly increases from 1% (row 2), to 10% (row 3), and finally to 100% (row 4) PAL O_2, yet it isn't until the modern atmosphere that we see a notable increase in the depth of the feature in the remotely detectable spectrum (Fig 5.4, right). We also note that the O_2 feature becomes difficult to detect for the coolest M dwarf in our sample, the M8V, even in the modern atmosphere due to low intrinsic stellar luminosity at those wavelengths (see also Rugheimer et al. 2015a).

Fig. 5.5 displays the individual feature for the Chappuis O_3 feature at 0.6μm. The left panel shows the relative absorption. The O_3 visible feature depth is most

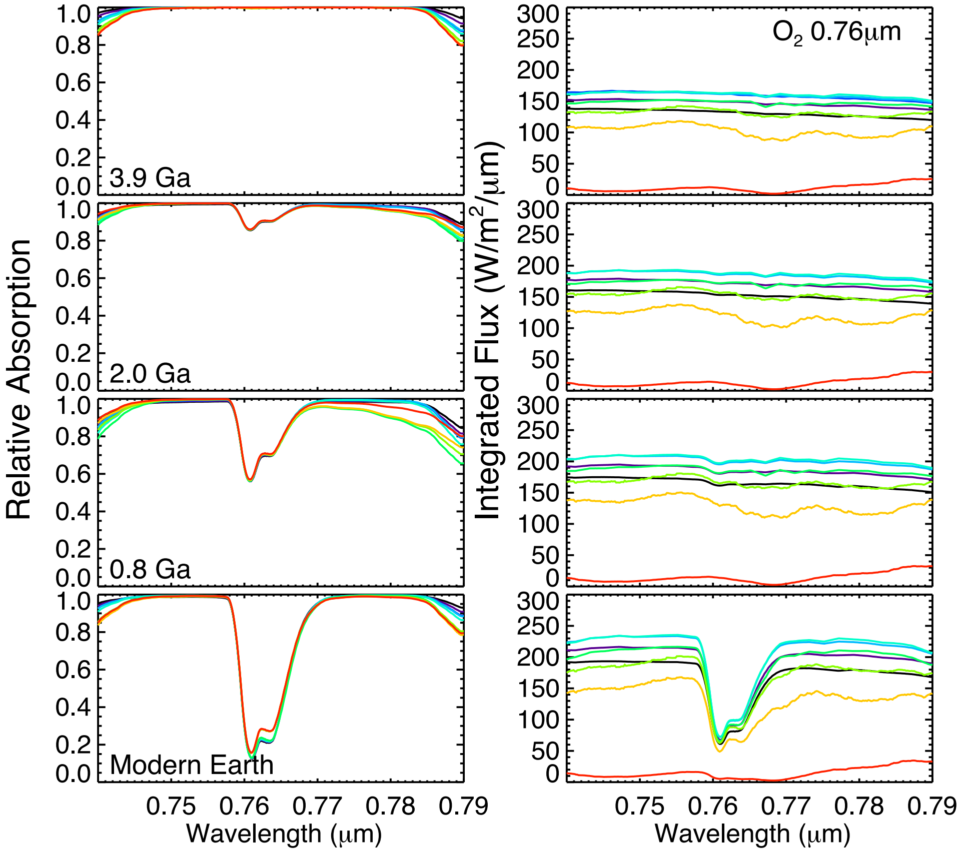

Figure 5.4: O_2 feature at 0.76μm in relative absorption (left) and the detectable reflected emergent flux for a 60% cloud cover (right). Coloring is the same as in Fig. 5.3.

pronounced for the hotter stellar types which have higher UV fluxes and therefore more O_3 production. The feature has a similar absorption depth at 0.8 Ga as in the modern atmosphere for the F and G stars. For the cooler K and M stars, the O_3 feature depth in the visible remains close to the absorption depth of the abiotic levels until the modern Earth atmosphere. The left panels show the effects of the reflected stellar light, surface composition, 60% clouds, and Rayleigh scattering. In low resolution, the direct detection of the broad 0.6 μm O_3 feature in reflected light would require a very high signal to noise to detect even for the highest ozone abundances for all stellar types.

Fig. 5.6 displays the H_2O feature at 0.95μm and CH_4 features at 0.9 and 1.0μm. In relative absorption, the prebiotic atmosphere at 3.9 Ga is most similar to the modern atmosphere in terms of absorption feature depth for H_2O and CH_4. In the direct detection spectra, the CH_4 will require high signal to noise to detect in the VIS/NIR. The surface reflectivity in the pre-vegetation atmospheres (3.9 - 0.8 Ga) also influence the detectability of the features. The H_2O feature shows the deepest absorption features in the modern atmosphere despite having higher abundances at 2.0 Ga and 0.8 Ga.

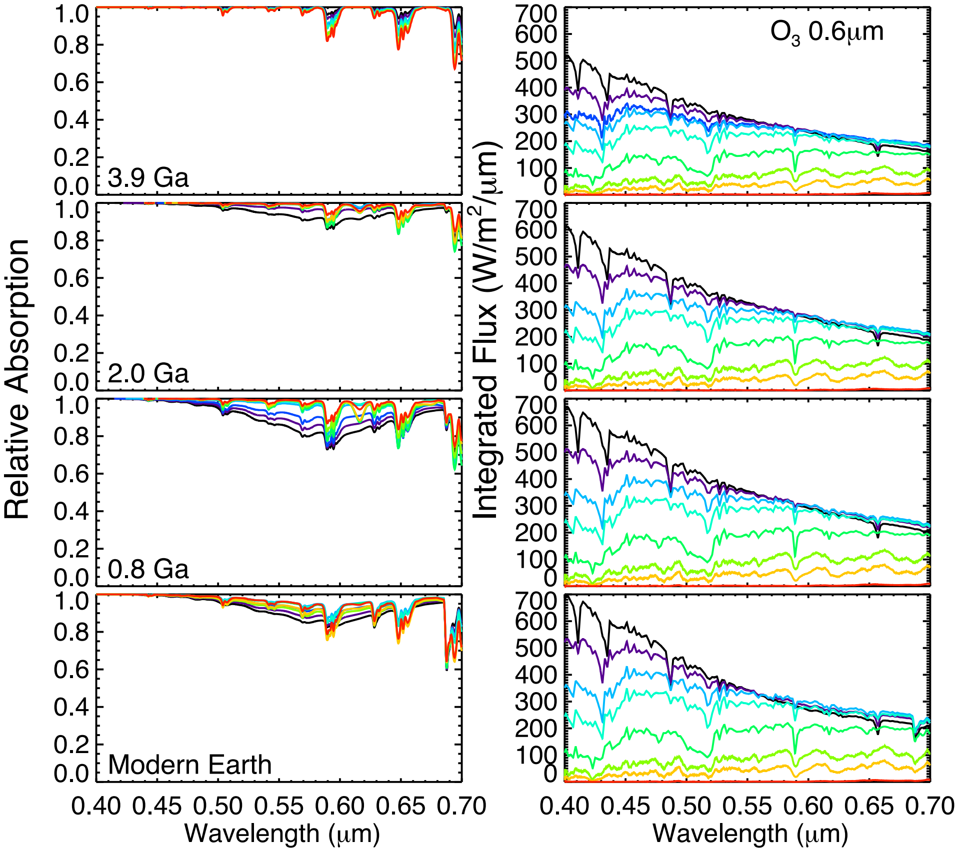

Figure 5.5: Disk Integrated spectra (R = 800) of the O_3 broad Chappuis feature at 0.6μm in relative absorption (left) and in reflected emergent flux for a 60% cloud cover (right). Coloring is same as in Fig. 5.3.

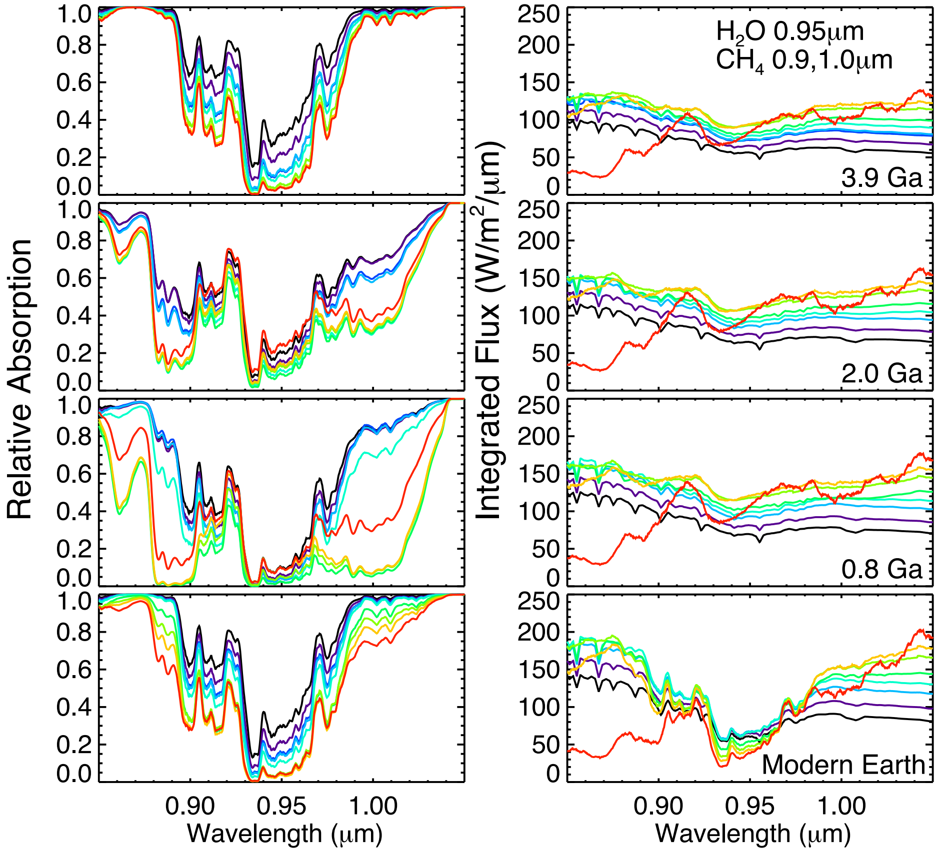

Figure 5.6: Disk Integrated spectra (R = 800) of the H_2O feature at 0.95μm and CH_4 features at 0.9 and 1.0μm in relative absorption (left) and in reflected emergent flux for a 60% cloud cover (right). Coloring is same as in Fig. 5.3.

5.4.2 Earth-like Infrared Spectra (4μm - 20μm)

Fig. 5.7 shows the thermal emission IR spectra from 4 to 20μm of Earth-like planets orbiting the FGKM stars for four geological epochs modeled after Earth's evolution. In the IR, both the concentration and the temperature difference between the continuum and the emitting/absorbing layer influences the depth of absorption features. The emitted flux is higher for the clear sky model since Earth-analogue clouds are cooler thereby partially obscuring the hotter surface. The IR spectra are displayed with a resolving power of 150 according to the proposed resolution of JWST.

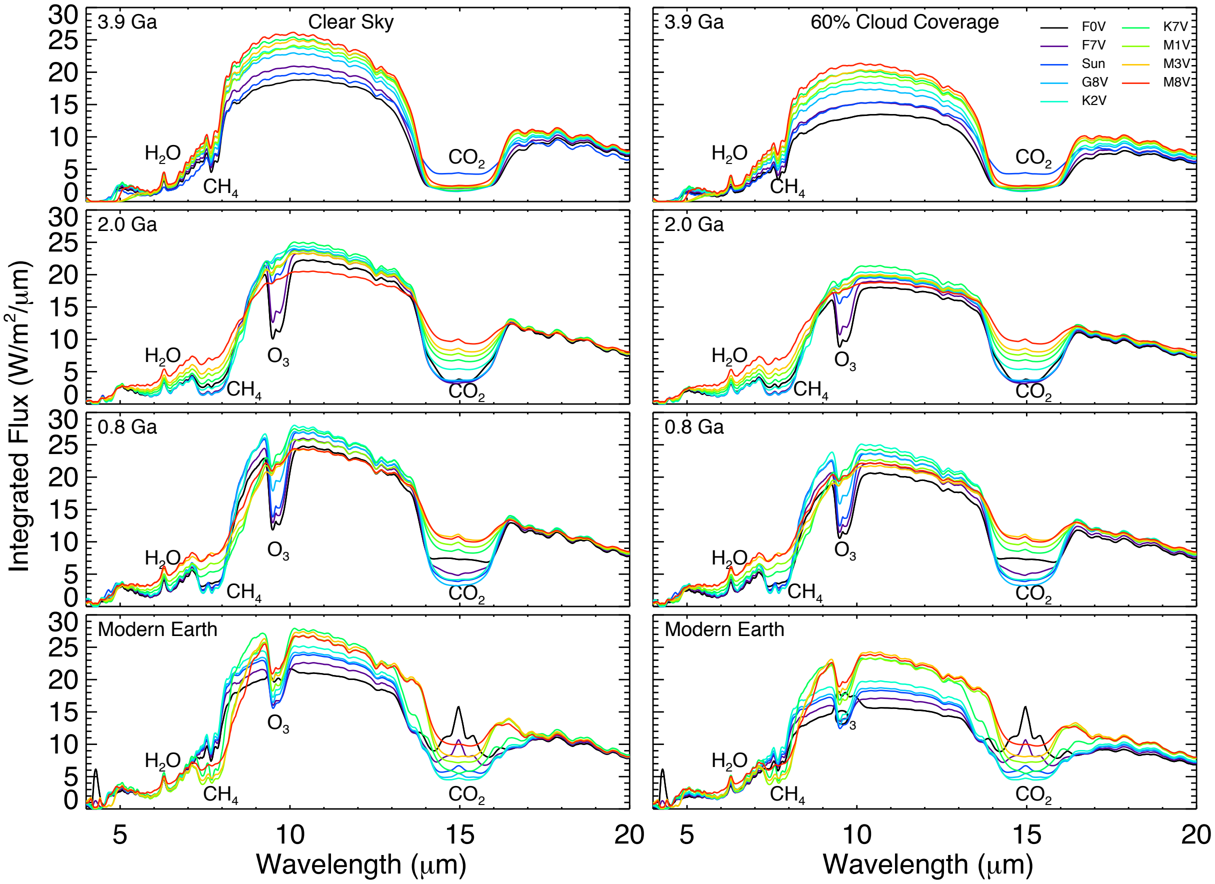

Figure 5.7: Smoothed, disk-integrated IR spectra at the TOA for an Earth-like planet for the grid of stellar and geological epoch models for clear sky (left) and assuming 60% Earth-analogue cloud coverage (right).

The ozone feature at 9.6μm is the feature with the greatest change with host star spectral type and over geological epochs (see also Rugheimer et al. 2013; Kaltenegger et al. 2007). The O_3 feature is shown in Fig. 5.8 in relative absorption and absolute integrated thermal emission flux for 60% cloud cover. At 3.9 Ga, there is not enough abiotic oxygen to produce observable ozone for any stellar type in low resolution spectra. At 2.0 Ga, O_3 is detectable for the two F stars modeled with T_{eff} = 7000K (F0V) and

$T_{\text{eff}} = 6250$K (F7V). At 0.8 Ga when the O_2 levels are at 10% PAL, the O_3 feature is detectable in low resolution spectra for the F and G stars modeled. In the modern atmosphere, the O_3 feature is seen in emission for the hottest F grid star (see also Rugheimer et al. 2013) and is a weaker feature for the other F stars due to the low contrast between the continuum and the hot stratospheres produced by ozone heating.

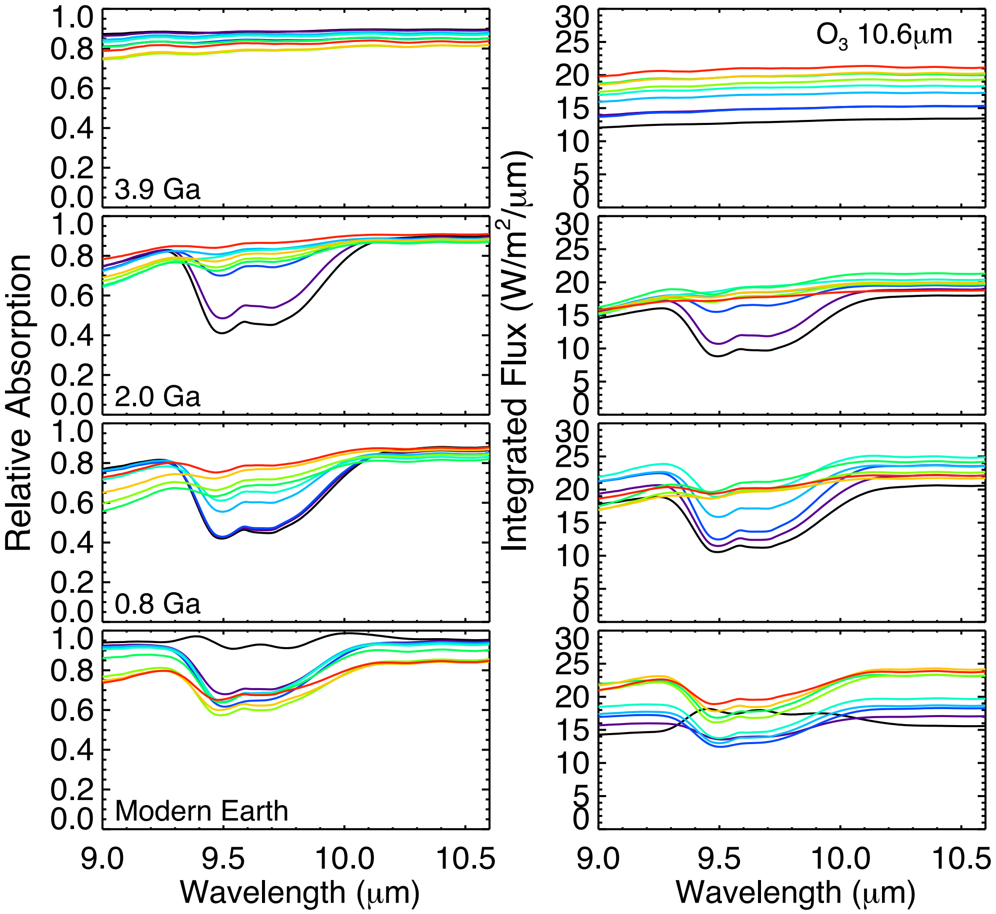

Figure 5.8: Disk integrated (R =150) spectra of the O_3 feature at 9.6μm in relative absorption (left) and in reflected emergent flux for a 60% cloud cover (right). Coloring is same as in Fig. 5.7.

The individual H_2O feature at 5-8μm and CH_4 feature at 7.7μm are shown in relative absorption and reflected emergent flux in Fig. 5.9. The CH_4 feature at 7.7μm increases in depth for epochs with higher methane abundance (2.0 and 0.8 Ga) and the cooler stars. The water feature from 5-8 μm is similar in depth for all epochs and is slightly deeper for hot stars due to a larger temperature difference between the absorbing layer and the continuum.

The individual CO_2 feature at 15μm is shown in relative absorption and reflected emergent flux in Fig. 5.10. The central plateau observed in the modern Earth-like atmospheres for G and F type stars is due to the hot stratospheres of those stars caused by ozone and as such has been taken as an "indirect" ozone feature (see e.g. Selsis 2000). We observe no central plateau until ozone concentrations rise to modern Earth levels (see also Kaltenegger et al. 2007). The CO_2 mixing ratio is fixed for each epoch, but the CO_2 feature is deepest for the hotter stars in our grid due to the difference in the continuum temperature to the CO_2 absorption layer temperature (see Fig. 5.1 for T/P profiles of the atmospheres).

5.5 Discussion

Observations of terrestrial exoplanet atmospheres will occur for planets at different stages of geological evolution. We expect to observe a wide variety of atmospheres and planets with diverse evolutionary paths and some planets resembling Earth at different epochs. For an Earth-like atmospheric trajectory, we can simulate planets from pre-biotic to current atmosphere based on geological data and compare those to detected exoplanet spectra of planets. An exoplanet's mass could potentially be constrained from transmission spectroscopy alone (de Wit & Seager 2013).

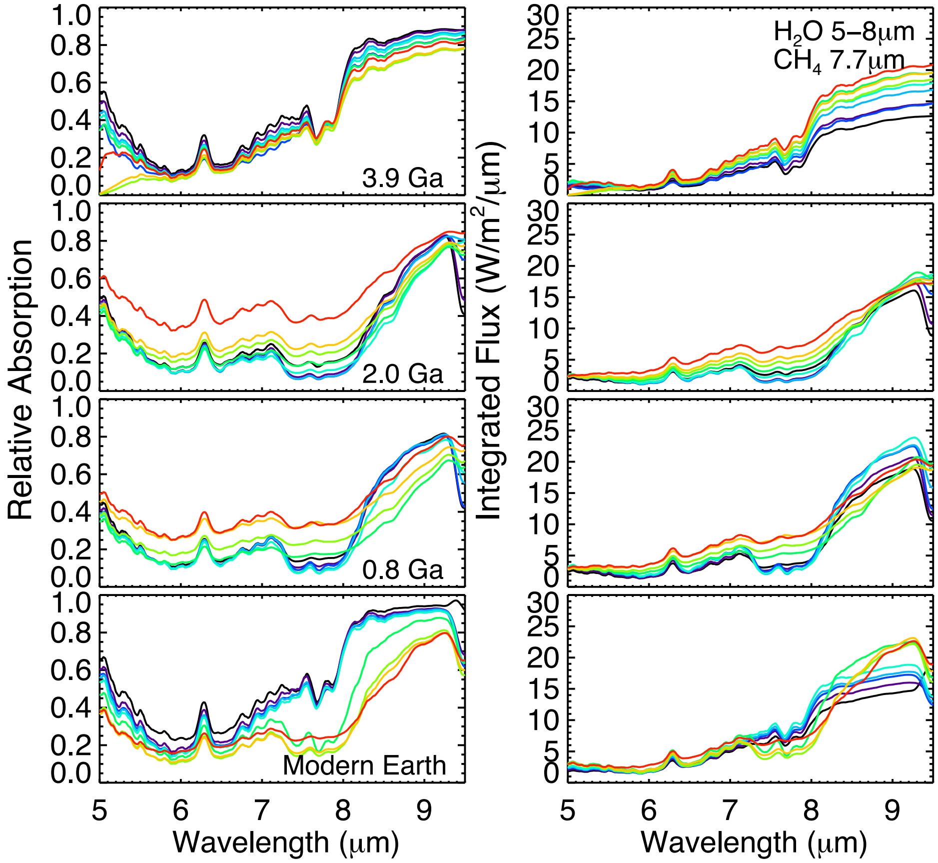

Figure 5.9: Disk integrated (R =150) spectra of H_2O at 5-8μm and the CH_4 feature at 7.7μm in relative absorption (left) and in reflected emergent flux for a 60% cloud cover (right). Coloring is same as in Fig. 5.7.

Detecting the combination of an oxidizing gas and a reducing gas for emergent spectra and secondary eclipse measurements remains the strongest spectroscopic biosignature (Lederberg 1965; Lovelock 1975; Sagan et al. 1993). Detecting the combination of biosignatures in context of a position in the Habitable Zone will aid in reducing the probability of false positive biosignatures. For example, high CO_2 atmospheres around M dwarfs could produce detectable O_2 concentrations from the photolysis of CO_2 or H_2O in low reducing atmospheres (see e.g. Domagal-Goldman et al.

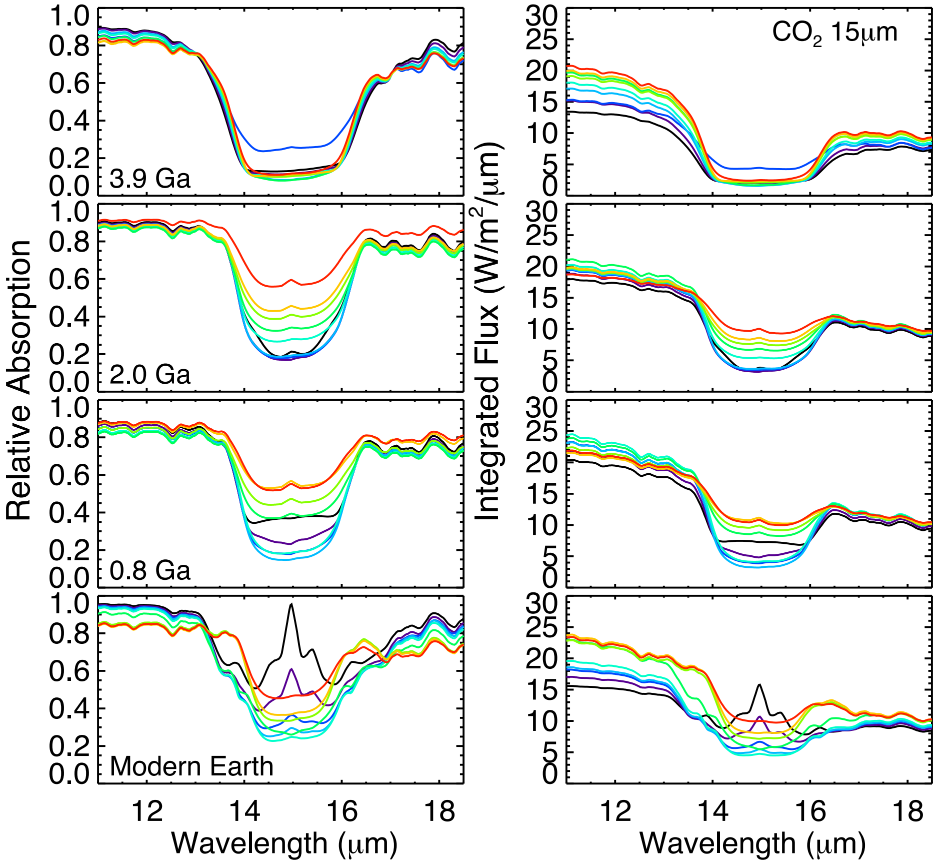

Figure 5.10: Disk integrated (R =150) spectra of the CO_2 feature at 15μm in relative absorption (left) and in reflected emergent flux for a 60% cloud cover (right). Coloring is same as in Fig. 5.7.

2014; Tian et al. 2014; Wordsworth & Pierrehumbert 2014) reinforcing the result that individual spectral features should not be used as a biosignature alone.

In the VIS to NIR, the most accessible biosignatures are the O_2 feature at 0.76μm and one of the multiple CH_4 features between 0.6 - 2.4μm. The H_2O features in the VIS/NIR would provide valuable planetary context of habitability. Detecting the O_3 feature at 0.4μm will require very high signal to noise observations. While visible in relative absorption at the rise of oxygen from 2.0 Ga to 0.8 Ga, the O_2 feature doesn't contribute substantial opacity to the directly detectable spectrum until modern Earth concentrations. For late M dwarves, M7V-M9V, the feature is not detectable due to the low level of stellar reflected flux at that wavelength (see also Rugheimer et al. 2015a). The CH_4 feature is deepest for cooler stars and epochs 2.0 and 0.8 Ga, but it may also be detectable at modern Earth level concentrations which occur for all epochs and stars modeled.

In the IR, the most accessible biosignatures are the O_3 feature at 9.6μm and the CH_4 feature at 7.7μm. The H_2O feature at 5-8μm and the CO_2 feature at 15μm would provide planetary context of habitable conditions. The central plateau of the CO_2 feature indicates a temperature inversion and the presence of an absorbing molecule in the stratosphere such as O_3. The O_3 feature at 9.6μm has a non-linear dependence on O_2 concentration. We find that for a F0V, G2V, K7V, and M8V host stars the ozone column depth is 2.2, 8.8, 6.5, 9.4 times smaller than for the atmosphere with 1% PAL O_2 compared to the modern atmosphere, respectively (see Table 4.1 in chapter 4). For F stars, the O_3 feature is deepest at 2.0 Ga and 0.8 Ga, since the stratospheres are not warm enough to reduce the temperature difference between where ozone absorbs and the surface. For the modern atmosphere, the O_3 feature is in emission for the hottest F stars and is weakest at the transition from absorption to emission near $T_{\mathrm{eff}} = 6250$K. At 0.8 Ga the O_3 feature is detectable for G and K stars. In the modern atmosphere, the O_3 feature is strongest for K stars stars due to an interplay of high enough UV to create O_3 and a larger temperature difference between the stratosphere and the surface.

For all epochs and stellar types modeled, concentrations N_2O and CH_3Cl do not contribute substantially to the emitted spectrum and would likely be undetectable by the first low resolution and photon limited exoplanet atmosphere characterization missions (see e.g. Selsis 2000; Kaltenegger et al. 2007).

5.6 Conclusions

Our results provide a grid of atmospheric compositions as well as model spectra from the VIS to the IR for possible atmospheres from pre-biotic conditions to the modern Earth atmosphere for terrestrial planets at different geological epochs for a grid of F0V-M8V stars. These spectra can be useful input to design instruments and to optimize observation strategy for JWST and E-ELT as well as other future space- and ground-based direct imaging and secondary eclipse mission design concepts such as HDST.

We show the VIS - IR spectral features for terrestrial atmospheres of planets orbiting F0V-M8V ($T_{\rm eff}$ = 7000K to 2400K) for four geological epochs modeled after Earth's evolution. Our earliest geological epoch corresponds to a pre-biotic world. The epochs at 2.0Ga and 0.8Ga represent worlds with increasing oxygen levels, and the fourth epoch corresponds to modern Earth.

For low resolution spectra (R=800 in the VIS/NIR see Fig. 5.4), O_2 does not substantially contribute the detectable emergent spectrum for Earth-analogue cloud coverage until PAL O_2 levels and even in modern Earth-like atmospheres, decreases in depth for later M stars. Thus, the IR is the best spectral region for observing biosignatures at equivalent stages of planetary evolution as Earth for other stars, i.e. O_2/O_3 in combination with a reducing species like CH_4. O_3 and CH_4 can be observed in combination for F stars at 2.0 Ga type atmospheres and for all stars at 0.8 Ga and the modern atmosphere. The CO_2 plateau provides a diagnostic to determine the presence of an inversion layer in the IR.

Earth-like planets have monotonically increasing planetary albedos with increasing stellar temperature for all grid stars through geological time epochs due to increased Rayleigh scattering. Exoplanet surface temperature varies more complexly with stellar temperature due to efficiency in stratospheric cooling and the column densities of chemical species and available stellar radiation.

The model spectra are available at www.cfa.harvard.edu/~srugheimer/EPOCHspectra/

Acknowledgements

This work has made use of the MUSCLES M dwarf UV radiation field database. We would also like to acknowledge support from the Simons Foundation (290357, Kaltenegger).

References

Abe, Y., Abe-Ouchi, A., Sleep, N. H., & Zahnle, K. J. 2011, Astrobiology, 11, 443

Allard, F. 2014, Proceedings of the International Astronomical Union, 8, 271

Allard, F., Hauschildt, P. H., & Schwenke, D. 2000, The Astrophysical Journal, 540, 1005

Anglada-Escudé, G., Rojas-Ayala, B., Boss, A. P., Weinberger, A. J., & Lloyd, J. P. 2013a, A&A, 551, A48

Anglada-Escudé, G., & Tuomi, M. 2012, A&A, 548, A58

Anglada-Escudé, G., et al. 2013b, A&A, 556, A126

Arndt, N. T. 2013, Geochemical Perspectives, 2, 471

Bailey, J., Butler, R. P., Tinney, C. G., Jones, H. R. A., O'Toole, S., Carter, B. D., & Marcy, G. W. 2008, ApJ, 690, 743

Barks, H. L., Buckley, R., Grieves, G. A., Di Mauro, E., Hud, N. V., & Orlando, T. M. 2010, ChemBioChem, 11, 1240

Batalha, N. M., et al. 2013, ApJS, 204, 24

Bates, D. R., & Nicolet, M. 1950, Journal of Geophysical Research, 55, 301

Bean, J. L., Benedict, G. F., & Endl, M. 2006, ApJL, 653, L65

Beichman, C., Lawson, P., Lay, O., Ahmed, A., Unwin, S., & Johnston, K. 2006, in Society of Photo-Optical Instrumentation Engineers (SPIE) Conference Series, Vol. 6268, Society of Photo-Optical Instrumentation Engineers (SPIE) Conference Series, 62680S

Beichman, C. A., Woolf, N. J., & Lindensmith, C. A. 1999, The Terrestrial Planet Finder (TPF) : a NASA Origins Program to search for habitable planets (Pasadena, CA: JPL Publications)

Berner, R. A. 1999, Proceedings of the National Academy of Sciences, 96, 10955

Berta, Z. K., et al. 2012, ApJ, 747, 35

Berta-Thompson, Z. K., Charbonneau, D., Bean, J., Irwin, J., Burke, C. J., Désert, J.-M., Nutzman, P., & Falco, E. E. 2011, ApJ, 736, 12

Bessell, M. S. 1995, in The Bottom of the Main Sequence - and Beyond, ed. C. G. Tinney, 123

Bétrémieux, Y., & Kaltenegger, L. 2013, ApJL, 772, L31

Borucki, W. J., et al. 2011, ApJ, 736, 19

—. 2013, Science, 340, 587

Broecker, W. S. 1982, Geochim. Cosmochim. Acta, 46, 1689

Broeg, C., et al. 2013, in European Physical Journal Web of Conferences, Vol. 47, European Physical Journal Web of Conferences, 3005

Browning, M. K., Basri, G., Marcy, G. W., West, A. A., & Zhang, J. 2010, AJ, 139, 504

Cash, W. 2006, Nature, 442, 51

Cayrel de Strobel, G., Soubiran, C., Friel, E., Ralite, N., & Francois, P. 1997, Astronomy and Astrophysics Supplement Series, 124, 299

Cayrel de Strobel, G., Soubiran, C., & Ralite, N. 2001, A&A, 373, 159

Chapman, S. 1930, Memoirs of the Royal Meterological Society, 3, 103

Charbonneau, D., et al. 2009, Nature, 462, 891

Claire, M. W., Sheets, J., Cohen, M., Ribas, I., Meadows, V. S., & Catling, D. C. 2012, ApJ, 757, 95

Cleaves, H. J., & Miller, S. L. 1998, Proceedings of the National Academy of Sciences, 95, 7260

Cnossen, I., Sanz-Forcada, J., Favata, F., Witasse, O., Zegers, T., & Arnold, N. F. 2007, Journal of Geophysical Research (Planets), 112, 2008

Cockell, C. S. 1998, Journal of theoretical biology, 193, 717

Cockell, C. S. 1999, Icarus, 141, 399

—. 2000, Planet. Space Sci., 48, 203

Correia, A. C. M., et al. 2010, A&A, 511, A21

Crossfield, I. J. M., Barman, T., Hansen, B. M. S., & Howard, A. W. 2013, A&A, 559, A33

Crow, C. A., et al. 2011, ApJ, 729, 130

Crutzen, P. J. 1971, Journal of Geophysical Research, 76, 7311

de Wit, J., & Seager, S. 2013, Science, 342, 1473

Delfosse, X., Forveille, T., Perrier, C., & Mayor, M. 1998, A&A, 331, 581

Deming, D., et al. 2009, PASP, 121, 952

Des Marais, D. J., et al. 2002, Astrobiology, 2, 153

Di Folco, E., Thévenin, F., Kervella, P., Domiciano de Souza, A., Coudé du Foresto, V., Ségransan, D., & Morel, P. 2004, Astronomy and Astrophysics, 426, 601

Domagal-Goldman, S. D., Meadows, V. S., Claire, M. W., & Kasting, J. F. 2011, Astrobiology, 11, 419

Domagal-Goldman, S. D., Segura, A., Claire, M. W., Robinson, T. D., & Meadows, V. S. 2014, ApJ, 792, 90

Dressing, C. D., & Charbonneau, D. 2013, ApJ, 767, 95

—. 2015, submitted ApJ

Dumusque, X., et al. 2012, Nature, 491, 207

—. 2014, ApJ, 789, 154

Ehrenreich, D., et al. 2014, A&A, 570, A89

Flower, P. J. 1996, ApJ, 469, 355

Foreman-Mackey, D., Hogg, D. W., & Morton, T. D. 2014, The Astrophysical Journal, 795, 64

Forget, F., & Pierrehumbert, R. T. 1997, Science, 278, 1273

Forster, P., et al. 2007, in Climate Change 2007: The Physical Science Basis. Contribution of Working Group I to the Fourth Assessment Report of the Intergovernmental Panel on Climate Change, ed. S. Solomon, D. Qin, M. Manning, Z. Chen, M. Marquis, K. B. Averyt, M. Tignor, & H. L. Miller (Cambridge University Press, Cambridge, United Kingdom and New York, NY, USA.)

Fraine, J., et al. 2014, Nature, 513, 526

France, K., et al. 2013, ApJ, 763, 149

Fressin, F., et al. 2013, ApJ, 766, 81

Garcia-Pichel, F., Mechling, M., & Castenholz, R. W. 1994, Applied and environmental microbiology, 60, 1500

Gardner, J. P., et al. 2006, Space Sci. Rev., 123, 485

Gascón, J., Oubiña, A., Pérez-Lezaun, A., & Urmeneta, J. 1995, Current microbiology, 30, 177

Geballe, T. R., et al. 2002, ApJ, 564, 466

Goldblatt, C., Zahnle, K. J., Crisp, D., & Robinson, T. D. 2013, AGU Fall Meeting Abstracts, B2

Grant, R. H., & Heisler, G. M. 1997, Journal of Applied Meteorology, 36, 1336

Gray, D. 1992, The Observation and Analysis of Stellar Photospheres (The Observation and Analysis of Stellar Photospheres, by David F. Gray, pp. 470. ISBN 0521408687. Cambridge, UK (Cambridge University Press), 431

Grenfell, J. L., Gebauer, S., v. Paris, P., Godolt, M., & Rauer, H. 2014, Planet. Space Sci., 98, 66

Grenfell, J. L., Stracke, B., von Paris, P., Patzer, B., Titz, R., Segura, A., & Rauer, H. 2007, Planetary and Space Science, 55, 661

Guzmán-Marmolejo, A., Segura, A., & Escobar-Briones, E. 2014, Astrobiology, 13, 550

Hansen, C. J., Schwartz, J. C., & Cowan, N. B. 2014, MNRAS, 444, 3632

Haqq-Misra, J. D., Domagal-Goldman, S. D., Kasting, P. J., & Kasting, J. F. 2008, Astrobiology, 8, 1127

Hawley, S. L., Gizis, J. E., & Reid, I. N. 1996, AJ, 112, 2799

Hegde, S., & Kaltenegger, L. 2013, Astrobiology, 13, 47

Howard, A. W., et al. 2012, ApJS, 201, 15

Hu, R., Seager, S., & Bains, W. 2012, ApJ, 761, 166

Jenkins, J. S., Ramsey, L. W., Jones, H. R. A., Pavlenko, Y., Gallardo, J., Barnes, J. R., & Pinfield, D. J. 2009, ApJ, 704, 975

Johnson, H. M., & Wright, C. D. 1983, ApJS, 53, 643

Johnson, J. A., & Apps, K. 2009, ApJ, 699, 933

Jones, D., & West, A. A. 2014, submitted ApJ

Kaltenegger, L. 2010, ApJL, 712, L125

Kaltenegger, L., Fridlund, M., & Karlsson, A. 2006, Ap&SS, 306, 147

Kaltenegger, L., Henning, W. G., & Sasselov, D. D. 2010, AJ, 140, 1370

Kaltenegger, L., & Sasselov, D. 2010, ApJ, 708, 1162

—. 2011, ApJL, 736, L25

Kaltenegger, L., Sasselov, D., & Rugheimer, S. 2013, ApJL, 775, L47

Kaltenegger, L., & Traub, W. A. 2009, ApJ, 698, 519

Kaltenegger, L., Traub, W. A., & Jucks, K. W. 2007, ApJ, 658, 598

Kasting, J. F. 1988, Icarus, 74, 472

—. 1992, LPI Contributions, 789, 54

Kasting, J. F., & Ackerman, T. P. 1986, Science, 234, 1383

Kasting, J. F., & Harman, C. E. 2013, Nature, 504, 221

Kasting, J. F., Holland, H. D., & Pinto, J. P. 1985, J. Geophys. Res., 90, 10497

Kasting, J. F., Pollack, J. B., & Crisp, D. 1984, J. Atmos. Chem., 1

Kasting, J. F., Whitmire, D. P., & Reynolds, R. T. 1993, Icarus, 101, 108

Kerwin, B. A., & Remmele, R. L. 2007, Journal of pharmaceutical sciences, 96, 1468

Kharecha, P., Kasting, J. F., & Siefert, J. 2005, Geobiology, 3

Kiang, N. Y., et al. 2007, Astrobiology, 7, 252

Kitzmann, D., Patzer, A. B. C., von Paris, P., Godolt, M., & Rauer, H. 2011a, A&A, 531, A62

—. 2011b, A&A, 534, A63

Klaasen, K. P., et al. 2008, Review of Scientific Instruments, 79, 091301

Knutson, H. A., Benneke, B., Deming, D., & Homeier, D. 2014a, Nature, 505, 66

Knutson, H. A., et al. 2014b, ApJ, 794, 155

Kopparapu, R. K., et al. 2013, ApJ, 765, 131

Kreidberg, L., et al. 2014a, ApJL, 793, L27

—. 2014b, Nature, 505, 69

Kurucz, R. L. 1979, The Astrophysical Journal Supplement Series, 40, 1

Lawson, P., Seager, S., Stapelfeldt, K., Brenner, M., Lisman, D., Siegler, N., Unwin, S., & Warfield, K. 2014, in SPIE Astronomical Telescopes+ Instrumentation, International Society for Optics and Photonics, 91432Q–91432Q

Lederberg, J. 1965, Nature, 207, 9

Levi, A., Sasselov, D., & Podolak, M. 2014, ApJ, 792, 125

Linsky, J. L., France, K., & Ayres, T. 2013, ApJ, 766, 69

Livengood, T. A., et al. 2011, Astrobiology, 11, 907

Lovelock, J. E. 1975, Royal Society of London Proceedings Series B, 189, 167

Luger, R., & Barnes, R. 2014, ArXiv e-prints

Maness, H. L., Marcy, G. W., Ford, E. B., Hauschildt, P. H., Shreve, A. T., Basri, G. B., Butler, R. P., & Vogt, S. S. 2007, PASP, 119, 90

Marcy, G. W., & Chen, G. H. 1992, ApJ, 390, 550

Marty, B., Zimmermann, L., Pujol, M., Burgess, R., & Philippot, P. 2013, Science, 342, 101

Massa, D., & Fitzpatrick, E. L. 1998, in Bulletin of the American Astronomical Society, Vol. 30, American Astronomical Society Meeting Abstracts, 1267

Massa, D., & Fitzpatrick, E. L. 2000, ApJS, 126, 517

Matsunaga, T., Hieda, K., & Nikaido, O. 1991, Photochemistry and photobiology, 54, 403

Mayor, M., & Queloz, D. 1995, Nature, 378, 355

Meadows, V. S. 2005, Proceedings of the International Astronomical Union, 1, 25

Miguel, Y., Kaltenegger, L., Linsky, J. L., & Rugheimer, S. 2015, MNRAS, 446, 345

Misra, A., Meadows, V., Claire, M., & Crisp, D. 2014, Astrobiology, 14, 67

Misra, A., Meadows, V., & Crisp, D. 2014, ApJ, 792, 61

Molina, M. J., & Rowland, F. S. 1974, Nature, 249, 810

Munakata, N., Saito, M., & Hieda, K. 1991, Photochemistry and photobiology, 54, 761

Neves, V., et al. 2012, A&A, 538, A25

Nienow, J. A., & Friedmann, E. I. 1993, Antarctic microbiology, 343

Nienow, J. A., McKay, C. P., & Friedmann, E. I. 1988, Microbial ecology, 16, 271

Pallé, E., Ford, E. B., Seager, S., Montañés-Rodríguez, P., & Vazquez, M. 2008, ApJ, 676, 1319

Parisi, A. V., & Downs, N. 2004, Photochemical & Photobiological Sciences, 3, 643

Patel, B. H., Percivalle, C., Ritson, D. J., Duffy, C. D., & Sutherland, J. D. 2015, Nature Chemistry, 7, 301

Pavlov, A. A., Brown, L. L., & Kasting, J. F. 2001, J. Geophys. Res., 106, 23267

Pavlov, A. A., Hurtgen, M. T., Kasting, J. F., & Arthur, M. A. 2003, Geology, 31, 87

Pavlov, A. A., & Kasting, J. F. 2002, Astrobiology, 2, 27

Pavlov, A. A., Kasting, J. F., Brown, L. L., Rages, K. A., & Freedman, R. 2000, J. Geophys. Res., 105, 11981

Petigura, E. A., Howard, A. W., & Marcy, G. W. 2013, Proceedings of the National Academy of Science, 110, 19273

Pierrehumbert, R., & Gaidos, E. 2011, ApJL, 734, L13

Quintana, E. V., et al. 2014, Science, 344, 277

Rauer, H., et al. 2011, Astronomy and astrophysics, 529

Reiners, A., & Basri, G. 2008, ApJ, 684, 1390

Ricker, G. R., et al. 2014, in Society of Photo-Optical Instrumentation Engineers (SPIE) Conference Series, Vol. 9143, Society of Photo-Optical Instrumentation Engineers (SPIE) Conference Series, 20

Ritson, D., & Sutherland, J. D. 2012, Nature chemistry, 4, 895

Robinson, T. D., et al. 2011, Astrobiology, 11, 393

Rodler, F., & López-Morales, M. 2014, ApJ, 781, 54

Rojas-Ayala, B., Covey, K. R., Muirhead, P. S., & Lloyd, J. P. 2010, ApJL, 720, L113

—. 2012, ApJ, 748, 93

Rugheimer, S., Kaltenegger, L., Segura, A., Linsky, J. L., & Mohanty, S. 2015a, submitted ApJ

Rugheimer, S., Kaltenegger, L., Zsom, A., Segura, A., & Sasselov, D. 2013, Astrobiology, 13, 251

Rugheimer, S., Segura, A., & Kaltenegger, L. 2015b, in press ApJ

Saffe, C., Gómez, M., & Chavero, C. 2005, A&A, 443, 609

Sagan, C., Thompson, W. R., Carlson, R., Gurnett, D., & Hord, C. 1993, Nature, 365, 715

Sato, S., Cuntz, M., Guerra Olvera, C. M., Jack, D., & Schröder, K.-P. 2014, International Journal of Astrobiology, 13, 244

Schaefer, L., & Sasselov, D. 2015, ArXiv e-prints

Schindler, T. L., & Kasting, J. F. 2000, Icarus, 145, 262

Schwieterman, E., Robinson, T. D., Meadows, V., Crisp, D., & Misra, A. 2014, in American Astronomical Society Meeting Abstracts, Vol. 223, American Astronomical Society Meeting Abstracts #223, #347.18

Seager, S. 2014, Proceedings of the National Academy of Sciences, 111, 12634

Seager, S., & Bains, W. 2015, Science Advances, 1, e1500047

Seager, S., Bains, W., & Hu, R. 2013, ApJ, 775, 104

Seager, S., Schrenk, M., & Bains, W. 2012, Astrobiology, 12, 61

Seager, S., Turner, E. L., Schafer, J., & Ford, E. B. 2005, Astrobiology, 5, 372

Segura, A., Kasting, J. F., Meadows, V., Cohen, M., Scalo, J., Crisp, D., Butler, R. A. H., & Tinetti, G. 2005, Astrobiology, 5, 706

Segura, A., Krelove, K., Kasting, J. F., Sommerlatt, D., Meadows, V., Crisp, D., Cohen, M., & Mlawer, E. 2003, Astrobiology, 3, 689

Segura, A., Meadows, V. S., Kasting, J. F., Crisp, D., & Cohen, M. 2007, A&A, 472, 665

Segura, A., Walkowicz, L. M., Meadows, V., Kasting, J., & Hawley, S. 2010, Astrobiology, 10, 751

Selsis, F. 2000, in ESA Special Publication, Vol. 451, Darwin and Astronomy : the Infrared Space Interferometer, ed. B. Schürmann, 133

Selsis, F., Kasting, J. F., Levrard, B., Paillet, J., Ribas, I., & Delfosse, X. 2007, A&A, 476, 1373

Senanayake, S. D., & Idriss, H. 2006, Proceedings of the National Academy of Science, 103, 1194

Setlow, R. B. 1974, Proceedings of the National Academy of Sciences, 71, 3363

Shields, A. L., Bitz, C. M., Meadows, V. S., Joshi, M. M., & Robinson, T. D. 2014, ApJL, 785, L9

Shields, A. L., Meadows, V. S., Bitz, C. M., Pierrehumbert, R. T., Joshi, M. M., & Robinson, T. D. 2013, Astrobiology, 13, 715

Shkolnik, E. L., & Barman, T. S. 2014, accepted to ApJ

Sneep, M., & Ubachs, W. 2005, Journal of Quantitative Spectroscopy and Radiative Transfer, 92, 293

Snellen, I. A. G., de Kok, R. J., le Poole, R., Brogi, M., & Birkby, J. 2013, ApJ, 764, 182

Solomon, S. C., & Head, J. W. 1991, Science, 252, 252

Som, S., Catling, D. C., Harnmeijer, J., Polivka, P., & Buick, R. 2012, AGU Fall Meeting Abstracts, G4

Stapelfeldt, K. R., et al. 2014, Proc. SPIE, 9143, 91432K

Swift, J. J., Johnson, J. A., Morton, T. D., Crepp, J. R., Montet, B. T., Fabrycky, D. C., & Muirhead, P. S. 2013, ApJ, 764, 105

Tevini, M. 1993, Effects on humans, animals, microorganisms and materials

Tian, F., France, K., Linsky, J. L., Mauas, P. J. D., & Vieytes, M. C. 2014, Earth and Planetary Science Letters, 385, 22

Toon, O. B., McKay, C. P., Ackerman, T. P., & Santhanam, K. 1989, J. Geophys. Res., 94, 16287

Torres, G., et al. 2015, ArXiv e-prints

Traub, W. A. 2003a, in ESA Special Publication, Vol. 539, Earths: DARWIN/TPF and the Search for Extrasolar Terrestrial Planets, ed. M. Fridlund, T. Henning, & H. Lacoste, 231–239

Traub, W. A. 2003b, in Astronomical Society of the Pacific Conference Series, Vol. 294, Scientific Frontiers in Research on Extrasolar Planets, ed. D. Deming & S. Seager, 595–602

Traub, W. A., & Stier, M. T. 1976, Appl. Opt., 15, 364

Traub, W. A., et al. 2006, in Society of Photo-Optical Instrumentation Engineers (SPIE) Conference Series, Vol. 6268, Society of Photo-Optical Instrumentation Engineers (SPIE) Conference Series, 62680T

Udry, S., et al. 2007, A&A, 469, L43

Valenti, J. A., & Fischer, D. A. 2005, ApJS, 159, 141

van Leeuwen, F. 2007, A&A, 474, 653

Voet, D., Gratzer, W., Cox, R., & Doty, P. 1963, Biopolymers, 1, 193

von Braun, K., et al. 2011, ApJL, 729, L26

—. 2012, ApJ, 753, 171

—. 2014, MNRAS, 438, 2413

Walkowicz, L. M., & Hawley, S. L. 2009, AJ, 137, 3297

Wang, J., & Fischer, D. A. 2015, AJ, 149, 14

Wehner, J., & Horneck, G. 1995, Journal of Photochemistry and Photobiology B: Biology, 28, 77

West, A. A., & Basri, G. 2009, ApJ, 693, 1283

West, A. A., et al. 2004, AJ, 128, 426

—. 2011, AJ, 141, 97

Wood, B. E., Redfield, S., Linsky, J. L., Müller, H.-R., & Zank, G. P. 2005, The Astrophysical Journal Supplement Series, 159, 118

Wordsworth, R., & Pierrehumbert, R. 2013, in EGU General Assembly Conference Abstracts, Vol. 15, EGU General Assembly Conference Abstracts, 6470

Wordsworth, R., & Pierrehumbert, R. 2014, ApJL, 785, L20

Wordsworth, R. D., Forget, F., Selsis, F., Millour, E., Charnay, B., & Madeleine, J.-B. 2011, ApJL, 733, L48

Yamada, H., & Hieda, K. 1992, Photochemistry and photobiology, 55, 541

Zeng, L., & Sasselov, D. 2013, PASP, 125, 227

—. 2014, ApJ, 784, 96

Zsom, A., Seager, S., de Wit, J., & Stamenković, V. 2013, ApJ, 778, 109